The Dissertation Committee for Christopher Fernandez Lietz
certifies that this is the approved version of the following dissertation:

Large-Eddy Simulation of Gas Turbine Combustors using Flamelet Manifold Methods

Committee:

Noel T. Clemens, Supervisor

Venkatramanan Raman, Co-supervisor

Ofodike A. Ezekoye

David B. Goldstein

Philip L. Varghese

Large-Eddy Simulation of Gas Turbine Combustors using Flamelet Manifold Methods

by

Christopher Fernandez Lietz, B.S.E.M.

DISSERTATION

Presented to the Faculty of the Graduate School of

The University of Texas at Austin

in Partial Fulfillment

of the Requirements

for the Degree of

DOCTOR OF PHILOSOPHY

THE UNIVERSITY OF TEXAS AT AUSTIN

December 2015

Large-Eddy Simulation of Gas Turbine Combustors using Flamelet Manifold Methods

Publication No. _____

Christopher Fernandez Lietz, Ph.D.
The University of Texas at Austin, 2015

Supervisor: Noel T. Clemens
Co-Supervisor: Venkatramanan Raman

The main objective of this work was to develop a large-eddy simulation (LES) based computational tool for application to both premixed and non-premixed combustion of low-Mach number flows in gas turbines.

In the recent past, LES methodology has emerged as a viable tool for modeling turbulent combustion. LES is particularly well-suited for the computation of large scale mixing, which provides a firm starting point for the small scale models which describe the reaction processes. Even models developed in the context of Reynolds averaged Navier-Stokes (RANS) exhibit superior results in the LES framework. Although LES is a widespread topic of research, in industrial applications it is often seen as a less attractive option than RANS, which is computationally inexpensive and often returns sufficiently accurate results. However, there are many commonly encountered problems for which

RANS is unsuitable. This work is geared towards such instances, with a solver developed for use in unsteady reacting flows on unstructured grids. The work is divided into two sections.

First, a robust CFD solver for a generalized incompressible, reacting flow configuration is developed. The computational algorithm, which combines elements of the low-Mach number approximation and pressure projection methods with other techniques, is described. Coupled to the flow solver is a combustion model based on the flamelet progress variable approach (FPVA), adapted to current applications. Modifications which promote stability and accuracy in the context of unstructured meshes are also implemented.

Second, the LES methodology is used to study three specific problems. The first is a channel geometry with a lean premixed hydrogen mixture, in which the unsteady flashback phenomenon is induced. DNS run in tandem is used for establishing the validity of the LES. The second problem is a swirling gas turbine combustor, which extends the channel flashback study to a more practical application with stratified premixed methane and hydrogen/methane mixtures. Experimental results are used for comparison. Finally, the third problem tests the solver's abilities further, using a more complex fuel JP-8, Lagrangian fuel droplets, and a complicated geometry. In this last configuration, experimental results validate early simulations while later simulations examine the physics of reacting sprays under high centripetal loading.

Table of Contents

List of Tables

List of Figures

Chapter 1

Introduction

This work is motivated by the desire to develop a computational fluid dynamics (CFD) tool for a broad family of applications. The solver discussed here uses an incompressible algorithm and flamelet manifold-based combustion modeling implemented into an open-source code for the solution of fluid mechanics problems on unstructured grids. While it can be used for a variety of problems, the cases examined here are gas turbine combustors. This chapter will provide a brief informational framework of turbine technology and its continued evolution. From this expansive topic, the specific challenges associated with combustion modeling will be described. Finally, the scope of the work and methodology will be defined within this context.

1.1 Gas turbine combustors

1.1.1 Background

Gas turbine combustors have been a widely used technology since their inception. Their versatility and in particular their scalability allows application to several engineering problems, from power generation to trains, ships, and planes [81]. Despite modern advances and additional complexities, the ba-

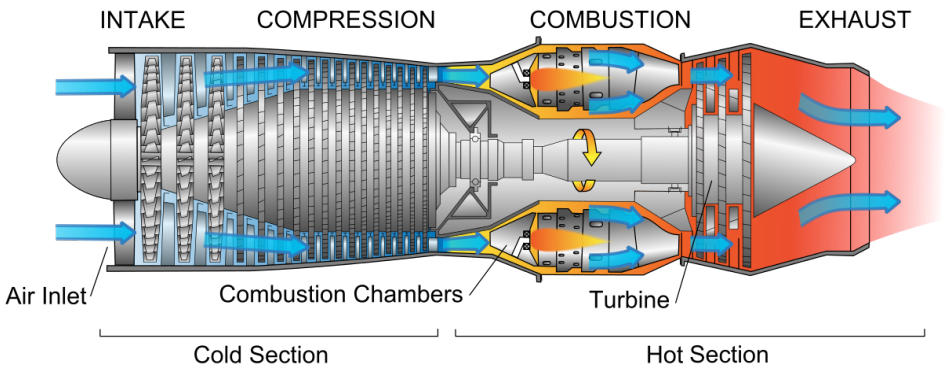

Figure 1.1: Schematic of a thrust-generating gas turbine combustor.

sic idea has remained the same. Air is drawn through the compressor, raising its pressure. The pressurized air enters the combustion chamber and is mixed with fuel. The mixture is then ignited yielding an expansion that forces the stream past the turbine, causing it to rotate. By directing some of the turbine output back into the compressor, the process cycles continuously. The remainder of the output can be used for thrust or power generation. A schematic of a typical gas turbine is shown in Figure 1.1 [3]. This sketch illustrates only the major components typically seen: air intake, compressor, combustion chamber, turbine, and exhaust. While all of these are areas of ongoing research, the combustion chamber is the only portion considered in this work.

Unlike the compressor and turbine, whose mechanical components rotate about the centerline axis, the combustor remains stationary. Because of this, it can be less axisymmetric and more modular. Several different designs exist: annular, tubular, and can-annular. Figure 1.2 shows a detailed view of a real world gas turbine developed by General Electric [1]. From this detailed

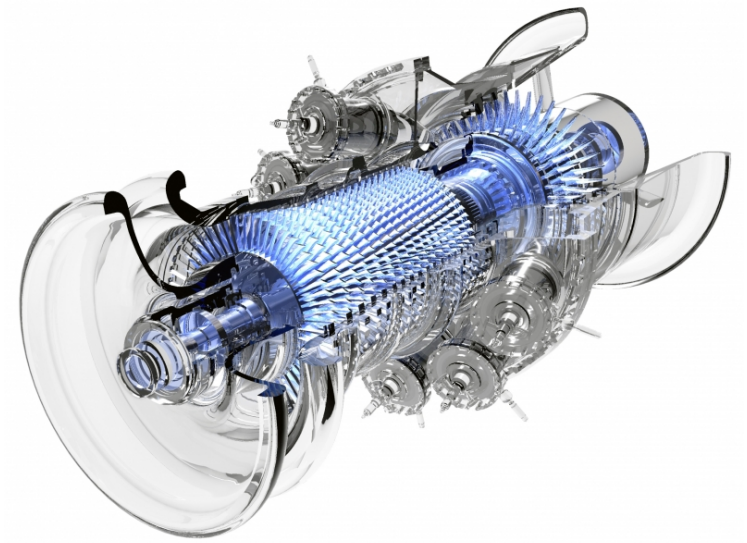

Figure 1.2: Detailed view of GE 7E.03 gas turbine, illustrating can-type combustion chambers.

isometric view, it is clear that the combustion chamber is not a single chamber, but rather a collection of cylindrical cans placed around the circumference of the section. These isolated chambers are more easily manufactured, optimized, controlled, and replaced than a single large annular chamber. Each contains its own fuel injector, igniter, liner, and casing.

Consequently, the problem is reduced to studying individual cans. These cans take two streams corresponding to air received from the compressor and fuel from a reservoir. The streams are combined and mix within the chamber before being ignited. Even in this comparatively simpler scenario, however, many choices are available with varying effects. The manner of fuel injection can be liquid or gas and the injector placement strongly affects how well mixing occurs. These factors also play an important part in how completely

the fuel is burned, which determines the overall efficiency of the engine and harmful emissions. Additionally, the mode of ignition effects the stability of the flame, with transient phenomena like blow-off or flashback amongst the potential problems [48]. All of these are basic design considerations regarding the fluid and combustion-based physics, to say nothing of the related material issues associated with them.

1.1.2 Modern combustor advances and related issues

While the basic principles of gas turbines were developed decades ago, the combustors continue to see additional iterations for the purpose of advancing modern agendas and reaching modern goals [39]. Some of these are sudden, the result of unforeseen external circumstances, such as federal regulations which may require a reduction of certain emissions. Other times, entirely new schools of application may appear with a different set of priorities. These types of stimuli reorient the focus and rules of the design process. However, many times advances are more deliberate and gradual.

One of the major factors for these incremental changes is the advancement of material science [39, 57]. Materials with better strength-to-weight ratios, higher melting points, increased resistance to corrosion and oxidation, less brittleness, and decreased tendency to creep damage, amongst other factors, significantly affect the way configurations must be arranged and parts must be designed. Most recently, the development of nickel-, cobalt-, and titanium-based alloys, in addition to new coatings and liners, have substan-

tially changed acceptable force and heat loadings. Often in gas turbines, particularly in aerospace applications, size and weight are equivalent to cost. New materials yield smaller flow cavities and combustion chambers and consequently new fluids problems for simulation.

Finally, cost reduction and increased overall efficiency lead to an unending cycle of experimentation. This includes many aspects such as fuel mixture and phase, delivery system, mixing methods, ignition modes, and more. One area of particular note is an increased usage of hydrogen-based fuels in gas turbine combustors, with environmentally friendly byproducts being an obvious benefit. Such changes are never without consequences, however, and these will be discussed in the chapters regarding flashback. Any or all of these are reasons why gas turbine combustors continue to evolve.

1.2 Current state of modeling

In the recent past, LES methodology has emerged as a viable tool for modeling turbulent combustion [60]. LES is particularly well-suited for the computation of large scale mixing, which provides a firm starting point for the small scale models which describe the reaction processes. Even models developed in the context of Reynolds averaged Navier-Stokes (RANS) exhibit superior results in the LES framework. For this reason, the LES approach is used in this work. Unlike RANS, where the flow is decomposed into a mean and fluctuation, LES decomposes fields according to some length scale, Δ, the filter width. Using a low-pass filter, all length scales below Δ are removed

[74]. The unresolved scalars are modeled while all resolved scale motions are represented directly on the computational grid.

There are many different combustion models available in CFD with varying modes of implementation and strengths corresponding to the particular problems they were developed for. Models can be divided according to the physics governing those problems. Some factors of note include fundamental flow aspects, such as Mach number and Reynolds number, which dictate the form of the transport equations and turbulent length and time scales [51]. The fuel itself plays an important role in chemical length and time scales, and thus the Damkohler number is relevant as well. The combustion regime heavily affects which models are appropriate, with the mixedness of the fuel described either as non-premixed, premixed, or partially premixed [67, 72]. Turbulence-flame interactions also comes into play. Predictive numerical simulations of gas turbine combustors require models which can bridge the gap between different regimes.

Often, the models themselves are not mutually exclusive and fusions of two or more distinct models can provide improved results, sampling advantages from both. The list presented here is therefore not exhaustive, but gives the reader a basic idea of several unique approaches which are of relevance to this work.

- **Detailed chemistry:** All reacting scalars are transported and the chemical mechanism is solved at every time step. While this has the ad-

vantage of easily accounting for things like differential diffusion and local variations in mass fraction, it can quickly become intractable. Complex fuels can contain hundreds of species, which will require their own equations. Furthermore, the reaction source term is determined through an extremely stiff ordinary differential equation (ODE), which will rapidly increase computational expense. Some variations use reduced chemistry, which removes certain species and elementary reactions based upon their time scales, leaving only the most important [47, 83, 63]. In the limit, this reduction becomes a one-step mechanism.

- **Flamelet models:** A natural extension of reduced chemistry models, flamelet-based methods take a similar approach, using a reduced thermochemical space to define the physics governing the combustion problem, such as fuel concentration, flame location, and enthalpy losses [13, 71]. In this way, the number of transported scalars can be reduced substantially. If the flame can be approximated as a locally laminar one-dimensional premixed flamelet, the answer could be as few as one. Rather than limiting these scalars to single species mass fractions, the method creates new scalars by combining them with the intention of obtaining more informative variables. Thus a variable defined in terms of both an intermediate and final product can better describe the flame structure than either could alone.

- **Manifold methods:** Manifold methods confront another aspect of the high computational expense associated with detailed chemistry: so-

lution of the mechanism ODE. Rather than solving this ODE at every step and cell during runtime, the solutions are tabulated beforehand and stored in a chemistry look-up table. Subsequently, the state need only be interpolated to the appropriate location in the thermochemical space and quantities such as density and reaction source term may be extracted [7, 89]. The full space spanned by the table occupies $N_S + 2$ dimensions, with N_S being the number of species. For unabridged mechanisms, the table can reach sizes on the order of tens or hundreds of gigabytes which is well outside the memory associated with a node on modern supercomputers. Therefore, tabulated chemistry is closely associated with a reduced order thermochemical space, such as the flamelet method described above.

- **Transported filtered probability density function (FPDF) models:** In many instances, a combustion model must assume some PDF shape to describe the statistics of sub-filter effects [55, 73, 77]. The transported FPDF method takes a more statistically sound approach by reconstructing the function, either through a Lagrangian or Eulerian formulation, allowing it to take a more organic shape according to the appropriate governing equations. In the former case, a Monte-Carlo type method is used, with 10-20 notional particles in each cell. Unfortunately, a computational expense penalty accompanies the technique. The Eulerian formulation alleviates this using quadrature, with the moments of the PDF described by a series of δ-peaks, each with a dedicated trans-

port equation. The closure in this case is simply relocated to a sub-filter mixing term.

1.3 Scope of the dissertation

While computational studies have focused on various transient instabilities in LES, there has not previously been accompanying DNS for detailed verification of model assumptions. The inavailability of results for verification has led to a disproportionate focus on more easily represented phenomena. Unsteady three-dimensional processes cannot be represented adequately by conventional RANS approaches. The objective of this work is to develop a robust computational tool for studying these behaviors in realistic gas turbine configurations. This tool will provide accurate results on unstructured meshes with easily adaptable schemes and the possibility for the user to alter the models with ease. This work will encompass two basic components: first, the development of said tool, and second, its application to three problems.

- **Development of an LES computational tool for low-Mach number reacting flows:** A robust solver has been developed using the open source CFD library OpenFOAM [2]. It focuses on low-Mach number flows with premixed or non-premixed chemistry or some combination thereof. Flamelet-based chemistry is used with additional consideration for phenomena such as wall heat loss and evaporation of fuel droplets. The solver is called utFlameletFoam.

- **Channel boundary layer flashback analysis using LES:** Using the LES tool, a model channel configuration is simulated. The channel was also simulated at Lawrence Livermore National Laboratory (LLNL) in the form of a DNS using detailed chemical kinetics [32]. Channel flashback is the primary behavior of interest, while the effects of subfilter models, numerical methods, and boundary conditions on flow predictions are discussed. The validity of the flamelet assumption in this context is examined in detail.

- **Flashback analysis in a swirl burner configuration using LES:** Using the LES tool, a model swirl burner configuration that was experimentally studied at UT is simulated [22, 23]. Both stable burning and flame flashback conditions, as well as the transition between these two states, are considered. Additionally, the effects of complex flow physics and non-orthogonal grids are discussed. Results are compared against detailed measurements from the UT experimental swirl burner.

- **Flame and droplet stability analysis in a swirl burner configuration using LES:** Using the LES tool, a unique swirl burner configuration that was experimentally studied at the Air Force Research Laboratory (AFRL) is simulated [90, 92]. The geometry contains an annular mixing cavity and angled air injection which, coupled with fuel droplet sprays, yields a high-g loading. The effects of these forces on combustion efficiency and flame stabilization will be discussed. Results are compared against detailed measurements obtained directly from AFRL.

Chapter 2

Development of a low-Mach number solver for reacting flows on unstructured meshes

Solver development strongly depends on the software chosen for implementation of the models and algorithms. Therefore, the organizational framework of the library in question, OpenFOAM, is described in detail for the purpose of giving the reader an idea of standard practices and usage. The essential elements of large eddy simulations are also derived, followed by the particulars of the specific models used in this work.

2.1 Open-source field operation and manipulation (OpenFOAM)

The open-source community has developed numerous CFD codes with varying purposes. These codes are typically tailored for specific problems, making them inflexible and rigid despite full accessibility to the source itself. Deviations from the presumed usage are at best complicated. For this reason, the C++ toolset OpenFOAM was chosen, which is extremely versatile by design [2]. Developed at Imperial College London in the late 1980s and early 1990s, OpenFOAM has been slow to gain traction, but in the past decade it has attained the full support of such companies as Airbus, Mitsubishi, and

Volkswagen [37]. The increased usage by companies is indicative of a broader trend towards versatility and decreasing license expense at the cost of user-end experience and customer support.

2.1.1 Code organization

The core of OpenFOAM is a set of libraries used to develop custom solvers and utilities for the solution of continuum mechanics problems, with a focus on computational fluid dynamics. From the beginning, granting users heavy customization has been a key factor in the code's organization. OpenFOAM is structured hierarchically and the source can be subdivided into three broad tiers. While superficial modifications are made reasonably simple, the difficulty increases steeply as alterations reach deeper libraries and classes. A schematic of this code organization can be seen in Figure 2.1.

The top tier is the case directory, containing all of the details of the problem being solved, which is divided into three subdirectories. Any subdirectory with a strictly numeric designation is seen by OpenFOAM as a time directory, meaning its contents are field data and boundary conditions. Each field is contained within a single file. In addition to volume and surface fields, Lagrangian particles are stored there as well. Which fields are necessary depends upon the solver. In this work, velocity, pressure, mixture fraction, reaction progress variable, total enthalpy, and turbulent viscosity are always solved, with the possibility for fuel droplets. The system subdirectory contains files read at each time step, allowing the user to adjust these input parameters

```
Case
   ➡ 0                    rho, U, p
   ➡ constant             polyMesh, turbulenceProperties
   ➡ system               controlDict, fvSchemes, fvSolution
Applications
   ➡ solvers              icoFoam, rhoPisoFoam, reactingFoam
   ➡ utilities            decomposeMesh, foamToVTK, sample
Source
   ➡ models               turbulenceModels, combustionModels
   ➡ numerics             finiteVolume, ODE
   ➡ mesh                 dynamicMesh, edgeMesh, mesh, surfMesh
   ➡ tools                postProcessing, sampling
   ➡ miscellaneous        engine, OSspecific, parallel
```

Figure 2.1: Schematic of case and code organization in OpenFOAM.

during runtime. Additional dictionaries are stored there, such as those used to define data sampling, but only three files are required by a solver: controlDict, fvSchemes, and fvSolution. The first defines settings such as end time, time step, write frequency, and data precision. fvSchemes is used to set the discretization scheme for each term in all equations being solved. fvSolution sets the type of iterative solver used for each discretized linear system, as well as things likes pre-conditioners, tolerances, relaxation factors, and algorithmic loop conditions. Finally, the constant subdirectory contains any files not expected to change during run time. This includes the mesh itself as well as the choice of models, e.g. combustion, turbulence, and Lagrangian particles.

The middle tier in Figure 2.1 contains the applications themselves, divided into either utilities or solvers. Utilities have many supporting functions, from decomposing a mesh for parallel solution to averaging a field through a cross-section to converting between output data formats. Solvers are the primary executables in OpenFOAM, which solve the governing equations under a variety of conditions, such as high-speed compressible flows, Lagrangian sprays, or multiphase problems. Within these categories, there are further subdivisions, built around different algorithms, such as PISO (pressure implicit splitting of operators) or SIMPLE (semi-implicit method for pressure linked equations). Modifications to utilities and solvers require little to no base knowledge of C++. New algorithms are often a matter of rearranging key components while the addition of transported scalars is simplified by overloaded functions, resulting in code that plainly reflects its intent. This high level syntax is entirely contained within OpenFOAM and successfully reproduces standard mathematical notation, as seen in Figure 2.2. Furthermore, all objects at this level are built such that no special steps must be taken for parallelization.

```
solve
(
    fvm::ddt(rho, Zmix)
  + fvm::div(phi, Zmix)
  - fvm::laplacian(turbulence->muEff(), Zmix)
);
```

Figure 2.2: Typical code for scalar transport equation

The bottom tier of Figure 2.1 contains base libraries, upon which all the solvers and utilities are built. Though they technically exist at the same level in the code, it's worthwhile to subdivide the tier still further, separating them according to dependencies. For instance, the source directory contains templates for general physical models such as thermodynamics, turbulence, chemistry, Lagrangian particles, heat transfer, and others. While many of these models build upon one another (thermodynamics and chemistry, for instance), they are linked such that alterations in one leaves the others intact and still functional, without the need to recompile most of the code. In addition to models, many numerical aspects can be added here, such as primitive field operators, linear system solvers, and discretization schemes. As with the models, only these dynamic libraries require recompilation in the event of changes. The breadth of available choices and ease with which new options may be created is one of OpenFOAM's primary strengths. For completeness, the remainder of the source code is filled with libraries unlikely to change for any reason. These libraries contain the building blocks of OpenFOAM, such as various types of matrices, meshes, and other data objects. Special variants exist to allow for dimensions, boundary conditions, vector and tensor fields, volume and surface fields, and many others options. Finally, additional functionality such as parallelization, OS specific tools, and file formatting fall into this category. Changes made here will likely yield consequences throughout the entire code.

2.2 Large eddy simulations

The crux of large eddy simulations is the removal of small-scale physics, such as chemical reactions or energy dissipating turbulence, through a filtering operation which leaves the large-scales intact. These large scales are resolved on the computational grid while the effects of those removed, known as sub-grid scales, are modeled. The reason behind the distinction is that, generally speaking, solution of the discretized Navier-Stokes for all scales is computationally intractable. The detailed approach, direct numerical approach (DNS), requires a grid spacing on the order of the smallest features of the problem. In premixed combustion, this can be tenths of a millimeter, making domains beyond a few cubic decimeters impossible even on modern supercomputers. Furthermore, the high order discretization schemes require orthogonal grids, which limits the use of DNS to canonical problems rather than practical applications.

2.2.1 Filtered governing equations

The flow scales are divided according to a characteristic length called the filter-width (Δ). In implicit LES, used in this work and most practical large eddy simulations, the value is simply the local grid size. Considering some field variable Q and the filtering kernel $\mathcal{G}$, the filtering operation is defined by the following relation

$$\overline{Q}(\mathbf{x},t) = \int_{-\infty}^{\infty} Q(\mathbf{y},t)\mathcal{G}(\mathbf{x}-\mathbf{y},t)d\mathbf{y}, \tag{2.1}$$

where the kernel shape determines the type of filtering operation, for example box or Gaussian. In variable density flows, the filtering is typically density-weighted, a variation known as Favre filtering and denoted by a tilde:

$$\begin{aligned}\widetilde{Q}(\mathbf{x},t) &= \frac{\overline{\rho Q}}{\overline{\rho}} \\ &= \frac{1}{\overline{\rho}}\int_{-\infty}^{\infty}\rho(\mathbf{y},t)Q(\mathbf{y},t)\mathcal{G}(\mathbf{x}-\mathbf{y},t)d\mathbf{y},\end{aligned} \tag{2.2}$$

where $\overline{\rho}$ is the filtered density. Equations 2.3 through 2.5 show the Navier-Stokes equations as well as a transport equation for reacting scalar, ϕ_i, all formulated generally for problems containing sprays,

$$\frac{\partial \rho}{\partial t} + \frac{\partial \rho u_j}{\partial x_j} = S_\rho, \tag{2.3}$$

$$\frac{\partial \rho u_i}{\partial t} + \frac{\partial \rho u_i u_j}{\partial x_j} = -\frac{\partial p}{\partial x_i} + \frac{\partial \tau_{ij}}{\partial x_j} + F_i, \tag{2.4}$$

$$\frac{\partial \rho \phi_i}{\partial t} + \frac{\partial \rho \phi_i u_j}{\partial x_j} = \frac{\partial}{\partial x_j}\rho D_i \frac{\partial \phi_i}{\partial x_j} + S_{\phi_i}. \tag{2.5}$$

The Favre filtering operator can be applied to obtain the equations governing their respective filtered fields.

$$\frac{\partial \overline{\rho}}{\partial t} + \frac{\partial \overline{\rho}\widetilde{u}_j}{\partial x_j} = \widetilde{S}_\rho \tag{2.6}$$

$$\frac{\partial \overline{\rho}\widetilde{u}_i}{\partial t} + \frac{\partial \overline{\rho}\widetilde{u}_i\widetilde{u}_j}{\partial x_j} = -\frac{\partial \widetilde{p}}{\partial x_i} + \frac{\partial \tau_{ij}}{\partial x_j} + \frac{\partial}{\partial x_j}\overline{\rho}(\widetilde{u}_i\widetilde{u}_j - \widetilde{u_iu_j}) + \widetilde{F}_i \tag{2.7}$$

$$\frac{\partial \overline{\rho}\widetilde{\phi}_i}{\partial t} + \frac{\partial \overline{\rho}\widetilde{\phi}_i\widetilde{u}_j}{\partial x_j} = \frac{\partial}{\partial x_j}\overline{\rho}\widetilde{D}_i\frac{\partial \widetilde{\phi}_i}{\partial x_j} + \frac{\partial}{\partial x_j}\overline{\rho}(\widetilde{\phi}_i\widetilde{u}_j - \widetilde{\phi_iu_j}) + \widetilde{S}_{\phi_i}, \tag{2.8}$$

where $\widetilde{u}_i$ is the velocity, $\widetilde{p}$ is the pressure, and τ_{ij} is the viscous stress tensor. There are numerous unclosed terms in the Equations 2.6 through 2.8. The sub-grid contributions, colored in blue, are discussed in Section 2.2.2. The reaction source term, colored in green, is discussed in Section 2.2.3. The evaporation source terms, colored in red, are discussed in Section 2.2.4.

2.2.2 Sub-grid modeling

In filtering, the momentum and scalar equations each gain an unclosed sub-grid term. These terms represent a transfer from the large scales to the small scales and consequently must be dissipative in nature. With some exceptions, the term is approximated using an explicit sub-filter scale model. In the case of momentum, this algebraic eddy viscosity takes the following form

$$\overline{\rho}\widetilde{u}_i\widetilde{u}_j - \overline{\rho}\widetilde{u_iu_j} \approx 2\mu_t\widetilde{S}_{ij}, \tag{2.9}$$

where $\widetilde{S}_{ij}$ is the strain rate tensor. This term can subsequently be combined with the molecular viscosity at very minimal computational cost and formulated in terms of the gradients of resolved fields [8, 56]. In this work, the Smagorinsky closure model is used [79],

$$\mu_t = C_\mu \overline{\rho} \Delta^2 |\widetilde{S}|, \tag{2.10}$$

where $|\widetilde{S}| = \sqrt{\widetilde{S}_{ij}\widetilde{S}_{ij}}$. The coefficient C_μ can be fixed, but the dynamic approach has the advantage of eliminating the uncertainties associated with tuning, relying instead on information gained from the resolved turbulence [4, 31, 68, 69]. Regarding the scalar transport equation, analogous to the momentum equation, the sub-grid term can be closed using a gradient diffusion approximation and a turbulent diffusivity with dynamically calculated coefficient [27, 61]. Due to the widespread use of the dynamic procedure to close models, it will be discussed next.

2.2.2.1 Dynamic coefficients

The idea of dynamic coefficients came in the attempt to close sub-grid models [31, 49]. As described above, these models contain a scaling coefficient. Previously, the value of this coefficient was extracted from DNS of some canonical problems, such as free shear flows. The applicability of this value to more complex cases was often doubtful and proven incorrect in many cases. The procedure described here, developed by Germano et al., remedies this deficiency by applying scaling arguments to the filtering operation.

Consider an arbitrary nonlinear term, $f(Q)$, which is a known function of the field variables. Suppose the filtered value of this function is modeled by Equation 2.11, a sum of the resolved part $f(\overline{Q})$ and a sub-grid residual which takes the form of an algebraic model $m(Q)$. In general, $m(Q)$ can itself depend

on field variables as well as space and time and the grid filter width Δ.

$$\overline{f(Q)} = f(\overline{Q}) + m(\overline{Q}) \tag{2.11}$$

Dynamic modeling considers how Equation 2.11 will change subject to a different filter width. The overhat is used to refer to fields or operations evaluated with respect to this larger filter width, referred to as the test filter $\widehat{\Delta}$. An analogous expression to Equation 2.11 takes a similar form,

$$\widehat{\overline{f(Q)}} = f(\widehat{\overline{Q}}) + m(\widehat{\overline{Q}}). \tag{2.12}$$

Test filtering Equation 2.11 and subtracting it from Equation 2.12 yields the following identity,

$$\widehat{f(\overline{Q})} - f(\widehat{\overline{Q}}) = m(\widehat{\overline{Q}}) - \widehat{m(\overline{Q})}. \tag{2.13}$$

Interestingly, all terms in Equation 2.13 are computable from the resolved field. A consistent sub-grid model will contribute the same amount within the overlapping band between grid and test filter levels. This identity can therefore be used as a calibration constraint. In practice, the identity holds strictly only when $m(Q)$ is the exact sub-grid residual, not being modeled. Instantaneous application typically leads to unphysical fluctuations in model behavior, requiring some averaging to get stable coefficients. Furthermore, the identity may also lead to poor results in the event that the modeled

quantity varies minimally between grid and test filter scales. Such quantities include dissipation and chemical reaction rates, which are almost exclusively modeled and therefore require some alternative approach.

Revisiting the form of the dynamic Smagorinsky model from the prior section (and indeed many other sub-grid models),

$$m(\overline{Q}) = Cs(\overline{Q}, \Delta). \tag{2.14}$$

Here, $s(\overline{Q}, \Delta)$ is some algebraic scaling law with the appropriate dimensions for the term. C is an unknown dimensionless coefficient, which is allowed to vary in space and time in the procedure. By the dynamic identity,

$$\widehat{f(\overline{Q})} - f(\widehat{\overline{Q}}) = \widehat{C}s(\widehat{\overline{Q}}, \widehat{\overline{\Delta}}) - C\widehat{s(\overline{Q}, \Delta)}, \tag{2.15}$$

where $\widehat{C}$ is the model coefficient at the test filter level. Note that C has been left inside the test filtering operator in the right most term. While various formulations of the procedure offer different means of evaluating it, this study assumes the coefficient to be scale invariant and independent of the directions in which flow is statistically homogeneous. From this, C passes unchanged through the test filtering operator,

$$\widehat{f(\overline{Q})} - f(\widehat{\overline{Q}}) = C\left(s(\widehat{\overline{Q}}, \widehat{\overline{\Delta}}) - \widehat{s(\overline{Q}, \Delta)}\right). \tag{2.16}$$

The following declarations are typically made for simplicity

$$\mathcal{L} = \widehat{f(\overline{Q})} - f(\widehat{\overline{Q}}) \tag{2.17}$$

and

$$\mathcal{M} = s(\widehat{\overline{Q}}, \widehat{\overline{\Delta}}) - \widehat{s(\overline{Q}, \Delta)}. \tag{2.18}$$

To obtain a single value for C in each homogeneous region of the flow, this expression is solved using least-squares [49]. This yields the expression below, where angled brackets indicate averaging over directions of flow homogeneity

$$C = \frac{< \mathcal{L} \cdot \mathcal{M} >}{< \mathcal{M} \cdot \mathcal{M} >}. \tag{2.19}$$

2.2.3 Combustion modeling

The closure problem seen in turbulence modeling takes a different form in combustion modeling, where a discrepancy exists between any filtered reaction source term and the source term evaluated at the filtered location in thermochemical space, succinctly summarized as

$$\widetilde{S}(\phi) \neq S(\widetilde{\phi}). \tag{2.20}$$

Because of the strong non-linear behavior of the ODE, this discrepancy is too large to neglect and rectifying the two terms is key to an accurate combustion model. Furthermore, in both premixed and non-premixed combustion,

the reaction zone is usually small compared to the filter width and the term is mostly or wholly modeled, with little resolved. Because of this, any type of model requiring dynamically computed coefficients like those used for sub-grid turbulence is inapplicable.

2.2.3.1 The flamelet assumption

Recall again the transport equation for a generalized reacting scalar

$$\frac{\partial \rho \phi_i}{\partial t} + \frac{\partial \rho \phi_i u_j}{\partial x_j} = \frac{\partial}{\partial x_j} \rho D_i \frac{\partial \phi_i}{\partial x_j} + S_{\phi_i}, \tag{2.21}$$

where ϕ_i corresponds to the some component of the thermochemical composition vector, D_i represents molecular diffusivity, and S_{ϕ_i} is the chemical source term. Given the non-linearity of the source term and the complexity of typical chemical reactions, which yields a stiff system of equations, the expense of this calculation can rise rapidly. However, if the flame fulfills certain parameters, a strong approximation can be applied in order to reduce the computational cost. If the flame structure is smaller than the smallest turbulent length scales, eddies cannot penetrate it and the flame is considered a laminar, one-dimensional "flamelet" embedded in the turbulent velocity field [29]. The validity of the assumption depends on the relative length and time scales of the turbulence and the combustion. Because of this, a commonly used diagram was created for determining flame regime (Figure 2.3) [12, 67].

If the flame exists either as a corrugated or wrinkled flamelet, the thermochemical space can be vastly reduced, a class of combustion modeling known

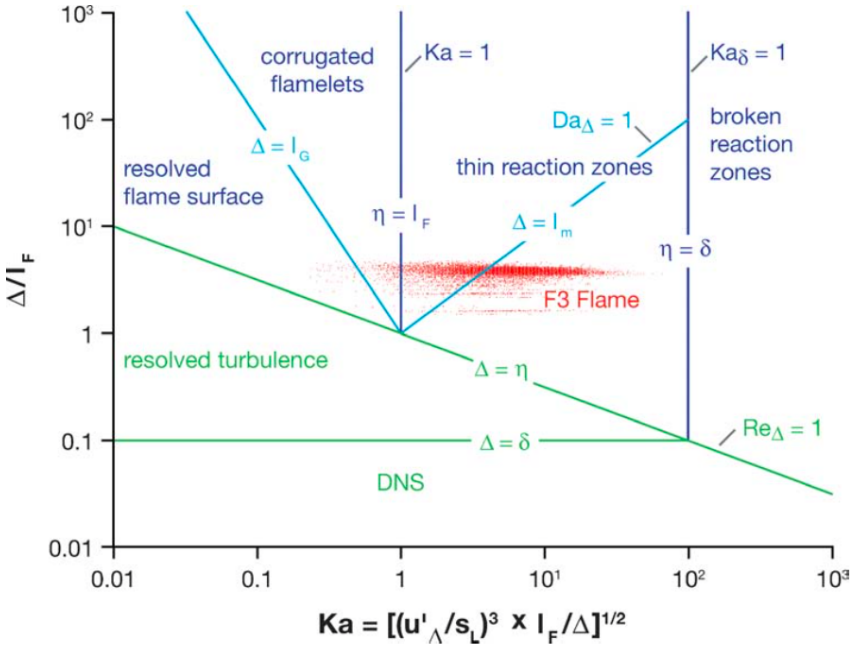

Figure 2.3: Regime diagram, divided according to Karlovitz number and non-dimensionalized flame thickness [72].

as flamelet models [7, 13, 71, 89, 34, 36, 10]. This redefinition of the compositional state in terms of fewer variables is one of the strengths of these models. The overall goal of a simulation and the driving physics which must be modeled determine how many and which variables are required. In this work, both premixed and non-premixed flames are simulated. Because of this, a tracking variable, the mixture fraction, is used to describe the relative proportion of fuel to oxidizer, i.e. the local equivalence ratio. As the flame is assumed to occur only in very thin regions, with variations throughout the flame significant only in the normal direction, a single variable is used to capture the degree to

which the mixture has burned. This measure, the reaction progress variable, also captures the location of the flame [68]. Finally, heat loss to walls is a common concern in industrial applications and in particular the phenomena being studied here, so total enthalpy will be tracked [89]. This is summarized as follows

$$\phi_i = \mathcal{F}(Z, C, h_t), \tag{2.22}$$

where each input variable is solved using a transport equation

$$\frac{\partial \rho Z}{\partial t} + \frac{\partial \rho Z u_i}{\partial x_i} = \frac{\partial}{\partial x_i} D \frac{\partial Z}{\partial x_i}, \tag{2.23}$$

$$\frac{\partial \rho C}{\partial t} + \frac{\partial \rho C u_i}{\partial x_i} = \frac{\partial}{\partial x_i} D \frac{\partial C}{\partial x_i} + \rho S_C, \tag{2.24}$$

and

$$\frac{\partial \rho h_t}{\partial t} + \frac{\partial \rho h_t u_i}{\partial x_i} = \frac{\partial}{\partial x_i} k \frac{\partial T}{\partial x_i}. \tag{2.25}$$

Total enthalpy is strictly defined for a given mixture, while the mixture fraction variable is simply a conserved scalar. In contrast, the reaction progress variable is defined at the discretion of the user. Consequently, it is easy to inadvertently create a variable which fails to capture the flame behavior. Traditionally, C is a normalized sum of some species mass fractions.

However, choosing an appropriate combination can have significant effects on the flame and requires careful consideration.

The reaction progress variable was initially designed to take the place of scalar dissipation as a look-up quantity. The reasoning behind this is obvious from Figure 2.4: the scalar dissipation rate χ cannot uniquely map all branches of the flame, with the unstable burning and non-burning branches ignored. Therefore, one of the two major guidelines is that for given values of Z and h_t, C should return a single composition. As its name suggests, the reaction progress variable must also serve as an indication of how far the reaction has progressed. Therefore, the second guideline indicates that a monotonically varying quantity works the best. This could be one of the fuels or final products, but as the behavior throughout the flame is of importance, it is likely that some combination of major species and minor species will provide a more even mapping from unburned to burned. Ideally, the flame would transition smoothly over the reaction progress variable, but as mentioned before, the LES grid seldom resolves any part of the flame resulting in a shock-like front. Some closures artificially broaden the flame to avoid such discontinuities [18].

Because of the need to use both transient and global species mass fractions in the progress variable, monotonicity and uniqueness cannot be guaranteed. Indeed, only the use of entropy would provide a truly universal combustion metric. Since no clear-cut rule otherwise exists for application to all fuels, in the end, some degree of experimentation is necessary to obtain an acceptable definition. For the three fuels used in this work, we choose as follows.

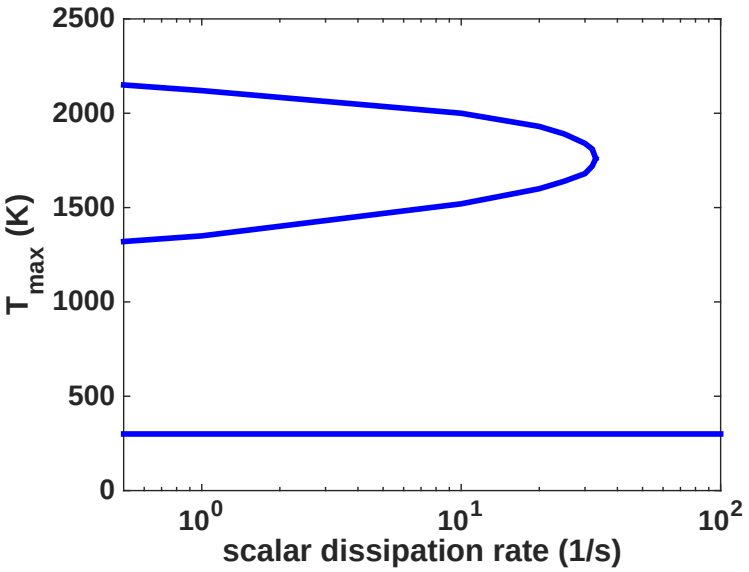

Figure 2.4: Maximum flamelet temperature for various scalar dissipation rates indicating stable burning (top), unstable burning (middle), and non-burning (bottom) branches for fixed values of mixture fraction and total enthalpy.

For H_2/CH_4,

$$C = 1 - \frac{Y_{H_2}}{Y_{H_2,max}} \tag{2.26}$$

pure CH_4,

$$C = 1 - \frac{Y_{CH_4}}{Y_{CH_4,max}} \tag{2.27}$$

and JP-8 surrogate

$$C = \frac{Y_{H_2} + Y_{CO_2} + Y_{H_2O}}{(Y_{H_2} + Y_{CO_2} + Y_{H_2O})_{max}} \tag{2.28}$$

2.2.3.2 Reduced manifolds

Despite the remapping of the thermochemical composition to a lower dimensional space, solution of the simplified ODE during runtime can still be expensive. For this reason, manifold based methods are often used in tandem with flamelets. Effectively, all possible combinations of the chemistry governing variables are calculated *a priori* and stored in an easily accessible table for subsequent look-up [89, 7]. In practice, this is done as follows. The reacting species transport equations are reformulated using the steady flamelet assumption, yielding

$$\rho \frac{\chi}{2} \frac{\partial^2 Y_i}{\partial Z^2} = -\rho S_i. \tag{2.29}$$

These steady flamelet equations are solved in one spatial coordinate, with the scalar dissipation rate serving as an adjustable parameter to fill the space. The thermochemical vector for the input space (Equation 2.22) is tabulated. From there, additional steps are taken to obtain the filtered outputs. Reiterating the filtering operation as a convolution with the PDF over the sample space,

$$\widetilde{\phi}_i = \int_{-\infty}^{\infty} \mathcal{F}(Z, C, h_t)\mathcal{P}(Z, C, h_t) dZ dC dh_t. \tag{2.30}$$

Here, $\mathcal{P}(Z, C, h_t)$ is the joint subfilter probability density function (PDF) of mixture fraction, reaction progress variable, and total enthalpy. In this case, Z, C, and h_t are assumed independent of one another. Prior studies have shown that $\mathcal{P}(Z)$ can be assumed to be a β-function while $\mathcal{P}(C)$ and $\mathcal{P}(h_t)$ are assumed to be δ-functions. As the β-function can be defined by two moments and the δ-function by one, the convolution simplifies.

$$\begin{aligned} \widetilde{\phi} &= \int_{-\infty}^{\infty} \mathcal{F}(Z, C, h_t)\beta(Z)\delta(C)\delta(h_t) dZ dC dh_t \\ &= \mathcal{F}'(\widetilde{Z}, \widetilde{Z}_{\mathcal{V}}, \widetilde{C}, \widetilde{h}_t) \end{aligned} \tag{2.31}$$

Equation 2.31 effectively replaces the stiff ODEs with a table of flamelets which may be easily accessed and from which quantities such as density, viscosity, and temperature are retrieved and quadrilinearly interpolated. $Z_{\mathcal{V}}$ is determined using an algebraic relation closed with the dynamic approach dis-

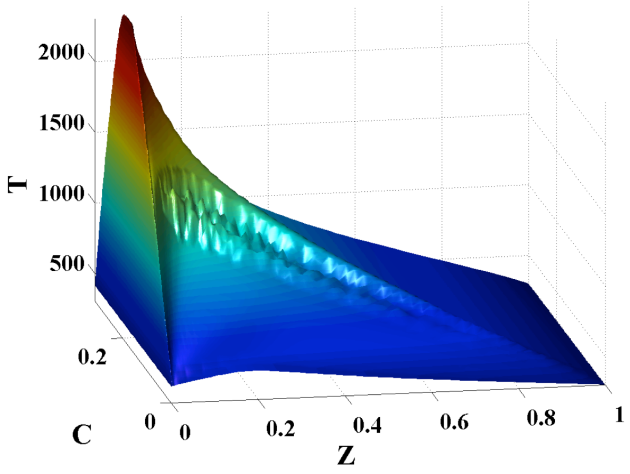

Figure 2.5: Example of temperature field mapped to Z and C for fixed Z_ν and h_t.

cussed previously. An example showing a temperature isosurface can be seen in Figure 2.5.

2.2.4 Lagrangian spray modeling

In the UCC, particles are injected into the computational domain via three axisymmetrically located hollow cone nozzles with an initial speed determined by a pressure differential

$$u = \sqrt{2\frac{p_{inj} - p_0}{\rho_d}}, \tag{2.32}$$

where p_{inj} is user-specified, p_0 is the background pressure, and ρ_d is the droplet density. The particle sizes and initial directions are determined randomly. The former is sampled from a Rosin-Rammler PDF with maximum, minimum, and

mean values, while the latter is sampled from a uniform distribution given some inner and outer cone angle. The particles are pure fuel, which fully determines their material properties and mass, and allows the direct translation of the evaporation source term into the mixture fraction equation.

Each particle, k, carries a state vector consisting of position ($\mathbf{X}_k^p$), velocity ($\mathbf{U}_k^p$), temperature (T_k^p), and mass (m_k^p). The evolution of each particle's position and velocity is governed by the following ballistic equations of motion [78],

$$\frac{d\mathbf{X}_k^p}{dt} = \mathbf{U}_k^p \tag{2.33}$$

and

$$\frac{d\mathbf{U}_k^p}{dt} = \frac{\mathbf{F}}{m_k^p}, \tag{2.34}$$

where $\mathbf{F}$ is the body force acting on the particles, which is recalculated at fractional time-steps. In this case, the only force is fluid drag, with the drag coefficient C_d follows the algebraic relation shown below [21].

$$C_D Re = \begin{cases} 0.424Re & : Re < 1000 \\ 24\left(1 + \frac{1}{6}Re^{2/3}\right) & : Re \geq 1000 \end{cases}$$

In equation 2.35, ρ_s is the interface density between the droplet and the gas, while $\mathbf{U}_g$ is the gas phase velocity linearly interpolated to the droplet position, and A is the wetted surface area of the droplet

$$\mathbf{F} = \frac{1}{2} C_d \rho_s (\mathbf{U}_g - \mathbf{U}_k^p)^2 A. \tag{2.35}$$

The droplet temperature, T_k^p, is governed by the following model [58, 59, 64], where the first term represents conduction from the surrounding gas and the second represents heat loss due to evaporation.

$$\frac{dT_k^p}{dt} = \frac{Nu}{3Pr} \frac{C_P}{C_L} \frac{f}{\tau_d} (T_g - T_k^p) - \frac{\dot{m}_k^p}{m_k^p} \frac{L_v}{C_L} \tag{2.36}$$

where C_P and C_L are the specific heats of the gas and liquid respectively and L_v is the latent heat of vaporization of the liquid droplet. τ_d is a characteristic particle time given by

$$\tau_d = \frac{\rho_d d_d^2}{18 \mu^g}, \tag{2.37}$$

and f is a correction factor [58] given by

$$f = \frac{\beta}{e^\beta - 1}; \tag{2.38}$$

$$\beta = -1.5 Pr \frac{\dot{m}_k^p \tau_d}{m_k^p}. \tag{2.39}$$

The droplet mass is governed by the following equation

$$\frac{dm_k^p}{dt} = -\frac{Sh}{3Sc} \frac{m_k^p}{\tau_d} ln(1 + B_M), \tag{2.40}$$

where B_M is the mass transfer Spalding number and is modeled according to the following relation,

$$B_M = \frac{Y_{d,s} - \widetilde{Z}_g}{1 - Y_{d,s}}. \tag{2.41}$$

$Y_{d,s}$ is the mass fraction of gas-phase fuel at the surface of the droplet,

$$Y_{d,s} = \frac{W_f X_{d,s}}{W_f X_{d,s} + W_g(1 - X_{d,s})}; \tag{2.42}$$

$$X_{d,s} = \frac{p_0}{p_{atm}} exp\left(L_v \left[\frac{1}{T_{b,atm}} - \frac{1}{T_{d,s}}\right]\left[\frac{W_f}{R}\right]\right). \tag{2.43}$$

W_f and W_g are the molecular weights of the gas and fuel, respectively. $X_{d,s}$ is the mole fraction of gas-phase fuel the surface of the droplet. The only unclosed portion of the model is $T_{d,s}$, the temperature of the gas phase fuel at the droplet surface, which is currently approximated as T_d. To obtain the filtered source terms for the Eulerian transport equations, the drag and evaporation of each droplet is summed within its respective cell.

2.3 Solution algorithm and low-Mach approximation

One of the deficiencies of OpenFOAM is its inability to solve a fully coupled system. In many other codes, a single block matrix containing the coefficients of all velocity components and pressure is constructed and solved, yielding a result which simultaneously satisfies all discretized equations within

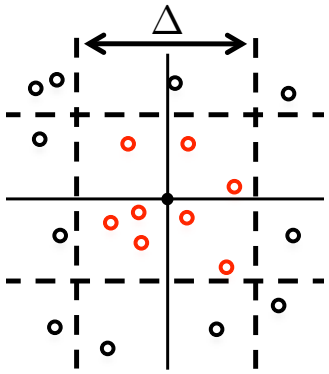

Figure 2.6: Droplets represented using point particle assumption

tolerances. However, a class of algorithms was created to solve this problem, whose decoupled equations circumvent the issue. These pressure-velocity coupling algorithms traditionally follow a form known as the predictor-corrector [16].

As the name somewhat suggests, the momentum equation is solved in an approximate sense, using either the old pressure field or neglecting it entirely. This returns a prediction of the velocity field, an intermediate value which satisfies a modified version of the Navier-Stokes. In order to calculate the pressure field from this intermediate velocity, an expression must be formulated from the equations already in hand. By taking the divergence of momentum and simplifying it using continuity, the equation below is obtained:

$$\nabla^2 \widetilde{p} = \frac{1}{\Delta t}\left(\frac{\partial \overline{\rho}}{\partial t} + \frac{\partial \overline{\rho}\widetilde{u}_j^*}{\partial x_j} - \widetilde{S}_\rho\right), \tag{2.44}$$

where $\widetilde{u}_j^*$ is the velocity prediction vector and continuity is again formulated for the presence of droplets. This Poisson equation can now be solved explicitly

for pressure. The gradient of the pressure field is subsequently applied to the intermediate velocity field in the corrector step. Many variations of the algorithm exist, such as SIMPLE, SIMPLER, SIMPLEC, PISO, etc [66, 88, 65, 35]. These variations alter the number of iterations, the convergence criteria, the order of calculations, and the pre-conditioners and relaxation factors.

At this point, no approximations have been made in the algorithm regarding the Mach number or compressibility of the flow. Pressure splitting can be used in both cases, and indeed PISO was developed as a compressible variant of SIMPLE. However, many problems arise when this algorithm is put into practice. The Poisson equation contains no time-history of pressure. As such, it can be prone to wide fluctuations between adjacent time steps. Additionally, the elliptic nature of the equation can disseminate local variations across the entire domain. In the case of high-Mach number flows, where pressure and density remain strongly coupled, these rapid changes have correspondingly unphysical thermodynamic effects, which often leads to catastrophic instabilities.

The low-Mach number approach removes compressibility effects from the governing equations [54, 53]. In the approximation,

$$p = p_0 + \delta p. \tag{2.45}$$

That is, the pressure field can be decomposed into a constant thermodynamic component (p_0) and a fluctuation (δp). If the fluctuations are small relative

to the ambient field, as is the case in a low Mach number problem, the decomposition holds. The effect of this approximation is subtle as far as the governing equation goes (2.46), but it vastly simplifies the thermochemistry, which no longer must contend with variable pressure. From a numeric perspective, this removes the potential for acoustic waves. This predictor-corrector algorithm in the context of low-Mach incompressible problems is known as a pressure-projection method,

$$\nabla^2 \widetilde{\delta p} = \frac{1}{\Delta t}\left(\frac{\partial \overline{\rho}}{\partial t} + \frac{\partial \overline{\rho}\widetilde{u}_j}{\partial x_j} - \widetilde{S}_\rho\right). \tag{2.46}$$

To summarize the algorithm used throughout the solver:

- **(Optional):** At the beginning of each time step, Lagrangian particles, if present, are evolved according to the ballistic equations. Evaporation and momentum terms are collected into volumetric fields to serve as sources. This evolution is done only once per time step for computational efficiency. The discrepancy associated with lagging the value of the Eulerian fields seen by the particles is an accepted error and assumed to be small.

- **Outside loop:** Mixture fraction, reaction progress variable, and total enthalpy are transported using the old values of the velocity and density. These values are therefore considered marginally incorrect. The thermochemical composition vector is updated from the chemistry table using these scalar values, which gives a slightly improved estimate.

- **Inside loop:** The velocity field is solved in the absence of pressure gradient, using updated values of density and viscosity. The pressure equation is solved using the intermediate velocity and density values. Now the pressure correction is applied to the intermediate velocity. The pressure and velocity fields are no longer consistent, so the inside loop is repeated to convergence.

- **Outside loop continued:** Mixture fraction, reaction progress variable, and total enthalpy must be solved again starting not from their intermediate values, but from the prior time step. The chemistry table look-up is repeated, followed by the inner loop. This outer loop is similarly iterated until all scalars, velocity, and pressure are consistent to within a convergence criterion.

Chapter 3

Channel Flashback Simulations

With the solver developed and models implemented, validation was extended to a three dimensional structured orthogonal geometry and a transient instability known as boundary layer flame flashback. A DNS conducted externally by Lawrence Livermore National Laboratory was used for comparison, with various qualitative combustion characteristics and statistical quantities examined.

3.1 Background

In lean premixed combustion of fuels with high hydrogen content, preventing flame flashback is an important design constraint. The high reactivity of hydrogen combined with enhanced flammability limits (compared to natural gas) promotes flame flashback of several types, including propagation along low-speed boundary layers adjoining the combustion walls [24, 30]. While this boundary layer flashback will be quenched by heat transfer to the walls, the combustor and premixing chamber walls may still sustain damage. Prior studies [19, 33] show that hydrogen flames are able to propagate three times closer to the wall before wall heat transfer quenches the flame. Since hydrogen-based

power generation is a significant component of pre-combustion approaches for reducing carbon emissions, understanding and preventing flashback is a top priority in the design of such combustors.

Theoretical studies in laminar flames [40, 41, 45] have identified a critical near-wall velocity gradient necessary to arrest flashback. This relation correlates the burning velocity at the leading edge of the flame, the distance of this edge from the wall, and the velocity gradient at the wall. In general, a turbulent boundary layer exhibits a higher critical gradient as compared to a laminar boundary layer, which could be the result of a reduced distance to the wall or an increased burning velocity due to the core turbulent flow [26, 25, 30]. Computational studies mainly focused on laminar boundary layer flashback [40, 41, 45], with increasing complexity of the underlying flow description. Recently, Gruber et al. [32] conducted the first direct numerical simulation (DNS) of flame flashback in a three-dimensional channel flow using detailed chemical kinetics. The simulation indicates that density changes associated with the flame strongly influence the propagation mechanism. Also, small reverse flow regions in front of the flame tend to accelerate it.

This discussion leads to an examination of the specific features of the flow which must be reproduced if the LES is to predict flashback correctly. This level of detail is present only in high-fidelity direct numerical simulation, which is invoked here in an *a posteriori* role in the form of a turbulent channel configuration simulated by Gruber, et al [32]. Such comparisons have their strengths and limitations which must be considered. While all DNS provides

extremely complete data sets about the entire flow field, an ideal scenario for model testing, it conversely cannot be used in the complex geometries and high Reynolds number flows seen in practical applications. Furthermore, because the DNS mesh is necessarily much finer than the smallest turbulence length scales (in order to resolve the flame front), it becomes a constraint in the context of the LES imposing minimum and maximum resolution requirements on the grid. Such issues will be discussed to some extent in this chapter, though its clear that for completeness, validation must reach beyond this configuration. With this background, the goal here is to assess the key physical characteristics that need to be represented in order to reproduce flashback using LES computations. A suite of computations is used to understand the interactions between the flame and flow field. Statistical quantities describing the structure of the flame front are used to evaluate LES performance.

3.2 Case details

3.2.1 DNS configuration

Figure 4.2 shows a schematic of the flow configuration used in the DNS. The domain measures $6.0\,\text{cm} \times 1.2\,\text{cm} \times 3.6\,\text{cm}$ in the streamwise, wall-normal, and spanwise directions, respectively, with $2400 \times 480 \times 1440$ points corresponding to each of those dimensions. Since all fields are fully resolved, no cell growth is used in the near wall regions, giving a uniform spacing of $\Delta = 2.5 \times 10^{-5}\,\text{m}$. The inflow mixture was fed through the inlet face indicated by the arrow with a bulk velocity of $20\,\text{m/s}$ leading to a Reynolds number of

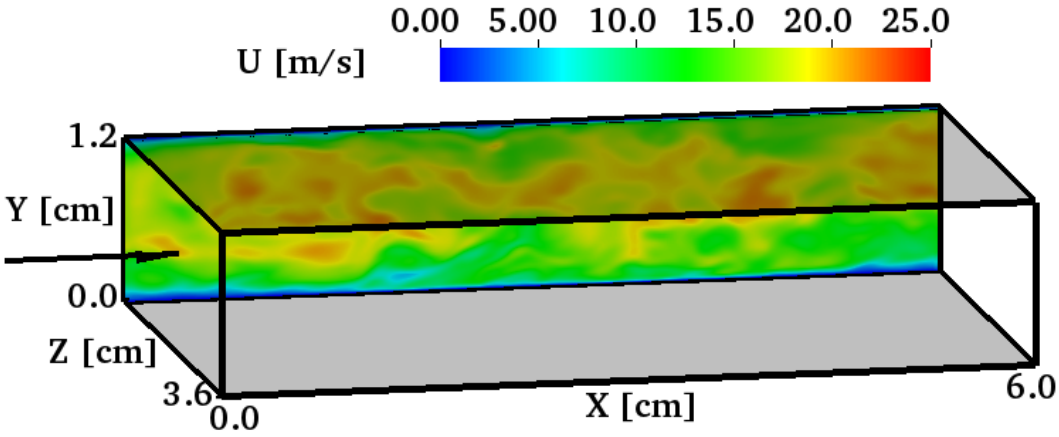

Figure 3.1: Schematic of the channel with X, Y, and Z axes corresponding to streamwise, wall normal, and spanwise directions respectively. Also indicated are the direction of flow (arrow), walls (gray), and instantaneous inert velocity contour (Z = 0.0 cm plane).

3200 based on channel height. The inflow was a temporally evolving turbulent velocity field extracted from an auxiliary inert DNS. This simulation was run with periodic boundary conditions which reached a statistically stationary state with reduced computational expense given its requirement of resolving only turbulence and not combustion. The flow field was allowed to develop turbulence inside the channel for a finite time before being interpolated to the finer grid. The flame front was initialized at the X = 4.5 cm plane.

The composition of the inflowing mixture was premixed hydrogen-air with an equivalence ratio of 0.55 and an inflow temperature of 750 K. The flame initialization was accomplished using a one-dimensional laminar flame profile, calculated externally and superimposed over the turbulent flow. The

streamwise velocity component was subsequently adjusted to account for the density change. The hydrogen combustion was simulated using a 9-species, 19-step reaction mechanism [47] solved using the FlameMaster chemistry tool. Although the configuration is slightly modified from that of [32], all other computational details remain the same.

Figure 3.2 shows a sample instantaneous flame front contour for the last available data set. Because of the physically unrealistic way in which the flame was initialized, some settling time was necessary to allow pressure oscillations to diminish. Additionally, early DNS time steps indicate that the flame in the centerline region moves significantly downstream before the boundary layer flashback catches and pulls the central front with it. Collection of useful statistics should therefore occur after the initial transient front development and the upstream propagation velocity has become roughly uniform. The leading edge of the flame during this temporal window is displaced by roughly 5.0 mm. Note that in this duration, the flame front motion is almost uniform allowing for temporal averaging in collecting statistics.

3.2.2 LES implementation

The LES closely follows the implementation used in the DNS. The dimensions of the channel were kept the same, with the grid resolution varied for the purpose of testing its effects on overall flame behavior in the context of the models used. In this work, the various sizes are referred to relative to the DNS grid, that is, 4Δ, 8Δ, and 16Δ rather than 1×10^{-4} m, 2×10^{-4}

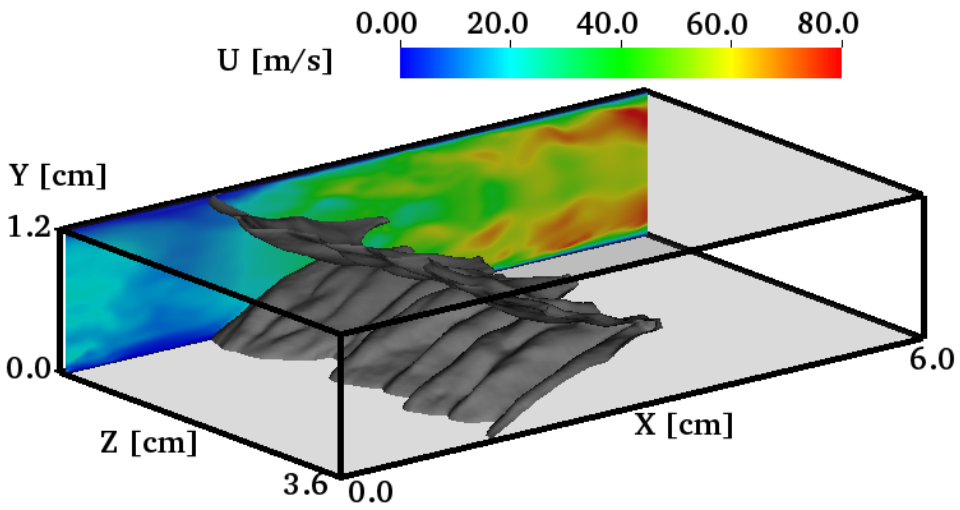

Figure 3.2: Instantaneous isocontour of T = 1400 K (gray) with velocity field at t = 2 ms.

m, and 4×10^{-4} m. A unique situation arose in simulating this case on progressively coarser grids. Given the high initial resolution used in the DNS which greatly over resolves the turbulence in order to capture the flame scales, the LES had a low upper limit to cell size. Even in the 16Δ case, which reduces the number of points used in the wall normal direction to 30, turbulence is still mostly resolved. Because of this, analysis was necessarily limited to combustion models rather than combustion/turbulence model interactions, an increasingly common simulation type as computational resources grow [28].

The LES equations were discretized using an Euler implicit scheme for time advancement. Diffusion and convections terms for mixture fraction, reaction progress variable, and total enthalpy used a second-order central difference scheme with a Sweby limiter [84], in order to encourage stability and enforce

bounded solutions. The same flux-limited second-order schemes are used in the momentum equation with an additional term used to correct for interpolation to the face centroid rather than the intersection of the face and the line connecting adjacent cell centers [20]. This is common practice in unstructured codes. Additionally, gradients are computed using second-order least squares rather than Gaussian integration, which does not guarantee second-order convergence on arbitrary meshes. While the QUICK scheme [44] is widely used in unstructured grids due to its third order convergence, dissipation errors arising from its usage necessitate an alternative approach.

As stated previously, the combustion model uses a flamelet generated manifold with a mixture fraction, reaction progress variable, and total enthalpy solved via scalar transport equations. These equations were closed using the F-TACLES procedure [7]. Additionally, the mixture fraction variance is required to fully define the β-PDF used in the filtering. An algebraic model with a dynamically calculated coefficient was used to calculate it [68]. The flamelet chemistry table was generated using the same chemical reaction mechanism used in the DNS. Regarding turbulence, the dynamic variant of the Smagorinsky model was used to model sub-filter stresses [31, 49, 79]. As mentioned previously, however, the high grid resolution eliminates most of the effects from this term.

Regarding boundary conditions, the same inflow velocity slices used in the DNS were applied here as well, interpolated to the coarser grids as necessary. This inflow was allowed to fully develop before initializing the flame.

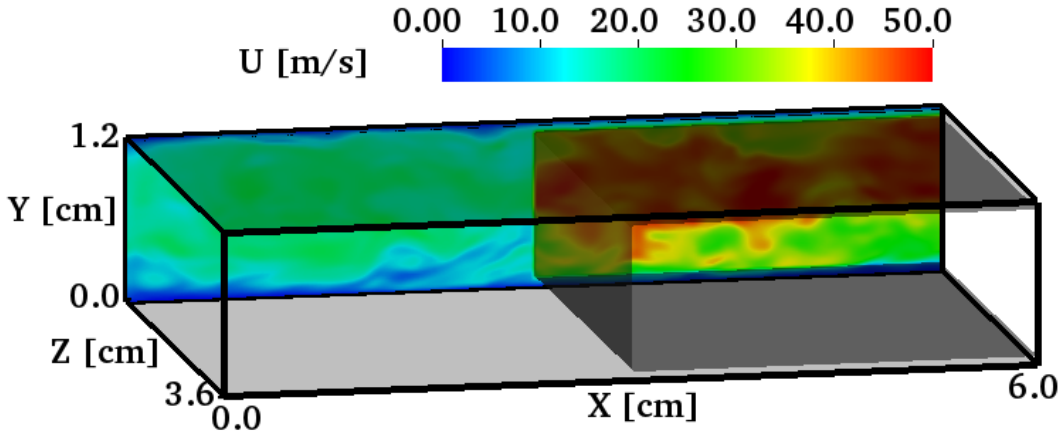

Figure 3.3: Instantaneous plot of corrected velocity field with initial isocontour of C = 0.7 (gray).

Given the flamelet based combustion model, initialization was slightly different than DNS. To initialize the reaction, a one-dimensional adiabatic flame was calculated externally using the FlameMaster code [70]. The thermochemical composition vector (temperature, density, viscosity, etc.) was remapped into mixture fraction, reaction progress variable, and total enthalpy space before being superimposed over the flow field. The streamwise velocity component was corrected to satisfy continuity. The initial flame front and the corrected velocity field are shown in Figure 3.3. Notice the flame extends from the central plane directly to the outlet, touching neither the top nor bottom walls. This was done to satisfy the fixed temperature at the wall while avoiding large initial gradients.

3.3 Results

The suite of calculations presented in this section examines the ability of a detailed LES to recreate the same qualitative and quantitative behavior of the DNS. Previous studies have indicated that the F-TACLES closure model previously described is well equipped for the present problem and will be applied here. The study will progress as follows. First, a baseline case will be considered, which uses all options present in the solver, namely heat loss and differential diffusion effects. Several mean quantities will be extracted and compared against the DNS results for validation. Second, the effects of varying grid resolutions will be described, with both refined and coarsened meshes used in an otherwise identical set-up. Finally, the role of heat loss and differential diffusion on both the general behavior and overall statistics will be considered. Additionally, it should be noted that all calculations were repeated for several different inflow conditions without appreciable effect. This implies front propagation is an accumulated interaction with multiple eddies over the resolved time scales and variability due to initial conditions is eventually washed out.

3.3.1 Validation using DNS

The baseline LES compared against the DNS for purposes of validation used a grid of 8Δ. Recall, Δ in this case is the length of one edge of the DNS, so the LES used a resolution of $300 \times 60 \times 180$ or 3.24 million cells. Figure 3.4 shows both LES and DNS isolines of progress variable at the earliest and latest time for which the DNS data is available. The flames follow the

same behavior, with the core flame being swept back from its starting position while the near-wall flame propagates upstream. Eventually, the front reaches a quasi-steady state depth after which it propagates as a coherent V-shaped structure. In examining the coming plots, several differences between the two will become apparent. First, the DNS field achieves greater post-flame speeds than the LES. Second, the DNS also deepens faster, reaching its final flame depth earlier. Clearly, the two cases have different characteristic evolution times, indicating a slower overall growth in flame wrinkling and stretch in the LES. These consequences are expected to impact the propagation speed.

In both DNS and LES, flow is diverted away from the wall by the flame induced blockage, essentially funneled to the cusp of the V-shaped front. Figure 3.5 shows this clearly, with streamlines seeded uniformly in the wall normal direction and clustering upstream of the flame. As the flow is redirected, it accelerates along the channel centerline. Passing through the flame, it accelerates further, reaching speeds beyond those exclusively due to expansion. Examination of the result earlier in the simulation corroborates this idea, where the flatter front yields a post-front velocity with the density scaled turbulent channel flow velocity. As the front develops the correct flame shape, these speeds gradually increase to match those of the DNS.

Flow redirection is not limited to the plane normal to the spanwise direction. Indeed, referencing Figure 3.5 again, there are large regions upstream of the front with no streamlines passing through, indicating either a recirculation zone or flow which originates from far out of the plane. The former

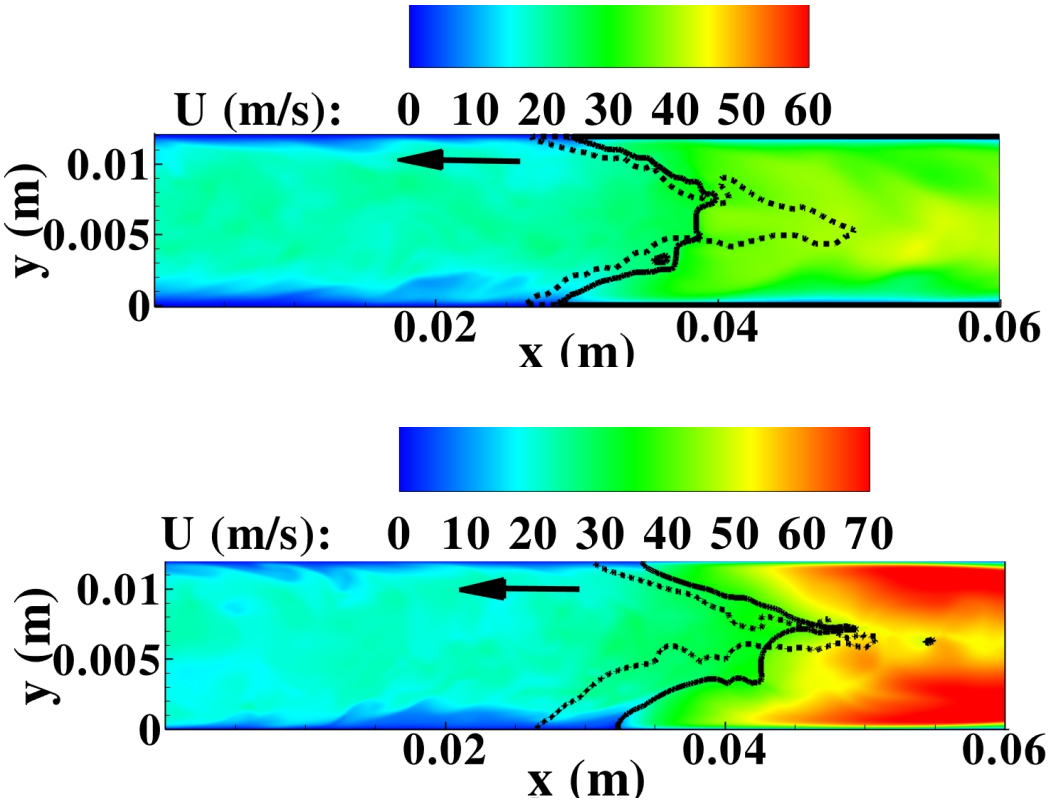

Figure 3.4: Instantaneous LES (top) and DNS (bottom) contours of streamwise velocity at 0.8 ms at the $Z = 1.8$ cm plane. Isolines of T = 1400 K shown at 0.8 ms (solid) and 1.4 ms (dashed).

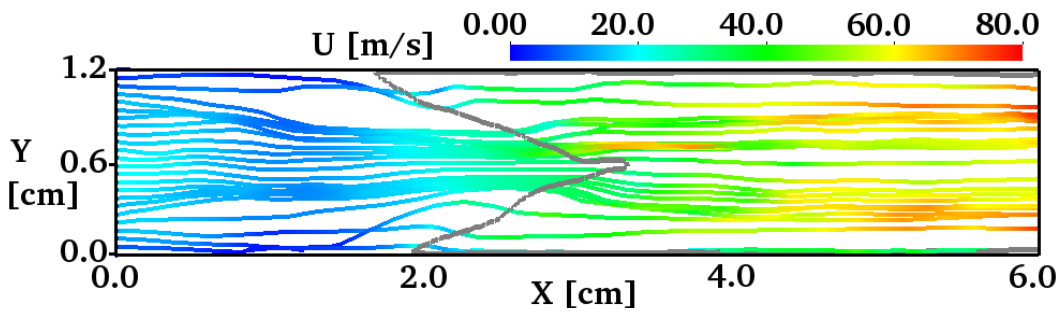

Figure 3.5: Instantaneous LES streamlines colored by velocity magnitude and an isoline of the flame front (gray) at the $Z = 1.8$ cm plane.

is easily disproven (and latter proven correct) by seeding a streamline within that space, as seen in Figure 3.6. In an instantaneous sense, the unburnt mixture flows around the flame, along the path of least resistance toward the valleys between adjacent bulges. It is clear that the trailing points of the flame front therefore see the highest flow speed. After passing through the flame, the streamlines are diverted again, this time in the direction normal to the flame surface. The combination of acceleration both pre- and post-flame yields an increased wrinkling which only grows as the flame wrinkles. That is, as the front develops its shape, the foremost near-wall regions see a slower oncoming velocity (which may include reverse flow areas) while lee-most core regions see faster oncoming flow. This self-sustaining growth feature is called a Darrieus-Landau instability.

Consider now the shape of the front itself. Figure 3.7 shows instantaneous three-dimensional isosurfaces of progress variable for both the LES and DNS. Clearly the DNS surface exhibits a wider range of scales with

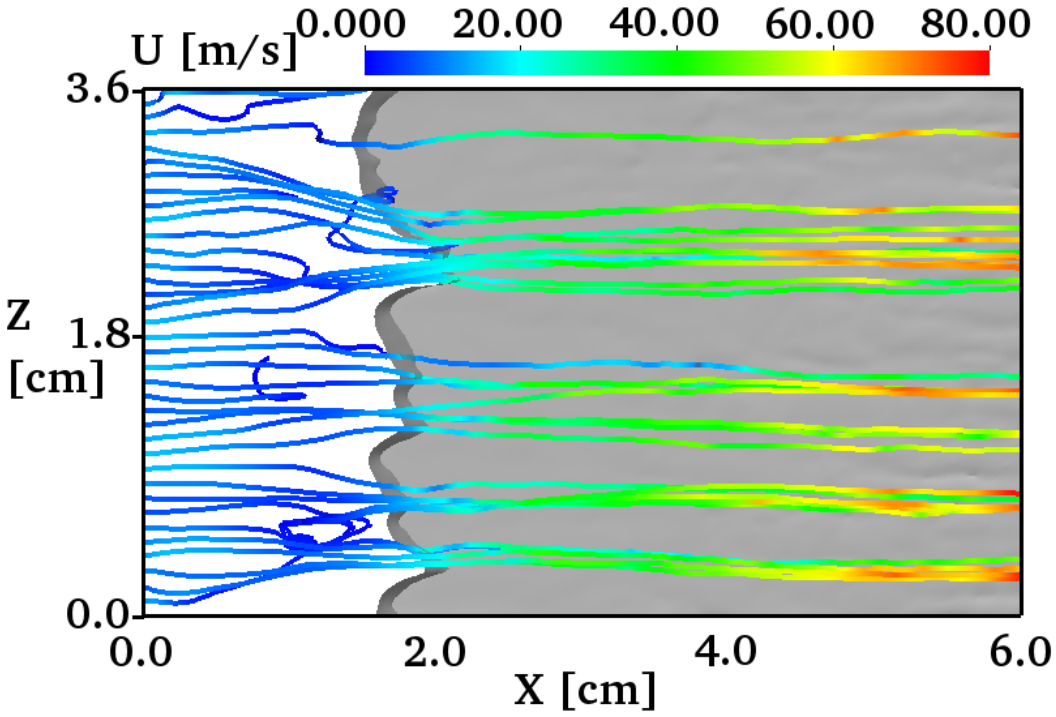

Figure 3.6: Top down instantaneous LES streamlines seeded at the Y = 1.0 mm plane and colored by velocity magnitude. The gray region indicates the fully burned zone.

smooth variations on the surface interspersed with small scale fluctuations in the streamwise location of the flame front. That its surface is more wrinkled than the LES is to be expected, given the increased resolution of the DNS. In addition, the positive curvature regions near the wall that tend to accelerate the flame are more pronounced with deeper troughs along the streamwise direction. Although the LES flame surface exhibits similar troughs, they are considerably shallower. As a consequence, the spanwise variation in the flame front location in the near wall region is smaller compared to the DNS case.

To further understand the LES results, some qualitative metrics of the flame must be defined. Here, the evolution of the distance between the leading and trailing edges of the flame, hereafter referred to as the flame depth, is studied. For the purpose of this discussion, the leading edge is the first point in the streamwise direction containing a non-zero progress variable, while the trailing edge is the last grid point in the streamwise direction which contains a zero progress variable. By this definition, the initial planar flame has a depth of Δ. The quantity is useful in that it incorporates the cumulative effect of the core velocity on the propagation characteristics. Note that in the boundary layers where the flow field is nearly laminar, propagation is mainly at the laminar flame speed (adjusted for quenching effects), while in the core flow, turbulent flame wrinkling will lead to turbulent-velocity based propagation.

Figure 3.8 shows the spanwise-averaged depth as a function of time. For the LES, this quantity increases slowly, but ultimately reaches a quasi-steady state value after 1.0 ms. While the depth in the DNS during this

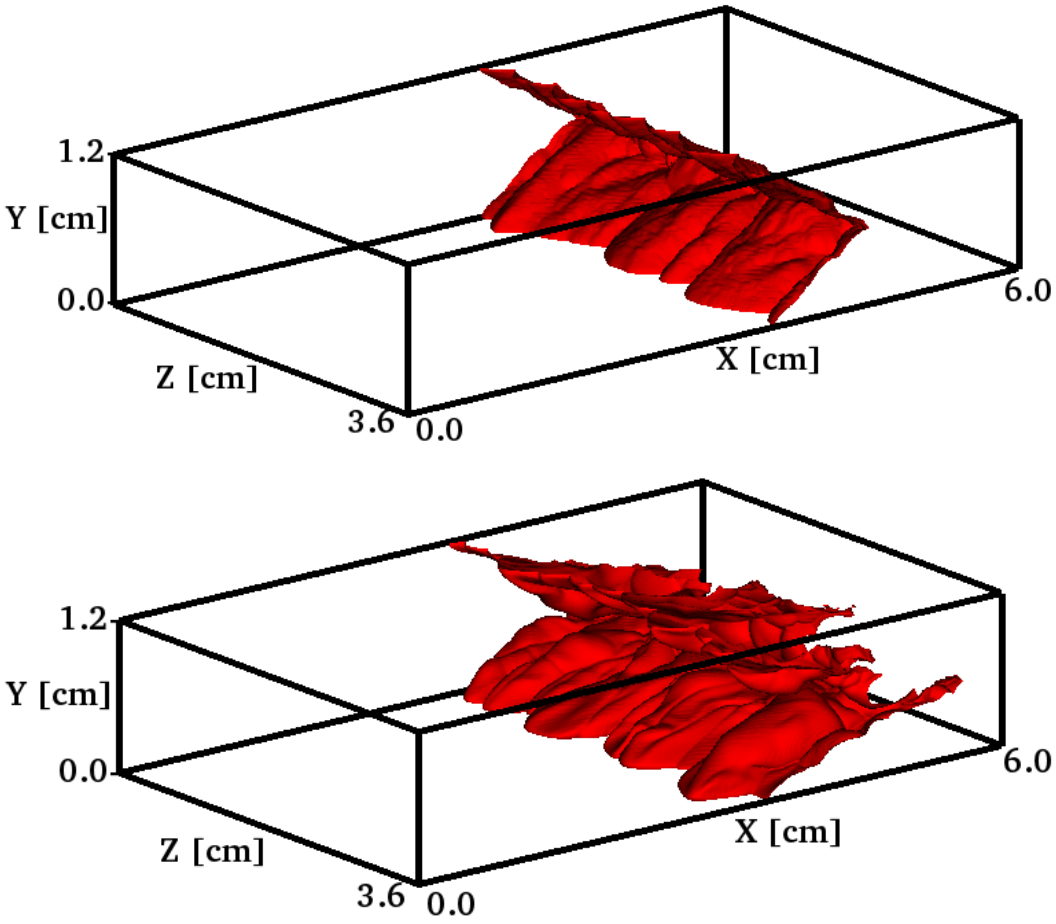

Figure 3.7: Instantaneous isocontour of C = 0.7 for LES (top) and DNS (bottom) for t = 0.8 ms.

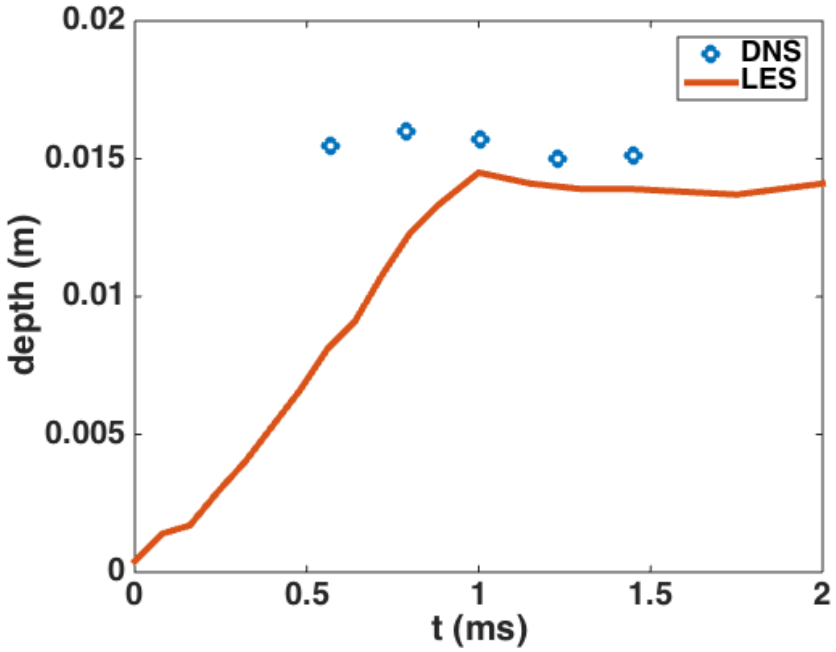

Figure 3.8: Plot of spanwise averaged depth parameter as a function of time for DNS (circles) and LES (solid line).

interval is around 15 mm, the LES under predicts this slightly, averaging only 14 mm. More revealing of the behavior of the flame is the growth rate indicated early in the plot. While no DNS data sets exist prior to 0.5 ms, growth can be expected to be roughly linear, with a slope at least double that seen in the LES, in agreement with the previous assertion that the two simulations yield different characteristic evolution time scales. This variation can arise from several sources. By combining the information gained from Figures 3.4 and 3.7 and the understanding of the velocity field variations as a result of the flame, clearly the DNS, in resolving the flame surface, more accurately predicts wrinkles and corrugations. Such fluctuations in the front have large consequences on the turbulent velocity field, because of the Darrieus-Landau instability. Therefore, only a better resolved flame front is expected to capture the same growth. That the two depths eventually reach similar values regardless is a strong indication that these effects are of importance only for initial flame development.

Defining the global propagation speed as the variation in mean position over time, several connections can be made with regards to both the DNS results and the flame depth parameter previously discussed. Figure 3.9 shows this metric as a function of time over the same range as the depth plot. As mentioned, there are no early data sets to determine the speed of the DNS prior to 0.5 ms. The LES curve indicates that the flame is initially convected downstream, having a negative propagation speed, before the flashback takes hold. As the flame increases in depth, which is accompanied by increased

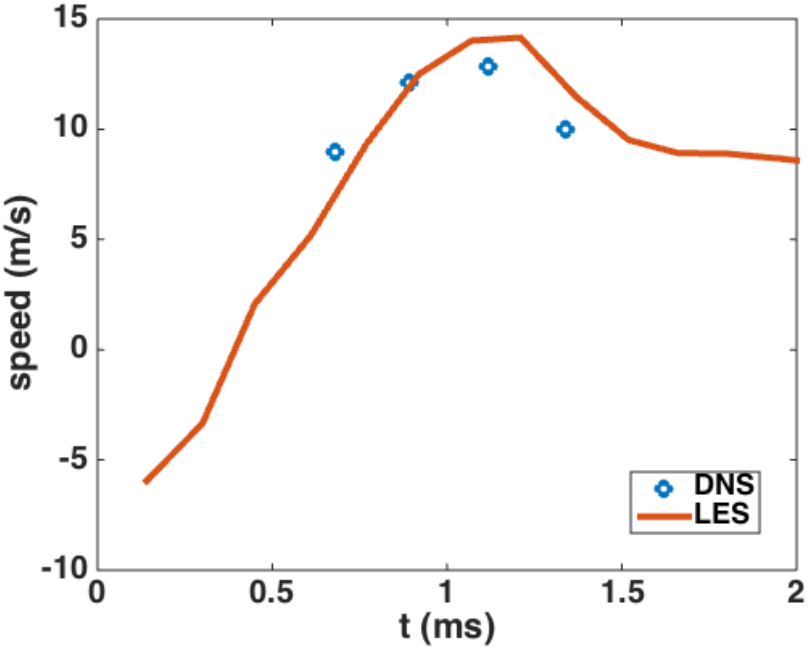

Figure 3.9: Plot of average flame speed in the normal direction as a function of time for DNS (circles) and LES (solid line).

wrinkling, the flame speed also grows before reaching a peak value. As the flame reaches its quasi-steady state depth, the front speed steadies as well. The DNS, fully resolving such small scale structures, continues to see fluctuations in the velocity field and corresponding variations in flame speed.

A related quantity of interest is the fluctuation of the flame front location in the streamwise direction about the spanwise-averaged flame front location. Figure 3.10 shows the PDF of the flame location in both DNS and LES computations. It is seen that the LES-based PDF roughly matches the near-Gaussian DNS-based PDF. However, the probability of large fluctuations

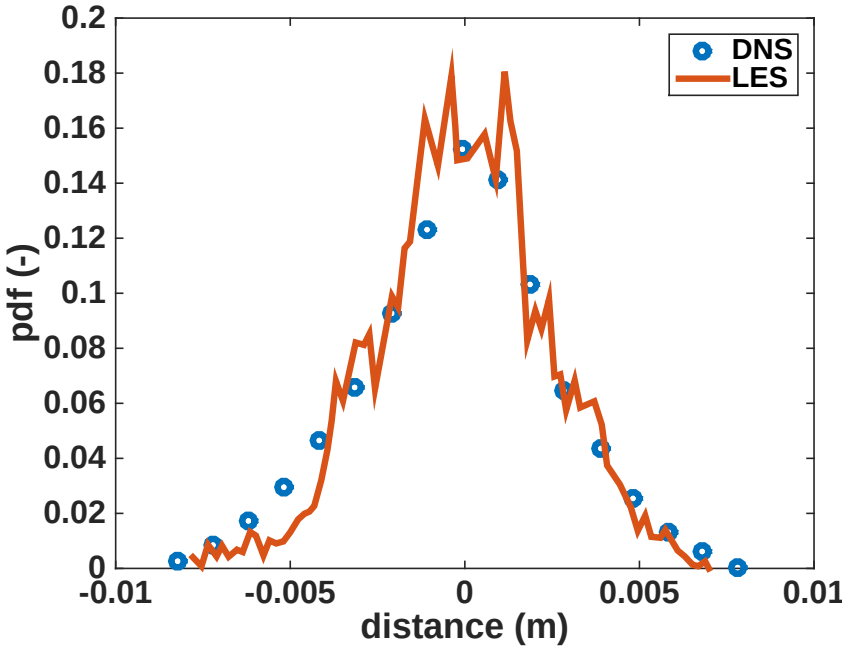

Figure 3.10: PDF of streamwise distance from the mean position for the C = 0.7 isosurface for DNS (circles) and LES (line) after reaching quasi-steady state.

in LES is marginally lower than the DNS probability. Overall, the baseline LES is able to capture many of the details of the flame front albeit with different initialization locations.

3.3.2 Effect of LES grid on propagation

Several alternative meshes were considered in addition to the 8Δ resolution. The first was uniformly spaced with a larger filter width, 16Δ being twice as coarse in each direction for a total of 405000 cells. Additional variations of the two uniform meshes were created with the same number of cells,

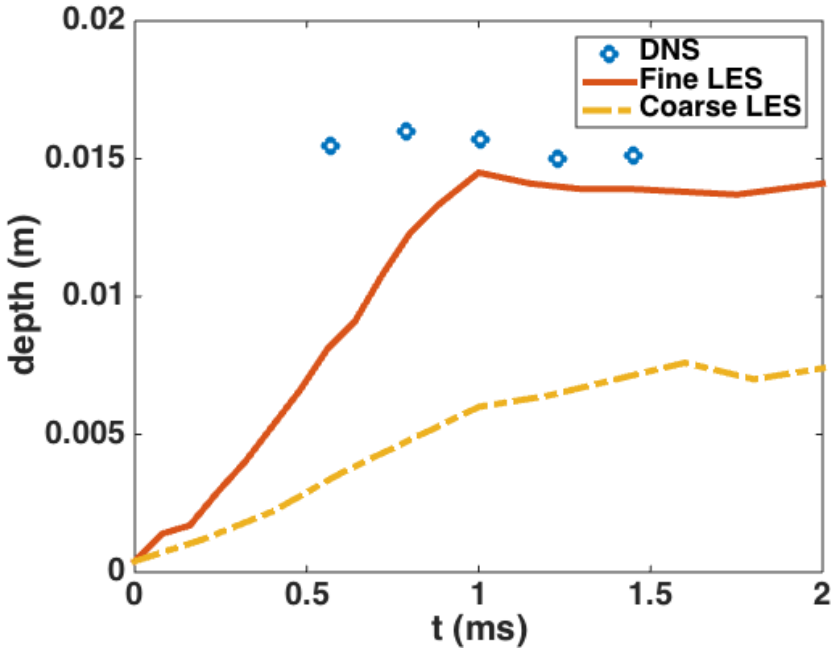

Figure 3.11: Plot of spanwise averaged depth parameter as a function of time for DNS (circles) and LES with F-TACLES at $\Delta/\Delta_x = 8$ (solid line) and $\Delta/\Delta_x = 16$ (dashed line).

but grading in the wall normal direction yielding half the filter width as compared against their respective uniform grids. Meshes beyond 16Δ (e.g. 24Δ) failed to yield any kind of flashback, with the flame getting washed out of the domain. In the cell-growth cases, the higher near-wall resolution had no effect on the flame speed nor the depth parameter as compared to their respective uniform meshes. This is somewhat counterintuitive, as the flashback behavior is intrinsically linked to the near wall region and a better resolved flame is expected to alter the resulting propagation. This suggests that beyond some minimum grid requirement, additional points fail to introduce new physics capable of altering the flame dynamics.

Considering now the variation between filter-widths of 8Δ and 16Δ, Figure 3.11 displays a wide discrepancy, indicating that the evolution of the depth parameter is more faithfully reproduced on the finer grid while the coarser one vastly under predicts it. Additionally, the time scales again suffer as the 16Δ case continues to grow for nearly 1.5 ms before reaching quasi-steady state. This observation is verified in the propagation speed plot, where the coarse case takes longer to reach a steady speed which is nevertheless far lower than expected. Again, the lack of resolution both near-wall and in the core of the flow diminishes the ability to successfully capture the front wrinkling. Because of this, the resulting smoother flame can attain neither an appropriate depth nor speed.

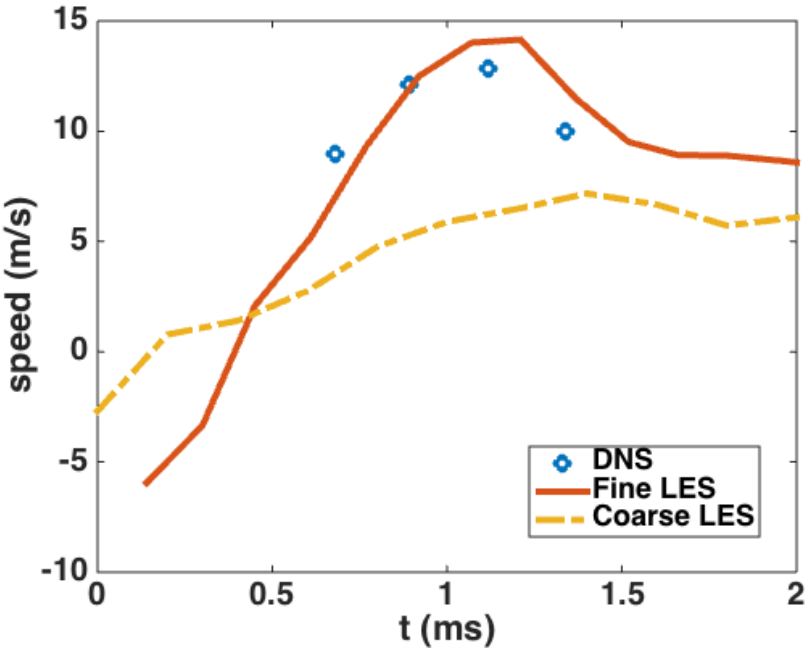

Figure 3.12: Plot of spanwise averaged velocity as a function of time for DNS (circles) and LES with FTACLES at 8Δ (solid line) and 16Δ (dashed line).

3.3.3 Effect of heat loss on statistics

Boundary layer channel flashback is widely assumed to depend not only on good resolution of the near wall region, but also a combustion model which incorporates boundary effects there. The baseline case in this work made use of total enthalpy lost to the surface. However, it is worthwhile to briefly examine to what extent heat loss truly affects the overall results, if at all. While the DNS fixes the temperature of the wall to 750 K, using an adiabatic boundary condition in the LES is a relevant consideration given the increased difficulty of incorporating heat loss into the model. In an industrial world, the accuracy gained by its usage may not outweigh the increased expense, which is generally not trivial.

For this reason, additional cases were run on the various meshes described above, but with the fixed temperature boundary condition removed. First, the evolutionary time scales increase slightly from the heat loss cases, indicating that the early development until quasi-steady state depends not only the grid but also shows some sensitivity to the raised temperatures at the wall. In considering the asymptotic temperature value for the adiabatic flame, the differences become more prominent. The removal of heat loss increased the flame depth by up to 15%, with the flame propagation speed rising accordingly by 0.8 m/s. By removing heat loss to the wall, the progress variable source term in those regions increases, allowing the flame to travel faster there. This yields the greater growth rate, depth, and overall speed.

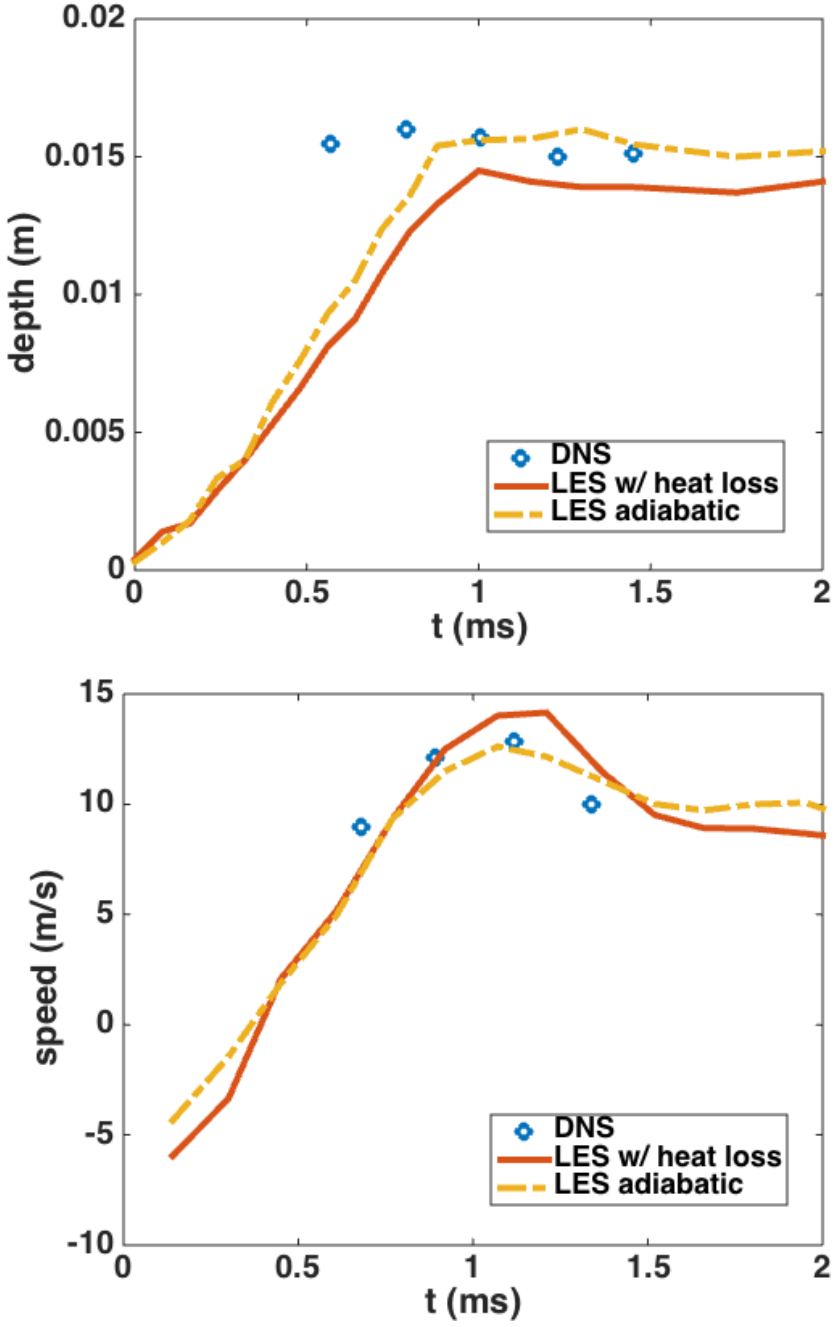

Figure 3.13: Plot of spanwise averaged depth parameter (top) and flame speed (bottom) as a function of time for DNS (circles) and LES with wall heat loss (solid line) and adiabatic walls (dashed line).

3.4 Conclusion

A suite of LES computations was used to understand the modeling of boundary layer flashback in relatively low Reynolds number turbulent channel flow. The LES filter widths were comparable to the smallest turbulence length scales, which would imply that the momentum description is reasonably accurate in the LES. The flame, on the other hand, was approximated as a thin front. In this sense, the computations were designed to test the interaction of this thin-flame assumption with the nearly fully resolved flow. The computations offered several insights. The baseline case at filter width of 8Δ produced a flame front comparable in statistics to that of the DNS. Using quantities such as the depth parameter and the PDF of front fluctuations, it was found that the LES computations are accurate in predicting the structure of the turbulent flame front, but not necessarily its characteristic time scales. Regarding small length scales, the LES flame was significantly less wrinkled, with bulges and cusps much shallower than the in the respective DNS. This is expected, given that the chemical source term is the predominant quantity in the progress variable transport equation. However, with regards to the whole time domain, this development is reasonably short, after which an accurate estimate of the flame speed is reached.

These observations indicate that although the flame is well represented by the flamelet model, some physical behaviors are lost in propagation mechanisms between the near-wall region and the center of the channel. Even at a coarser grid density (up to the indicated cut-off), flashback was predicted,

indicating that flame propagation through the boundary layers can be captured with some minimal resolution. Interestingly, additional mesh variations on these basic computations (wall normal cell growth) did not produce any changes to the flow. In particular, adding more points to the near-wall region did not change the depth or the velocity of propagation. Additionally, starting the calculation from different initial conditions led to almost no perceptible difference in these characteristics of the flame.

Based on these results, the requirements to capture the flashback process could be divided into three parts. First, there should be sufficient resolution near the wall to represent the actual V-shape of the flame, and at least approximately, the transition to a laminar flow. Combined with the density change across the flame, this creates a blockage to divert the flow towards the center. Second, the blockage-created centerline acceleration in the core of the channel is necessary to maintain the V-shape of the flame. Third, the combustion model should ensure that the core is not pushed downstream with the flow. In other words, the transition from a fully laminar to, possibly unresolved, wrinkled flame needs to be captured. However, the requirements for obtaining the correct propagation velocity seem to rely on the details of the model. For instance, the modulation of the small-scale turbulence by the density change across the flame front needs to be included in the closure model, in order to accurately represent the specific features of a flashback in a rectangular channel.

Chapter 4

UT Swirl Burner Simulations

Using the validated solver, a more realistic application is studied in the form of a swirl burner with premixed inflow. The capabilities of the code are examined in the context of a unstructured polyhedral grid, varying fuel compositions, and complex flow physics. While many of the same phenomena are examined as in the previous chapter, with boundary layer flashback again the focal point, there are additional complications. In contrast to the channel, detailed experimental measurements are used here for comparison.

4.1 Background

As discussed previously, lean premixed combustion of fuels with high hydrogen content can be prone to instabilities such as flame flashback and must be designed accordingly. Increased flammability promotes propagation close to the wall which could easily damage such surfaces. In order to design robust combustors, tractable models that can predict flashback for a complex combustor geometry and operating conditions would be very useful. While many detailed computational models have been used to study other flashback modes, such as propagation through combustion-induced vortex breakdown

(CIVB) in swirl burners [85], a similar focus on boundary layer flashback in these same burners is missing. Due to the inherent three-dimensional and unsteady nature of flame flashback in a swirling flow, the LES approach provides the best starting point for modeling. Since LES resolves only the large scales, and the flame/boundary layer interaction occurs exclusively at the small scales, subfilter models should be able to handle the impact of density changes on flame and fluid propagation. In the simulations of vortex breakdown based flashback, it has been found that existing models reproduce flashback with reasonable accuracy, but unphysical near-wall flame propagation could be introduced by the nature of the chemical source term closures used [80, 86, 85]. In these studies, flashback occurs primarily in the core of the flow, away from the walls, and subfilter closures based on the assumption of local equilibrium could be invoked without introducing appreciable errors. In boundary layer flashback, such assumptions must be assessed in order to determine the accuracy of equilibrium-based subfilter models.

The high-fidelity DNS channel [32] and accompanying LES provide many insights into the conditions which must be fulfilled in order to predict flashback. For instance, resolution requirements for the filter width are known to strongly affect the results and are difficult to satisfy in practice. Additionally, the presence of characteristics such as flame bulges and flow redirection upstream of the front serve as good qualitative indications of accurate simulation. To build upon the results of the channel study, the techniques and models must be applied to a more complex gas turbine geometry using realistic condi-

tions. For that purpose, a swirl burner was built at the University of Texas at Austin and tested using methane and hydrogen fuels [22]. The current study is limited to atmospheric pressure, though the experimental apparatus has been successfully run in a high pressure environment. An extensive set of data was collected and used for comparison against the suite of LES computations discussed here. Several quantities describing the structure and flashback speed of the flame front are used to evaluate LES performance.

4.2 Case details

4.2.1 Experimental configuration

Figure 4.1 shows an image of the experimental configuration. The burner consists of three sections: a plenum, a toroidal mixing tube, and a combustion chamber. Only the latter two comprise the computational domain. The mixing tube has an outer diameter of 5.1 cm, an inner diameter of 2.54 cm, and a length of 15.0 cm. Eight vanes are evenly spaced around the central body, extending to within 1 mm of the outer wall. Six 3.175 mm diameter ports (3 on the top and 3 on the bottom) are located on each vane, allowing for auxiliary injection in the event of partially premixed cases. However, in the experiments considered here, these ports are unused and air and fuel are premixed upstream before passing through a flow straightener and entering the mixing tube through the inlet face as shown by Figure 4.2. As the mixture flows upward, it encounters the vanes, which impart a swirl that continues throughout the tube and weakens considerably upon expanding into

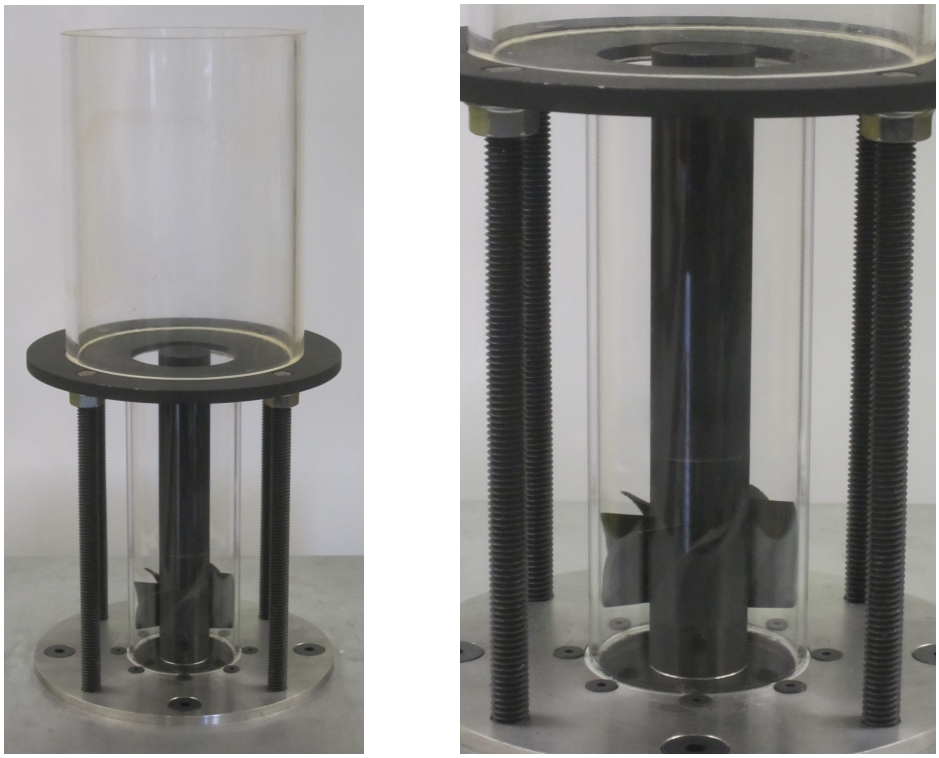

Figure 4.1: Experimental combustor showing full combustion chamber, and mixing tube and vanes (left) and detailed view of mixing tube and vanes (right).

the combustion chamber. The chamber itself has a diameter of 10.0 cm and a length of 15.0 cm, with flow exiting through the red face into the atmosphere. The expansion causes vortex breakdown, yielding a low velocity core which holds the conical flame in the stable case.

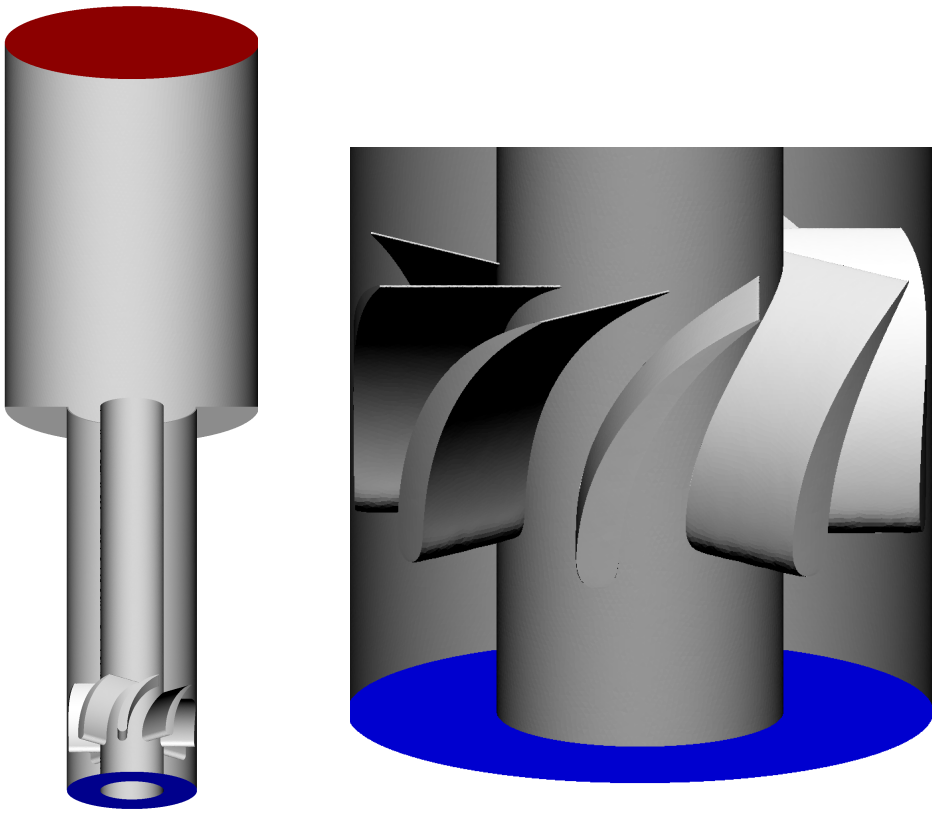

Figure 4.2: Full combustor geometry (left) indicating inlet (blue) and outlet (red) and detailed view of mixing tube vanes (right).

4.2.2 Computational implementation

As addressed above, the simulations eliminate the plenum and flow straightener, leaving only the mixing tube and combustion chamber. In order to construct the mesh, CAD files were obtained directly from the experimental design. Several mesh sizing parameters were considered. First, the combustion model requires a minimum resolution, ideally a minimum of four or five points through the flame thickness. For both methane and hydrogen/methane mix-

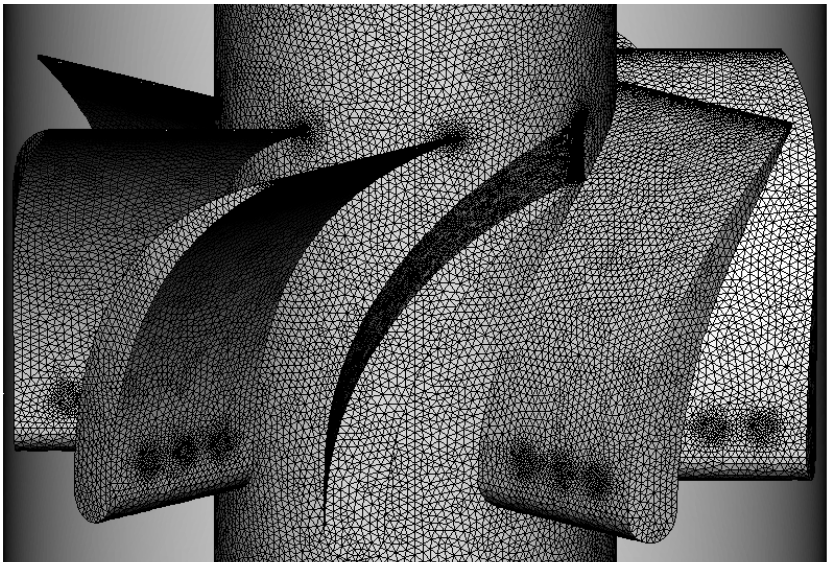

Figure 4.3: Detailed view of mesh in the vicinity of the turning vanes indicating clustering near bluff body and trailing edges.

tures, the laminar flame thickness is roughly 0.5 mm. Furthermore, given that wall effects were not explicitly considered by the turbulence or combustion models, cell clustering near the bluff body and vanes was required to ensure proper resolution of turbulence and small scale flow structures (Figure 4.3). In order to ensure a $y+$ value on the order of unity, an appropriate characteristic grid sizing is $\Delta = 0.1$ mm. Nearer the core, this value was allowed to grow to $\Delta = 0.2$ mm, while within the combustion chamber cells reached sizes as large as $\Delta = 2.5$ mm. In the latter case, where no qualitative measurements were extracted, sizing was less critical. The resulting mesh, created using the ANSYS meshing tool and converted appropriately using OpenFOAM utilities, contained roughly 7 million polyhedral cells.

The LES equations were discretized similarly to the chamber, with time advanced first order implicitly. Diffusion and convections terms for mixture fraction, reaction progress variable, and total enthalpy used a second-order bounded central difference scheme. Regarding the momentum equation, the same flux-limited second-order schemes are used with an additional term used to correct for interpolation to the face centroid rather than the intersection of the face and the line connecting adjacent cell centers [20]. This is common practice in unstructured codes. Additionally, gradients are computed using second-order least squares rather than Gaussian integration, which does not guarantee second-order convergence on arbitrary meshes.

As stated previously, the combustion model uses a flamelet generated manifold with a mixture fraction, reaction progress variable, and total enthalpy solved via scalar transport equations. These equations were closed using the F-TACLES procedure [7]. Additionally, the mixture fraction variance is required to fully define the β PDF used in the filtering. An algebraic model with a dynamically calculated coefficient was used to calculate it [68]. Regarding turbulence, the dynamic variant of the Smagorinsky model was used to model subfilter stresses [31, 49, 79]. Near the outflow of the combustion chamber, this artificial viscosity provides a much needed stabilizing effect typically used in low-Mach number solvers.

For hydrogen combustion, a 9-species 19-step mechanism was used while for methane a 6-species 4-step mechanism was used [47, 83]. Reynolds numbers were matched between the two cases, while the equivalence ratio was

varied to yield the same laminar flame speed of 26.0 cm/s. A fully turbulent flow field was allowed to develop inside the domain before the reaction was initialized. The turbulent inlet boundary condition was created using an auxiliary simulation, a periodic channel annulus with high Reynolds number which was sampled and subsequently fed into the swirler. The remaining boundary conditions for the cases discussed are summarized in table 4.1. It should be noted that methane was mixed with the hydrogen fuel for experimental visualization purposes. However, this dilution was subsequently proven a necessary addition in arresting the flame speed, as a pure hydrogen fuel rich enough to burn would not stabilize in the combustion chamber for any equivalence ratio.

To initialize the reaction, a one-dimensional adiabatic flame was calculated externally using the FlameMaster code, as seen in Figure 4.4 [70]. The thermochemical composition vector (reaction progress variable, density, viscosity, etc.) was superimposed over the fully developed turbulent flow field, yielding a spherical flame with a finite thickness within the recirculation zone in the core of the flow. The velocity was corrected to satisfy continuity. These initial fields are shown in Figure 4.5. Various methods of ignition were explored and found not to effect the flame stabilization and upstream propagation. Thus, this procedure was used due to its stability properties and the ease with which the flame could be ignited without fear of being washed out of the domain. In all cases the flame traveled through both the boundary layer and the low speed core of the flow, eventually stabilizing on the bluff body. In order to transition from the stable flame to flashback, the equivalence ratio

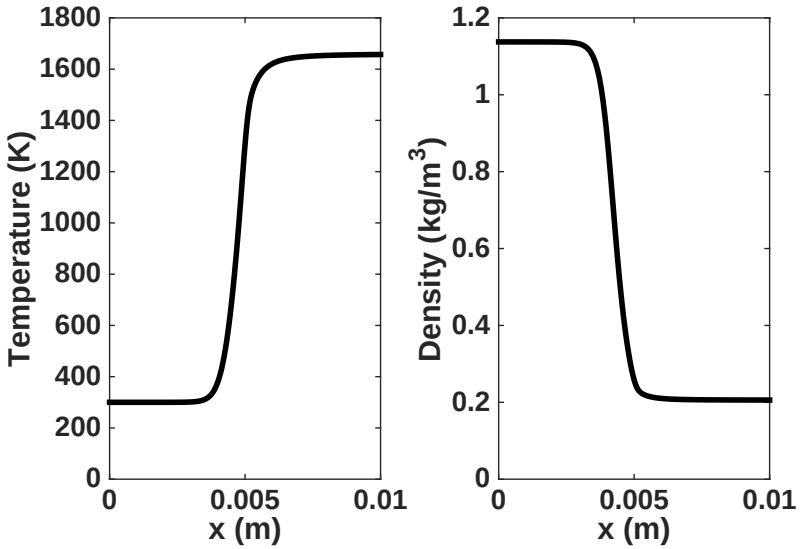

Figure 4.4: Unfiltered one dimensional flamelet solution for CH_4 fuel at $\phi = 0.6$.

was increased from ϕ_s to ϕ_f (as indicated by table 4.1) over a time span of 100 ms.

4.3 Results

The primary motivation in this study is the flashback speed. This quantity is strongly dependent on two factors: the turbulent flow field and the flame speed. The former requires adequately resolving the flow on the mesh or appropriately choosing a sub-grid turbulence model, especially in the near wall region where boundary layer driven flashback is expected. The previously examined channel flashback corroborates this, demonstrating a minimum grid requirement for flashback to occur. The latter factor demands a combustion

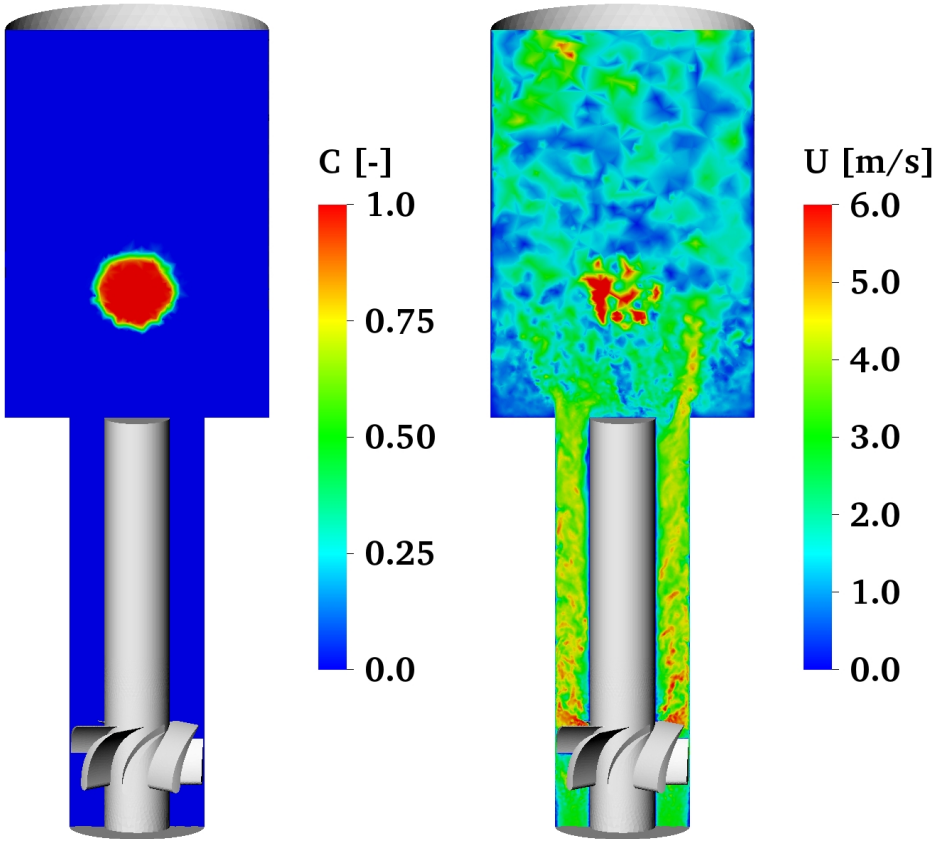

Figure 4.5: Instantaneous contours of reaction progress variable C (left) and density corrected velocity field (right) immediately after initialization

model which can accurately capture flame propagation and the effects of wrinkling and turbulence. In order to isolate the effects of the model, the flow field is first examined in the absence of combustion and compared against the corresponding experimental data [22]. Qualitative and quantitative examinations of the stable reacting case and mixing tube flashback follow.

	Case 1	Case 2
Fuel	CH_4	H_2/CH_4 (95% H_2 by volume)
Bulk inflow velocity (m/s)	2.5	2.5
p (atm)	1	1
Re	4400	4400
ϕ_s	0.6	0.33
ϕ_f	0.8	0.4
S_L (cm/s)	26.0	26.0

Table 4.1: Summary of cases simulated

4.3.1 Inert flow characteristics

Figure 4.6 displays instantaneous contours of the streamwise, azimuthal, and radial components of the velocity field. The vanes introduce a strong swirl into the flow, indicated by an azimuthal component on the same order as the axial. Equation 4.1 was used to calculate the global swirl number for the flow.

$$S = \frac{\int_0^{R_o} \rho U_\theta U_z r^2 dr}{R_o \int_0^{R_o} \rho U_z^2 r dr} \tag{4.1}$$

where R_o is the outer radius of the annulus, U_θ is the azimuthal velocity component, and U_z is the axial velocity component. A value of $S = 0.9$ was obtained, which agrees with both analytical and experimental expectations. Because the Reynolds number of 4400 (based on annular gap height and centerline velocity) is not large, turbulent mixing is relatively weak. Consequently, some larger scale structures remain non-homogenized throughout the mixing tube and breakdown only upon expansion into the combustion chamber. This

breakdown yields the recirculation zone paramount to flame stabilization.

Figure 4.7 shows the streamwise and rotational components of the velocity field, averaged in the azimuthal direction and in space. Near the combustion chamber, both components of the LES compare favorably with the experimental results. As expected, U_θ peaks closer to the inner wall, while the axial velocity peaks near the outer wall. Discrepancies between the datasets grow as slices further upstream are considered, though in all but the last they remain within a single standard deviation (as calculated from the experimental data set) of the correct value. At the 73 mm plane, the streamwise velocity is particularly ill-predicted. Despite some differences, there is overall agreement between the averaged fields.

One of the striking characteristics of the inert flow is the elongated high speed streaks in the mixing tube. To varying extents, these structures can be seen in all three components of the velocity, though the axial component shows the widest variation from the surrounding flow. The streaks can be traced upstream to the gaps between neighboring vanes, indicating a high degree of coherence throughout the tube, a consequence of low Reynolds number as mentioned above. Another flow feature, particularly clear in the azimuthal velocity component, is the presence of a precessing vortex core (PVC). Near the interface between the mixing tube and the combustion chamber is a region of high velocity and longer characteristic time scale which precesses about the bluff body. At the particular instant shown in those figures, this region is on the right hand side of the tube. PVCs are the consequence of vortex breakdown

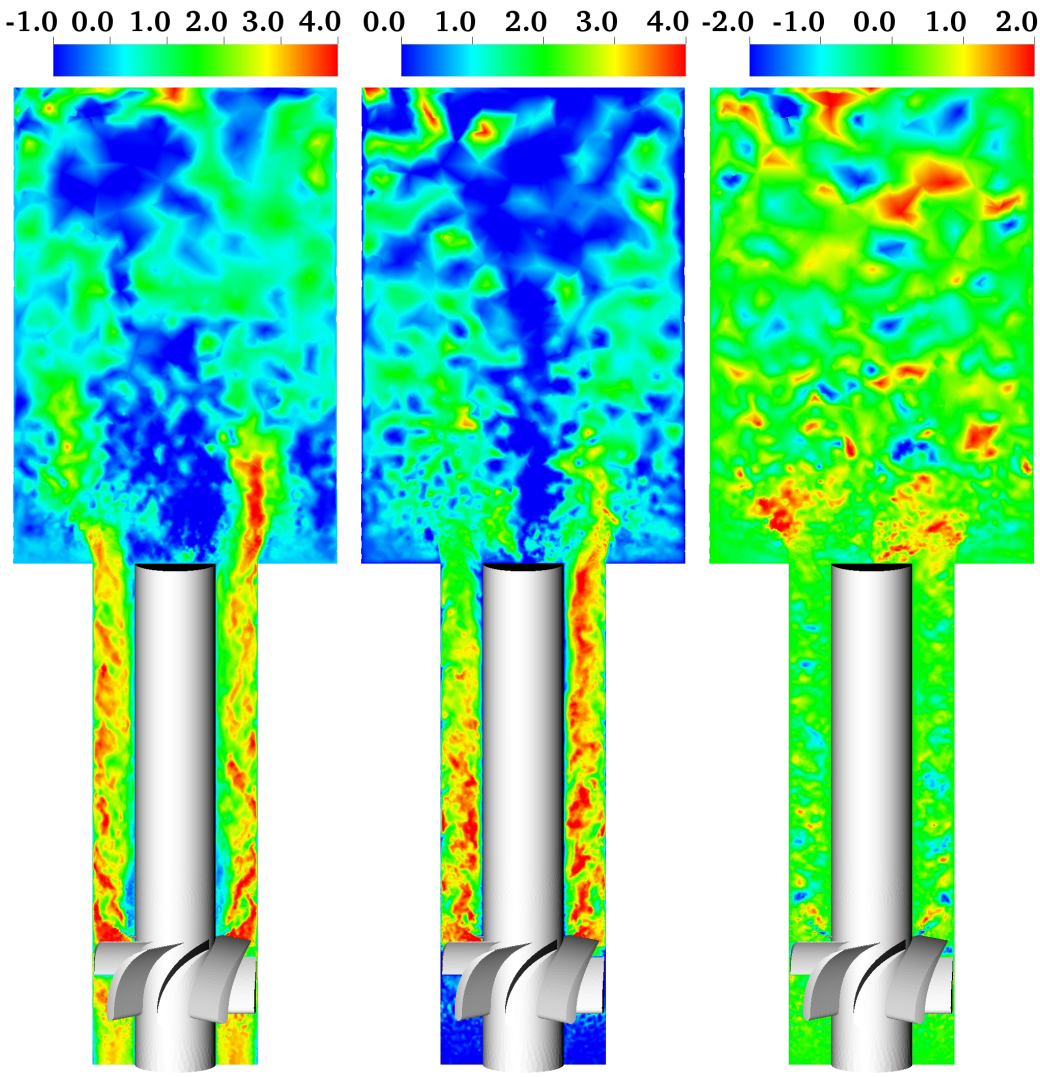

Figure 4.6: Instantaneous streamwise (left), azimuthal (center), and radial (right) velocity components for a bulk inlet speed of 2.5 m/s.

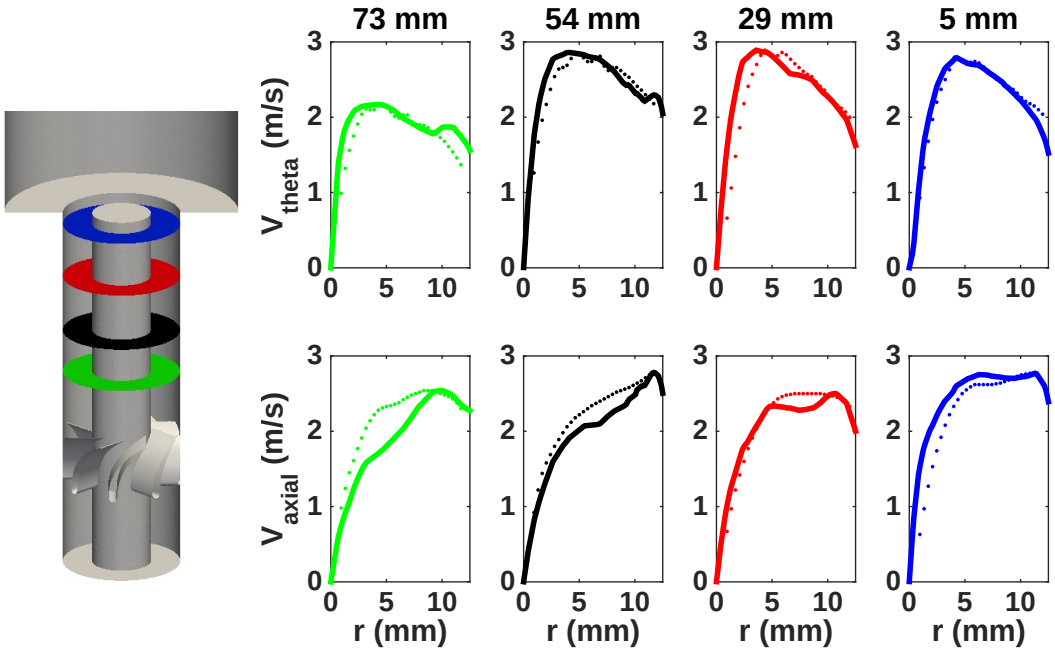

Figure 4.7: Time averaged streamwise and azimuthal velocity fields at four positions inside the mixing tube for LES (solid) and experiments (dotted) given a bulk velocity of 2.5 m/s. Radial position is measured from the bluff body to the outer wall while streamwise position is measured from the plane between the mixing tube and combustion chamber.

in the chamber which yields an upstream effect. This low-frequency large scale motion ultimately affects the azimuthal location of the flame flashback, as the front must go around it. The streaks and precessing core are expected to become primary governing factors in the development of the flame front and the manner of flashback seen.

4.3.2 Reacting flow and flame analysis

As described above, the flame was initialized far downstream within the combustion chamber and allowed to propagate to the mixing tube, with the equivalence ratio set sufficiently low as to avoid triggering flashback. Though outside the scope and primary objectives of the study, the stabilization of the flame serves as a validation that the turbulent flame speed is not excessive, given the sensitivity of the flashback to this quantity. For illustrative purposes, a volumetric rendering of the stable flame can be seen in Figure 4.8. The flame maintains a funnel shape, with the apex close to the tip of the bluff body. Note the extremely low peak temperature of the stable flame, due to an equivalence ratio of 0.3 in the H_2/CH_4 case, only marginally higher than the lower flammability limit (LFL) for the given fuel mixture.

To gain a general idea of the flame behavior as it flashes back through the mixing tube, a characteristic case is shown in Figure 4.9. In this series of instantaneous images, a methane flame starts within the combustion chamber. As a richer mixture is flowed in, the flame surface gradually enters the tube, moving along the bluff body exclusively and in opposition to the outer wall. This flame motion continues, with the front developing a definitive foremost point, henceforth called the leading edge. The flame propagates not only upstream, but also in the azimuthal direction promoted by the flow swirl. Similar to the channel flow, where a higher centerline velocity yielded a v-shaped front, here the higher axial velocities found near the outer wall impose an inner wall flame, mostly prohibiting it from extending far beyond the boundary layer.

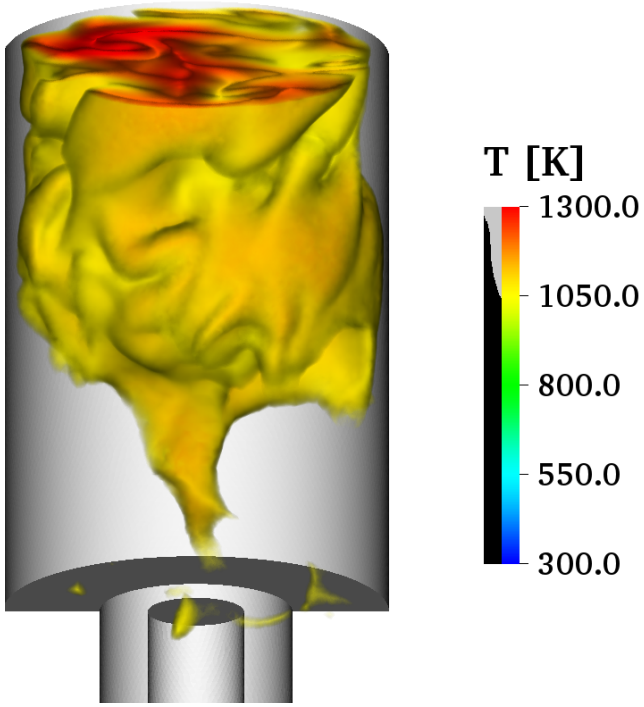

Figure 4.8: Instantaneous volume rendering of stable H_2/CH_4-air flame.

Also analogous to the channel problem, the front is characterized by a series of curved bulges, inflecting toward the wall and downstream flow. Smaller scale structures and wrinkles form and dissipate throughout the simulation. While the experiments were run until the flame front extinguished itself in the vicinity of the vanes, LES computations were terminated after the leading edge traveled roughly 70 mm into the mixing tube (corresponding to the green plane in Figure 4.7). This avoids those upstream regions of the tube with questionable velocity statistics while allowing the flame to move beyond the influence of the precessing vortex core.

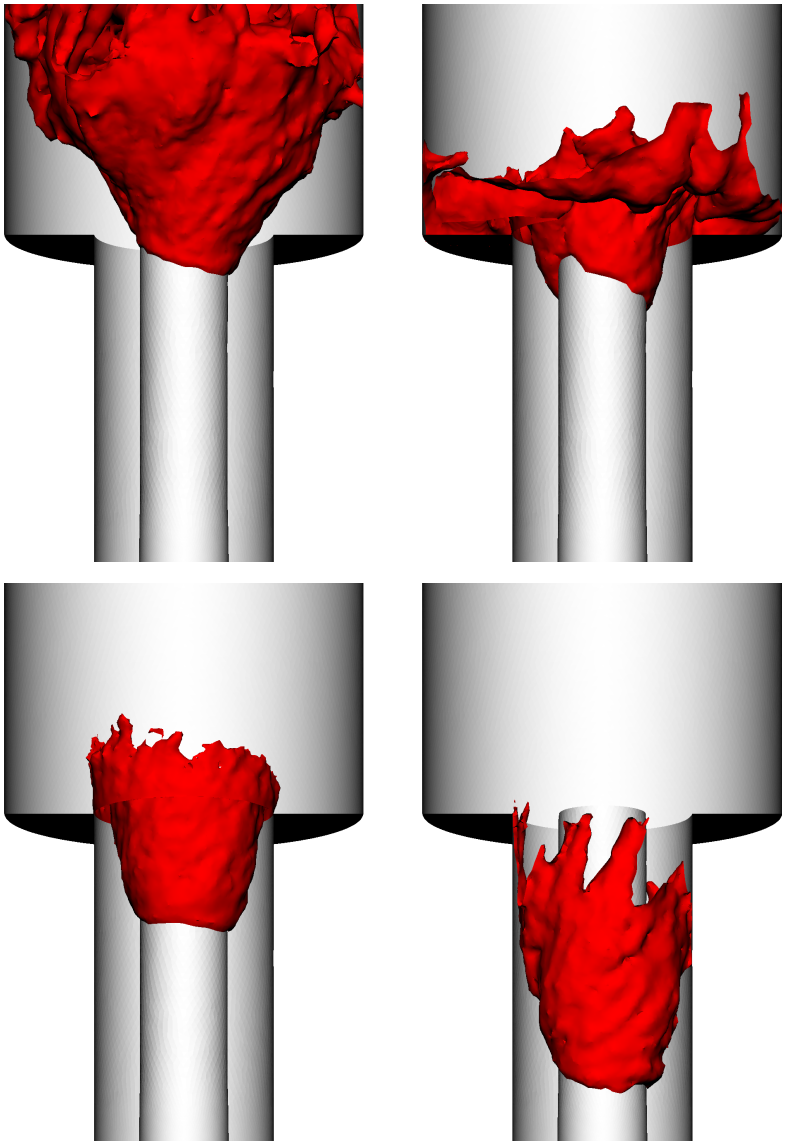

Figure 4.9: Instantaneous isocontours of T = 1400 K at t = 0.105 s (top left), t = 0.115 s (top right), t = 0.135 s (bottom left), and t = 0.165 s (bottom right).

The cases studied here explicitly triggered flashback, but a working combustor does see stratified flows and a potential for large periodic spikes in equivalence ratio. The sensitivity of the flame to these local increases is therefore of some consequence. While the equivalence ratio is uniformly increased at the inlet plane, the high speed streaks carry it unevenly toward the chamber. The flame initially encounters this richer mixture near the outer radius of the mixing tube and advances, but only when the richer mixture diffuses or is convected into the boundary layer does the front flash, advancing in a manner very similar to the channel flashback. As the front is already fully corrugated by the time it reaches the tube, however, the initial wrinkling phase does not occur. The familiar system of bulges and cusp wraps around the bluff body, stretched by the swirling flow. In a manner analogous to the channel, the swirling flame eventually reaches a quasi-steady flame depth after which further stretching of the front ceases. This state can be seen in the last image of Figure 4.9. As expected, there is a large asymmetry between inner and outer walls.

While the macroscopic structure of the flame shows many of the same features of the channel flashback in the context of a swirling bulk flow, there are several differences. Considering the front shape itself, a series of ligaments can be seen extending away from the wall. These structures are referred to in this work as flame tongues. For comparison, both the single-tongue front and the finer scale multi-tongue front are shown side by side in Figure 4.10. Despite reaching lengths on the order of the channel itself, these structures are

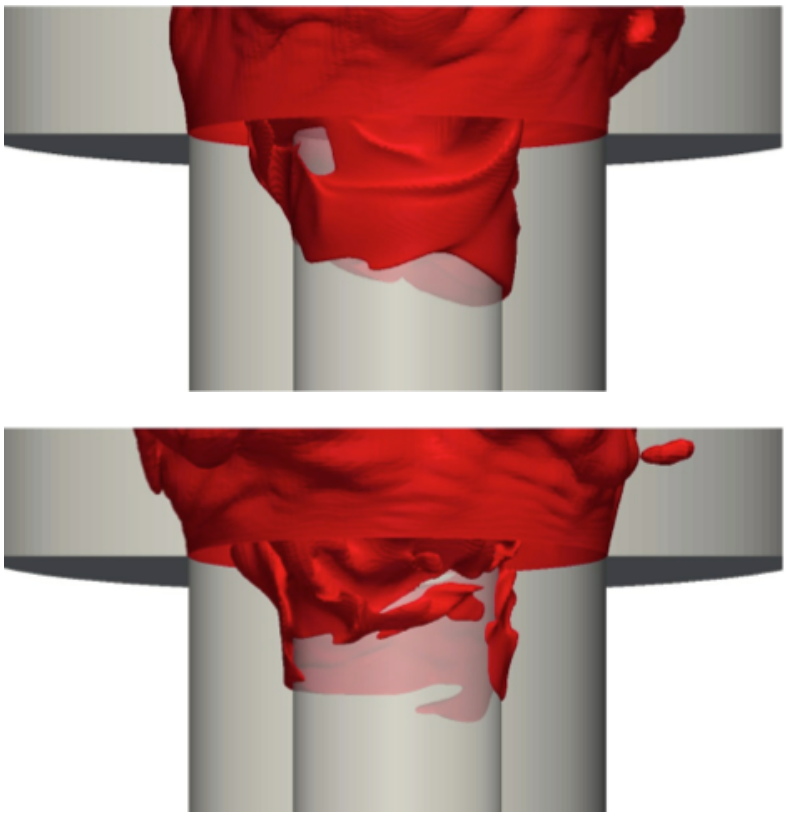

Figure 4.10: Instantaneous isocontours of T = 1400 K, indicating single flame tongue (top) and multi-flame tongue (bottom) behavior.

characterized by short time scales, developing out of the front and rejoining it quickly. Their root cause could be any combination of locally high equivalence ratio or low velocity, but given their transience, the overall effect on the flashback speed in minimal.

In contrast to the channel flame, which extends between both walls, the swirler flame flashes back only along the bluff body. To determine the reason

for this, an examination of the velocity field and in particular the behavior of the flow as it encounters the flame is necessary. As already discussed, the swirl introduced by the vanes and the presence of the bluff body create an uneven velocity field, slower near the inner wall and faster at the outer wall. The weak mixing exacerbates this difference, with high speed streaks lasting throughout the annulus and some core breakdown near the combustion chamber. In general, as the front moves through this field there are two consequences, both of which can be seen in Figure 4.11. First, as flow passes through the flame, its density decreases drastically and it accelerates according to continuity. This difference between burnt and unburnt sides creates a stretching effect and the flame thickens. Second, the unburnt flow is to some extent redirected around the flame. In the axial direction, the cross-section is effectively reduced and consequently the flow accelerates through the converging unburnt mixture, a behavior seen in the channel. Regions near the outer wall, already possessing higher speeds, get faster and the boundary layer narrows. The flame, needing the boundary layer to sustain flashback, is quenched within the narrow band and thus cannot exist at the outer wall.

4.3.3 Effect of fuel variation on flame behavior and flashback speed

As stated previously, the two cases were chosen to yield the same laminar flame speed at the flashback equivalence ratio. All else equal, a large difference in flashback speed was not expected. The results summarized in Table 4.2 indicate, however, that the flashback speed varies drastically depending

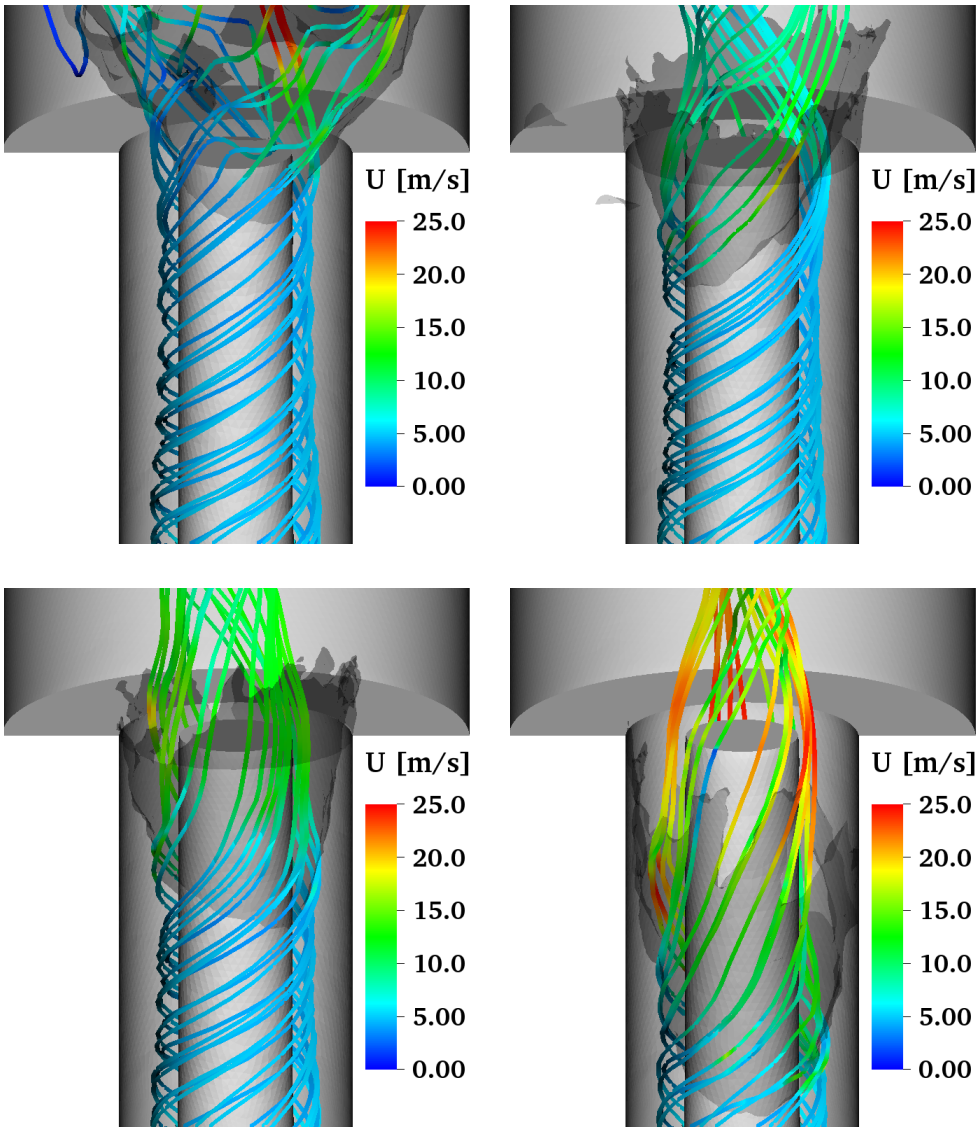

Figure 4.11: Instantaneous streamlines seeded uniformly about the bluff body and colored by velocity magnitude. The transparent gray front represents the T = 1400 K isocontour. Images are taken at t = 0.105 s (top left), t = 0.125 s (top right), t = 0.145 s (bottom left), and t = 0.165 s (bottom right).

	CH_4 - Flashback speed (m/s)	H_2/CH_4 - Flashback speed (m/s)
Experiment	0.58	0.94
LES	0.55	0.71

Table 4.2: Experimental and LES flashback speeds for both fuel compositions

on the fuel. This speed is calculating strictly in the axial direction, determined by the distance the leading point travels over some time frame. Experiments indicate that this is a consequence of thermo-diffusive effects and positively stretched flame tips. That the hydrogen flame can approach closer to the wall before being quenched could also contribute to the higher global front propagation speed. Additionally, the pure methane flame speed is extremely well captured while the hydrogen/methane mixture flame speed is under predicted. The reasoning behind this is not immediately apparent, but upon closer inspection, many of the ideas gathered from the channel can be directly applied to explain why this discrepancy occurs.

Figure 4.12 shows the flame isosurface for both fuels at comparable locations. While the difference is subtle, the pure methane case is characterized by a smoother surface, while the hydrogen/methane mixture is convoluted, showing many of the same macroscopic shapes while containing small-scale corrugations overlaid. From the channel LES, it was determined that correctly resolving these small scale structures can have implications on the growth of the flame. Thermo-diffusive instability stemming from a non-unity Lewis number for the hydrogen [42] yields a more wrinkled flame under the same Reynolds

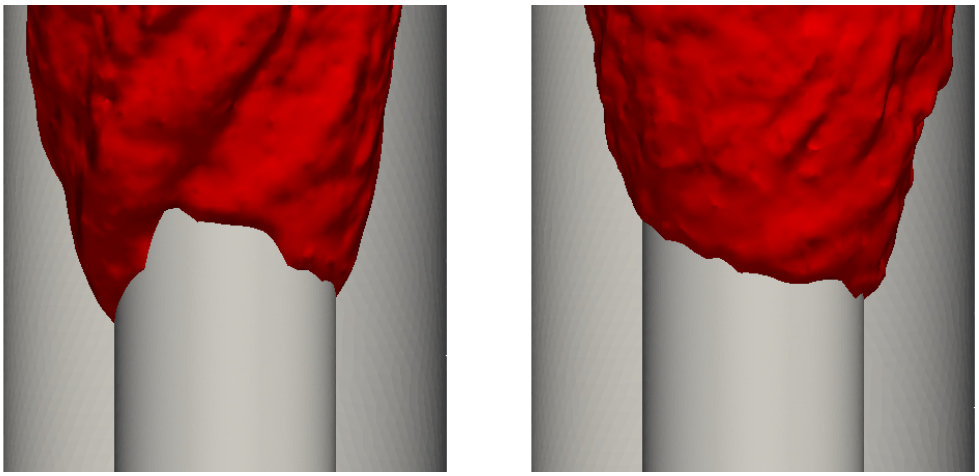

Figure 4.12: Instantaneous C = 0.7 isocontour for methane (left) and hydrogen/methane (right).

number. This phenomenon was accounted for in determining appropriate grid resolution and throughout the iterative refinement of the mesh.

4.4 Conclusion

In this chapter, the premixed flamelet combustion approach was used in LES of a swirling burner for both inert and reacting conditions. Similar to the channel problem, the behavior of interest was the upstream propagation of premixed methane/hydrogen flames through the low speed boundary layer. Regarding the inert validation, the simulations proved very accurate: the mean and standard deviations of velocity within the mixing tube matched well with experimental results, despite some sensitivity to inflow boundary conditions. Furthermore, macroscopic flow features such as high speed streaks, vortex

breakdown, and the precessing vortex core were also well represented.

The simulations also accurately captured much of the flame behavior qualitatively, including the ligament like structures and contraction-like effects due to the flame which caused an acceleration of the unburnt flow as it moved past the front. The result is an accurate prediction of the flashback speed. The LES computations also exhibited the correct behavior for the transition from a stable flame to flashback, a requisite characteristic of any model used in these types of applications. Further work will refine the models on the basis of the conclusions drawn from this work as well as examine the same configuration in the context of more real world conditions, specifically setting the combustor to a higher pressure. Such a change, while easy as far as computational implementation, will require a more complex experimental set-up to obtain validation data.

Chapter 5

Ultra Compact Combustor Simulations

Having tested the Eulerian flow solver in the two previous chapters, the Lagrangian particle tracking component is validated in the context of an experimental gas turbine combustor. Building upon the prior swirler, this case uses an unstructured mesh with complex flow physics and droplet based JP-8 fuel. Unlike the transient flame behavior studied there, however, only time-averaged values are examined. Comparisons are made against experimental data collected at the Air Force Research Laboratory.

5.1 Background

The placement of inter-turbine burners (ITB) between the high and low pressure stages of a gas turbine is known to provide high thermal efficiency [76]. Since the ITB exhaust flows over the turbine blades, incomplete combustion products could detrimentally affect the lifecycle performance of turbine components through secondary reactions [52, 15, 14]. Figure 5.1 shows a schematic of a potential ITB concept as well as a conventional combustor path. To reduce the weight penalty which accompanies these additional burners, reducing the dimensions of the combustor becomes important. The size, or length in the

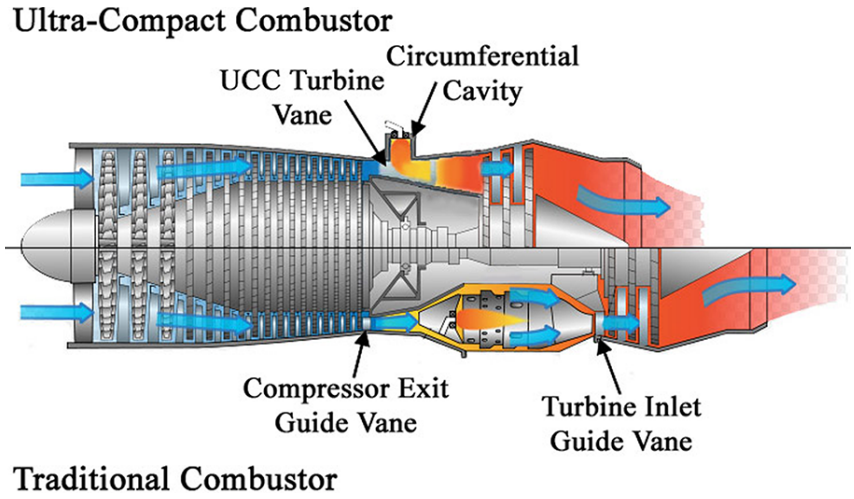

Figure 5.1: Schematic of an ultra-compact combustor (top) compared to a traditional combustor (bottom).

case of the schematic, of the conventional axial flow combustors is dictated by the residence time required to evaporate the fuel, ensure appropriate mixing, and complete reactions [43]. Reducing the size of the combustor beyond a critical length may lead to fuel rich products entering the turbine section and causing damage or potentially being exhausted, wasting fuel [5, 38, 50, 87]. Inter-turbine burners using conventional combustion technology for aerospace applications face similar size constraints.

One approach for reducing the length of combustors is to inject the fuel and a portion of the air in a cavity recessed from the flow. This moves the fuel injection region, which takes axial length in a conventional combustor, to a radial position. The fuel rich combustion products move radially from the cavity into the axially flowing core-flow, where reactions are completed. A particular implementation of this concept is the high-g combustor [6, 11,

90, 91, 92]. In the high-g combustor, the bulk fluid motion in the cavity is in the circumferential direction around the combustor axis [82]. This is achieved by angling the air injection holes within the cavity to impart the required tangential momentum. The high momentum and direction of the gases in the cavity result in centripetal forces which may interact with the fluids within the cavity.

It has been argued that at sufficient centripetal forces the reaction rates within the high-g combustor are enhanced [82]. This is based on combustor performance data from Zelina and the work of Lewis [92, 45, 46]. Lewis measured changes in the apparent turbulent flame speed as premixed fuel (either hydrogen or propane) and air were ignited and subjected to centripetal forces in a rotating tube. An increase in flame speed greater than a factor of three was observed for propane flames as the centripetal force was increased from less than one to over a thousand times the force of gravity. Lewis theorized that the increase in turbulent flame speed resulted from buoyancy forces [45]. These forces cause the less dense hot combustion products to be propagated into the more dense premixed fuel and air [45]. Further validating this research, Zelina calculated the flame speed of a laminar hydrogen-air flame with varying gravitational forces [92]. It was observed that the flame speed increases by factors of 2 and 4 for forces of 10^2 and 10^3 times the force of gravity, respectively. It is important to note that these studies were in environments where there was no cross-flow and gaseous fuels were burned. This is significant because in practical aerospace applications liquid fuels are typically burned and the

centripetal forces are created by the bulk air flowing within the cavity (i.e., flow is orthogonal to the direction of the centripetal force).

Hence it is not clear whether the interaction in the flame speed and centripetal forces are applicable for cavity stabilized combustor environments. Moreover, it is not clear if stratification between the liquid fuels and gases will occur in a high-g combustor because of centripetal forces. This has the potential to have a significant effect on combustor stability and performance. To better understand the flow dynamics inside a high-g combustor, an LES based study of a model combustor is conducted. Focus is placed on the flow and droplet fields, ignition and flame stabilization, and effects of varying g-loading on temperature statistics. Experimental datasets are used for validation.

5.2 Case details

5.2.1 Experimental configuration

Figures 5.2 and 5.3 show the AFRL high-g combustor design. Figure 5.4 shows a schematic of the reactor and the various air feed and fuel droplet injection ports. This experimental combustor consists of three sections: the toroidal cavity, the spray and air manifold, and the exhaust section. The volume of the toroid without the air and fuel manifold (i.e. the cavities) was approximately 250 mL. The outer diameter was 13 cm. JP-8 fuel was injected through three pressure atomizers spaced symmetrically around the outer radius of the toroid. The faces of the nozzles were flush with the outer radius of the cavity. Air entered the cavity through a series of 48 holes at the outer radius

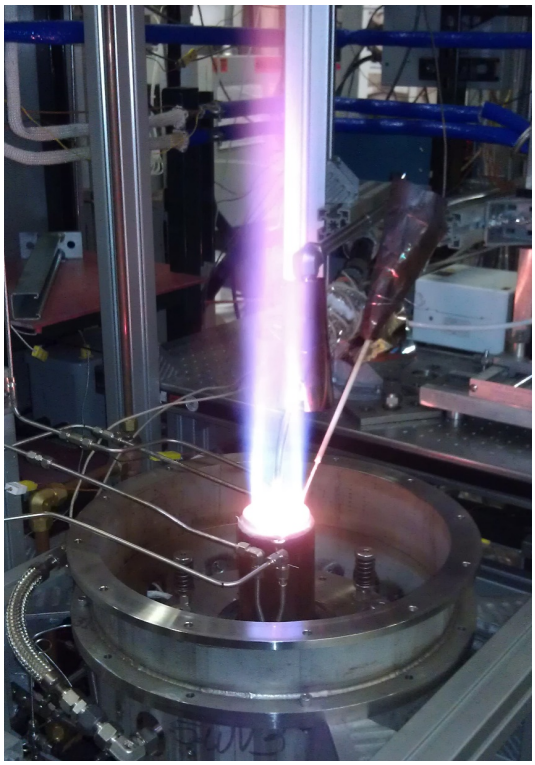

Figure 5.2: Operational high-g combustor showing the exit flow.

of the toroid, spaced symmetrically with respect to the fuel nozzles. The holes were drilled at 45° relative to the normal to impart momentum in the tangential direction. The diameter of each hole was 0.8 cm. The air passing through the holes was plenum fed and metered using mass flow controllers. The metal reactor was water cooled and coated on the inside with thermal barrier coating to provide additional thermal protection in the combustion environment.

The combustion gases migrated and exited through a 0.05 m diameter hole at the center and top of the toroid. A ceramic flow straightener consisting

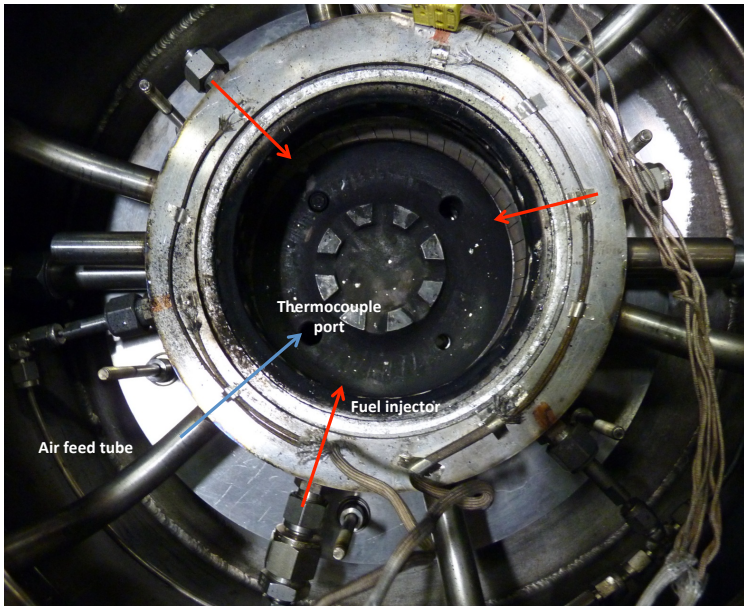

Figure 5.3: High-g combustor top view indicating the fuel injection and air feed ports.

of 6 straight fins was placed in the exit from the reactor to reduce the swirl and eliminate swirl-induced reverse flow. The combustion products pass through the straightener and then through a ceramic stack prior to exhausting.

Both velocity and temperature measurements were obtained from this combustor. For the velocity measurements a two component hot wire probe was traversed in the axial direction between the top and bottom walls of the toroid. The probe was oriented in the central plane of the toroid with one wire directed radially and the other directed tangentially. Calibration of the probe was done with respect to velocity magnitude and in-plane directionality using a flow stand with known velocity characteristics. Due to probe signal sensitivity at experimental design conditions, the resulting uncertainty

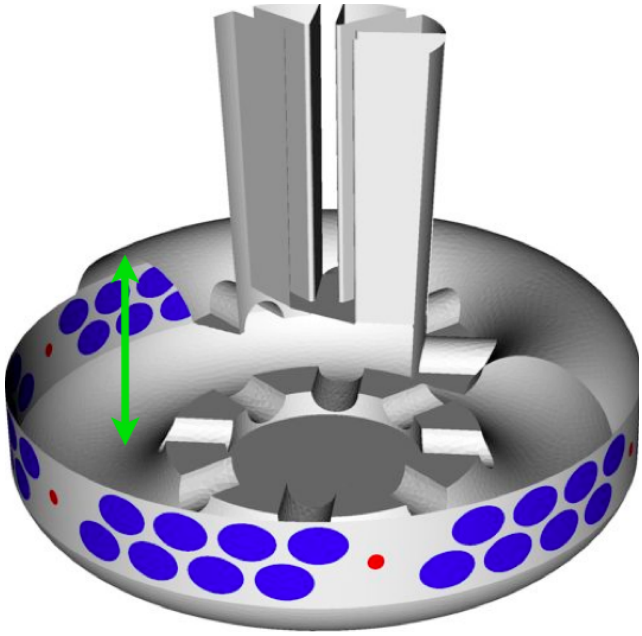

Figure 5.4: Schematic of the high-g gas turbine combustor, with air inlets (blue) and spray injectors (red) as indicated. Axial experimental measurements were taken along the green line.

of the velocity measurements was approximately 15% based on repeated measurements. Measurements were collected for cold flow conditions to ensure survivability of the probe and were compared to corresponding non-reacting LES calculations, accounting for out-of-plane contributions to the two-wire probe signal. Temperature measurements were collected by traversing a bare bead type-B thermocouple in radial and axial directions. The axial temperature profile was obtained between the top and bottom walls of the reactor (similar to the hot-wire probe). The radial profile was obtained from the center to the outer wall of the reactor. A sensitivity in the measurements to the relative position of the spray injector was observed. This is attributed

to the close proximity to the droplets, which can suppress the temperature. To account for this sensitivity, computed and measured temperature profiles are compared for the same orientation relative to the fuel injectors. The root mean square of repeated measurements of the axial and radial temperature profiles were typically within 15% of the mean value based on three or more repeated measurements.

The air flow rate through the reactor for inert and reacting conditions was 1000 SLPM (1.8 g/s). The calculated centripetal force for these flow rates peaked at 200 times the force of gravity. The air was preheated to 400 K for reacting conditions and was kept at ambient conditions for non-reacting measurements. The fuel (JP-8) flow rate was 129 mL/min, distributed between the three fuel injectors. This gave an overall equivalence ratio of approximately 1.3. Additional details of the inflow conditions are provided in Table 5.2.2.

5.2.2 Computational implementation

The simulation domain was directly obtained from the experimental design CAD files. However, the reverse flow issues seen in the experimental exhaust section are more easily dealt with numerically. As such, the section was truncated, leaving the reduced geometry shown in Figure 5.5. Given the complex nature of the flow and uncertainty associated with the flame stabilization, few assumptions could be made regarding appropriate grid sizing parameters. Some combustion length scales were obtained from FlameMaster, which were used to set an upper limit for cell size, and expected locations of

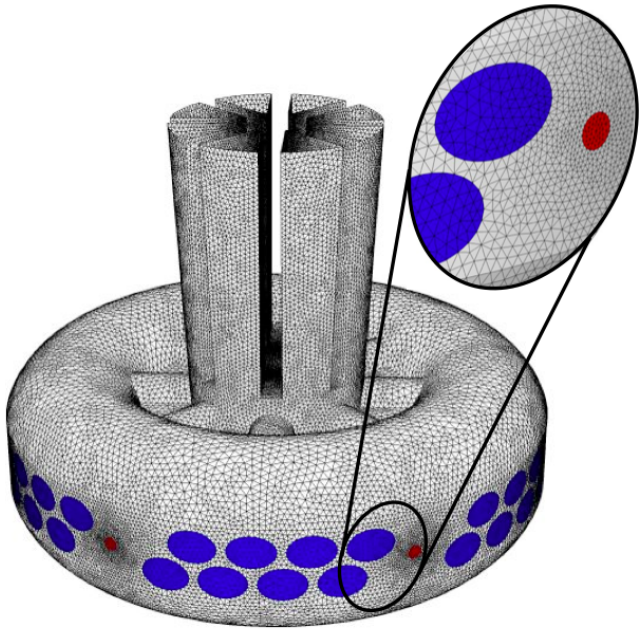

Figure 5.5: Mesh discretization of the outer domain surface. Enlarged region displays clustering near air and fuel inflow regions.

high strain rate in the immediate vicinity of air and fuel inflows required grid clustering [75]. The interior domain was otherwise uniformly meshed for a total of 5.5×10^6 computational cells.

As with the swirl burner, the LES equations were discretized using an Euler implicit scheme for time advancement. It was found that the use of higher-order time discretization did not improve accuracy or allow larger time steps. This was mainly due to the fact that the spray equations are solved explicitly, and the entire solution is constrained by the accuracy of this algorithm. Diffusion and convection terms again used flux limited second-order central difference schemes, while gradients are computed with second-

order least squares. Additionally, the spray equation were integrated using a 4th order Runge-Kutta method.

The fuel injection is based on a hollow cone nozzle model, and is specified to match the experimental spray injection angle (cone angle), droplet diameter distribution, and mass flow rate. To maintain computational efficiency while reducing cost, a parcel-based approach is used to model the spray population. Here, 75 to 100 parcels are added to the system at each time-step. The parcel sizes are obtained from a Rosin-Rammler distribution with a mean diameter of 85 μm. At steady state, the simulation domain consists of roughly 6×10^5 parcels. The boundary conditions for the flow and spray equations are provided in Table 5.2.2.

Parameter	Value
Fuel jet velocity	6.81 m/s
Droplet mass flowrate	1.77 g/s
Carrier flowrate	21.9 g/s
Bulk carrier air velocity	7.10 m/s
Jet Reynolds number	3,000

The flamelet table is obtained using a surrogate description of the JP-8 fuel, consisting of 62.6% n-dodecane, 19.8% methylcyclohexane and 17.6% m-xylene by mass [63, 9]. The flamelet equations were solved using the FlameMaster package [70]. Figure 5.6 shows the chemical source term used in the progress variable equation for zero mixture fraction variance. It is seen that the source is highly localized in the mixture-fraction/progress variable space. In other words, chemical reactions that lead to heat release could hap-

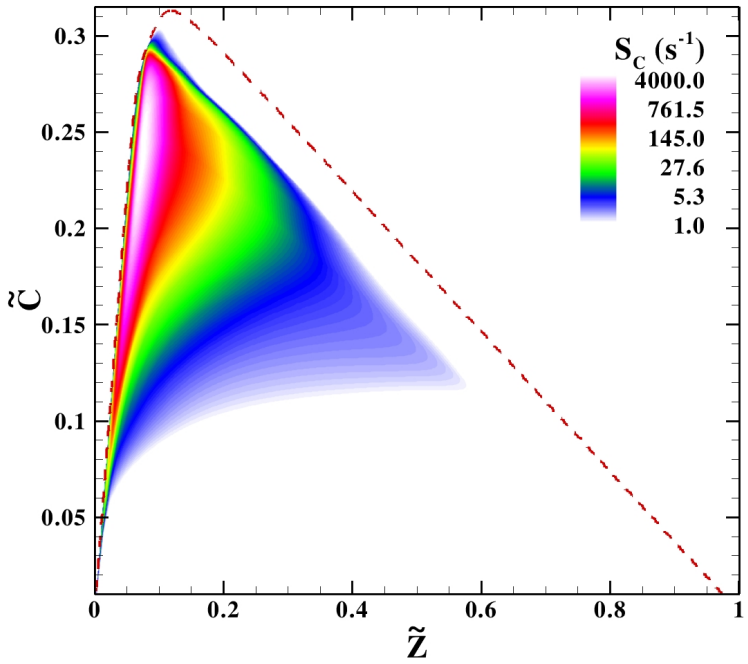

Figure 5.6: Progress variable source term obtained from the flamelet table, plotted as a function of progress variable and mixture fraction. The dotted line delineates the physically realizable and non-realizable regions.

pen only in a small fraction of composition space. Unless, these conditions are sustained in the combustor, global blowout/extinction will occur. This stringent burning condition is unique, in the sense that the fuel is created with safety in mind and requires some effort to induce ignition.

Unlike the approach taken with hydrogen fuels, which burn easily in the presence of an instantaneous spark, a sustained ignition zone was necessary to initiate a stable burning solution. This region was apart from the centerline axis, where high velocities wash out the flame. By holding areas within the toroid at a constant temperature for several residence times, determined based

on the circumference of the toroid and the injection velocity of the coflow air, the flame could take hold in the low speed flows. The ignition itself amounted to a source in the reaction progress variable, which was determined relative to the local fuel mixture fraction. After this, the high-temperature source region was removed and the solution was allowed to evolve until it reached steady state. The results and discussion below are based on this steady-state data.

5.3 Results

In this section, the LES results in the ultra compact combustor are discussed. Experimental validation is provided for both the inert velocity field as well as the reacting temperature field. After a discussion of these results and an analysis of droplet distribution and flame stabilization, new cases are created which examine the physics associated with incrementally increased inflow air velocities and resulting centripetal forces on the droplets.

5.3.1 Inert flow characteristics

Figure 5.7 displays instantaneous contours of each cylindrical component of the velocity field. Strong inward radial velocities accompany the prescribed tangential velocities near the air inlets, with regions of stagnant flow localized around the fuel injectors (both active and inactive). As the swirling flow moves toward the exhaust, mass conservation induces an amplification of the radially-directed component. It is in this region where the axial velocity, denoted as U_z, becomes significant. In the outer regions, however, the turbu-

lent mixing is relatively weak. With a Reynolds number based on the toroid internal diameter of 3000, significant levels of turbulence are not expected aside from the contraction forced by the flow straightener near the exhaust.

In comparing the two components of the time-averaged velocity field, centerline magnitudes agree well, as seen in Figure 5.8. The decay seen only in the lower half of the experimental result, however, differs from the LES by some 20%, which can be explained by the experimental technique used. In collecting hot wire measurements, a port was created for insertion of the instrumentation on the lower surface of the toroid. The port diameter was twice that of the hotwire probe, inducing cavity flow effects and lowering overall magnitudes immediately above the surface.

Examination of the streamlines indicates an asymmetry in the strength of the recirculation zones that is not apparent from the velocity field alone. By seeding the flow in three different axial locations, as shown in Figure 5.9, the impact of exhausting only in one direction can be exposed. The bottom plot shows the results of initializing streamlines circumferentially in the lower third of the toroid, where streamlines frequently cross the centerline and begin circulating again in the upper half before exiting through the flow straightener. By progressively moving the initial points upward axially, the paths become much more deterministic as the exhausting gas prevents downward mixing. Interestingly, points seeded near the spray injector plane (Figure 5.9, center) enter almost immediately into the core, suggesting a minimal residence time for droplets with those trajectories. In other words, a portion of the droplets

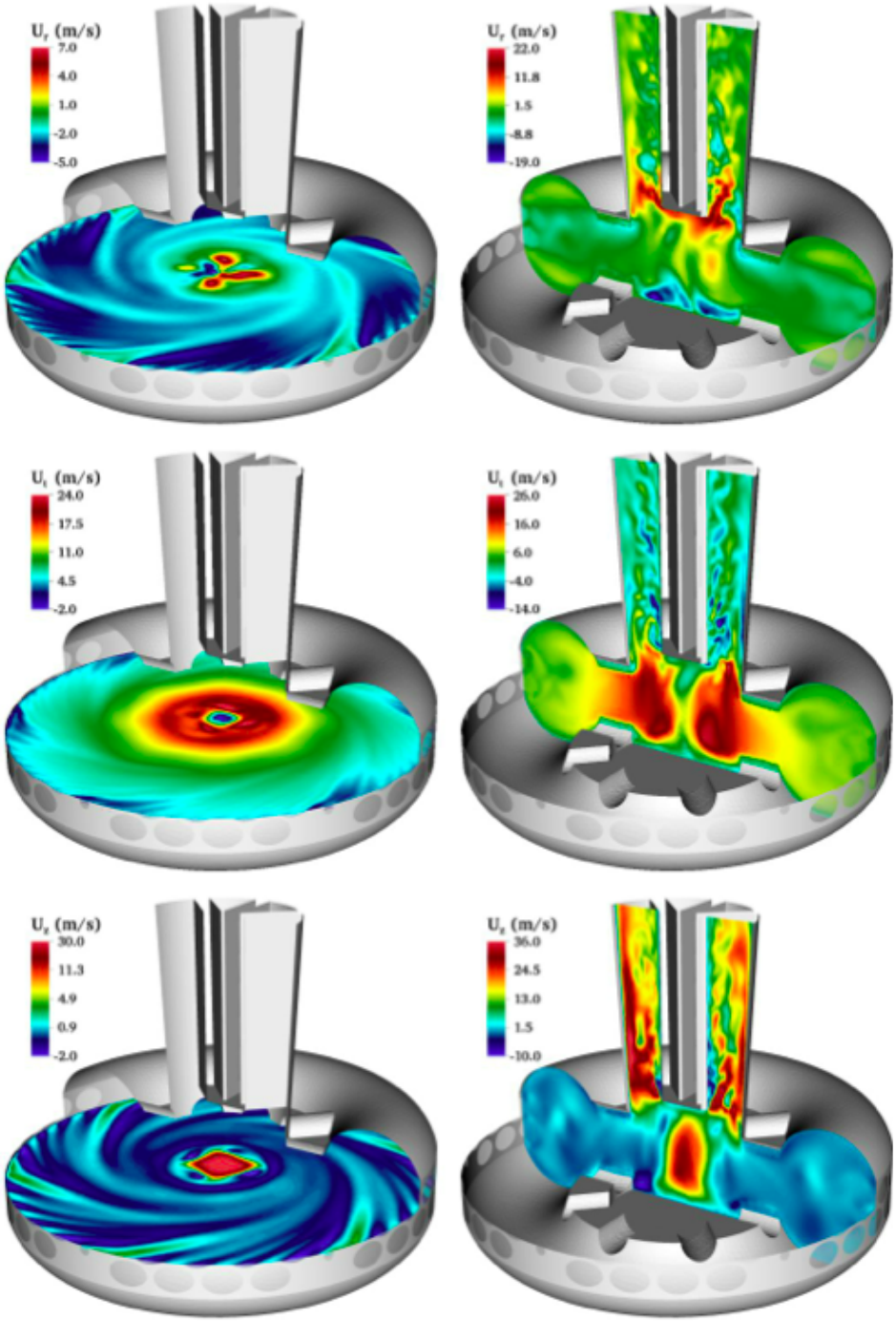

Figure 5.7: Instantaneous contours of radial (top), tangential (middle), and axial (bottom) velocity components

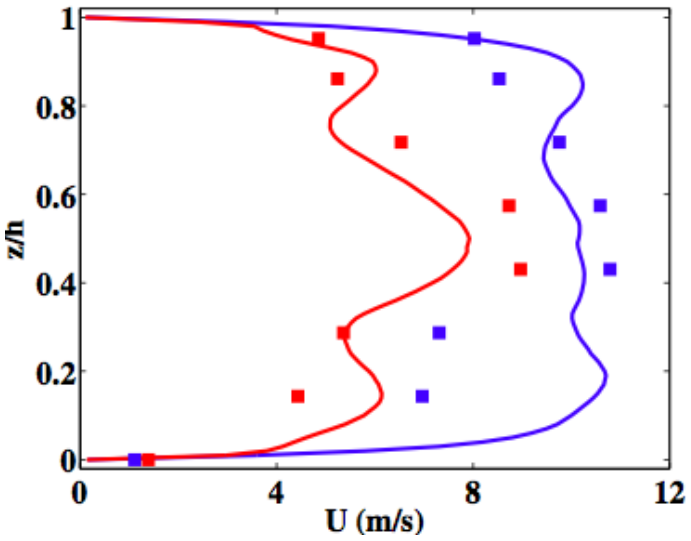

Figure 5.8: Comparison of time-averaged LES (lines) and experimental results (symbols) for radial (red) and tangential (blue) velocity components.

are at risk of being swept out of the domain before they can evaporate, mix, and combust. As will be seen from the reacting case, this proves important in the reaction and in particular the stabilization process.

5.3.2 Non-reacting Lagrangian spray

Figure 5.10 shows an axial view of the droplets. The plane crosses through the centroid of all fuel injectors and will henceforth be referred to as the spray plane. As the figure indicates, for this particular orientation, the primary flow is counter-clockwise. Unlike the air inlets, the fuel injectors are normal to the surface. The spray droplets then interact with the crossflow of air and are carried away from the injection point. It can be seen that the cone angle is wide enough that the three injectors distribute droplets fully

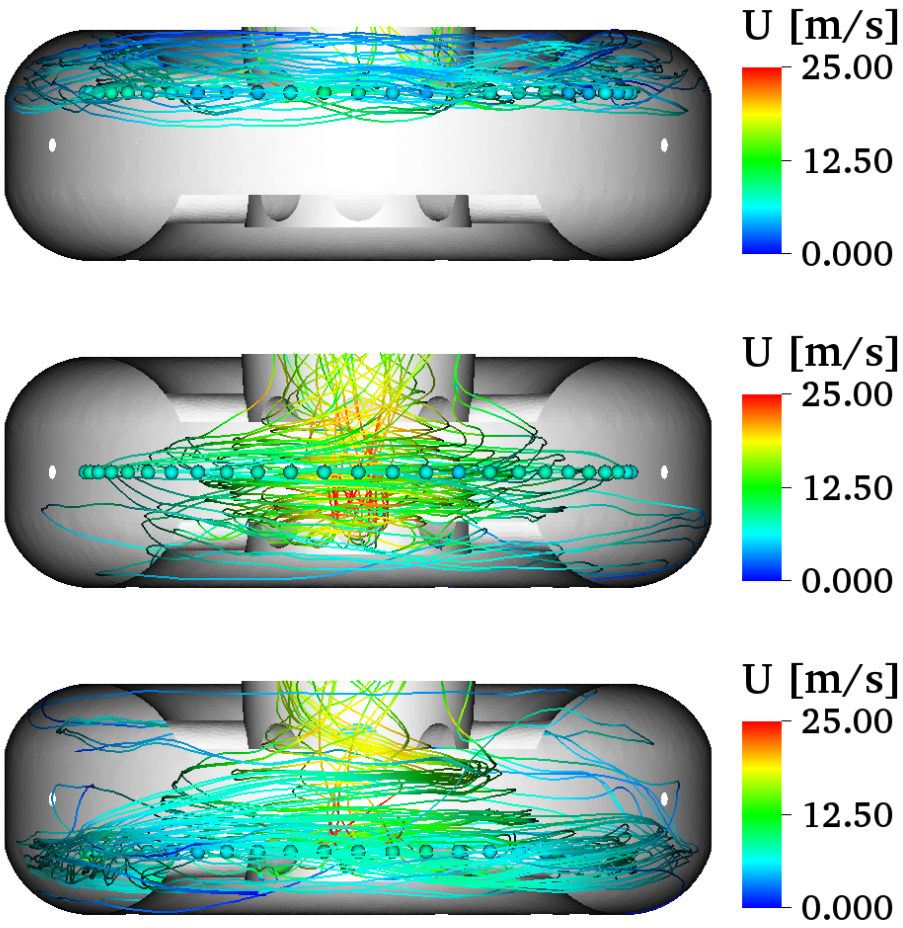

Figure 5.9: Streamlines colored by gas phase velocity magnitude, seeded within the upper (top), centerline (center), and lower (bottom) portions of the toroid. Note, the swirler is oriented with the exhaust pointing upwards.

around the circumference of the toroid. However, the presence of the cross-flow creates an asymmetry in the azimuthal distribution and the droplets flow downstream of the injection point. This also causes a depletion of droplets through evaporation. The droplet size distribution shows a similar asymmetry, where heavier droplets are present upstream of the injection point, while smaller droplets are seen near the higher temperature region on the lee side of the injector. At steady state, there are roughly 600,000 droplets in the domain at any given time. In this non-reacting case, nearly half of the injected fuel mass leaves the domain unevaporated.

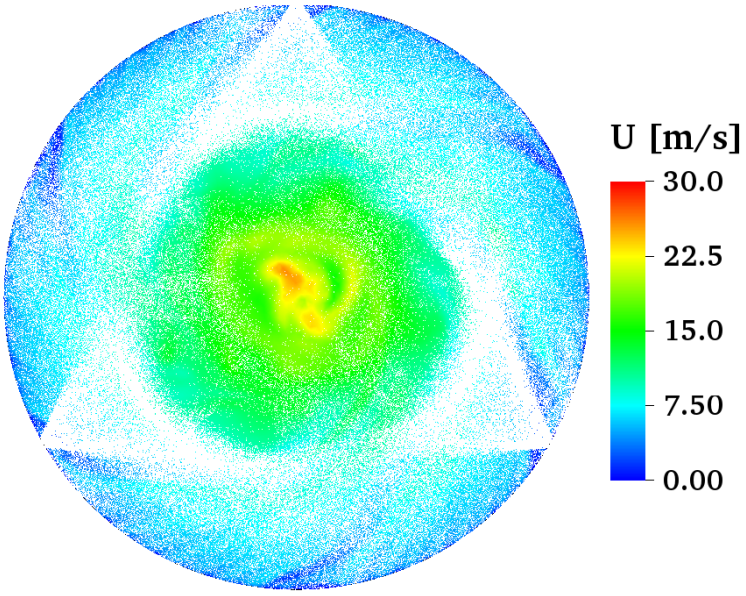

Figure 5.10: Droplet location superimposed over the gas phase velocity.

Figure 5.11 shows the magnitude of the velocity of the droplets in both the spray plane and the plane orthogonal to it. The cone shape of the injector is apparent, with droplets only sparsely populating the regions closest to the

walls. This is expected due to a strong air inflow. The mean entrance velocity of 22.0 m/s was calculated using an experimentally obtained pressure differential. A stochastic variation was superimposed over this mean. The particles are gradually brought to the gas phase velocity through the drag force, which scales non-linearly with Reynolds number. Low velocity droplets are seen on both the lee and windward sides. On the lee side, the low velocity is mainly due to the fact that the gas phase velocities are also low as the flow is diverted around the injection cone. This is similar to a jet in crossflow configuration, where the main jet acts as an obstruction which sets up a recirculation zone on the lee side [62]. The increased residence time due to the low droplet and gas phase velocities allow fuel mixing and ignition. The bottom image of Figure 5.11 shows the spread of the droplets out of the spray plane and into the top and bottom of the toroid.

One of the interests in this study was the effects of centrifugal forces on the droplets with varying Stokes numbers and the way this would impact flame stability and structure. Examining the evaporating droplets in the absence of the high temperatures associated with combustion provides further information about this distribution. As seen in Figure 5.11, the droplets reach every portion of the domain, indicating an evaporation time larger than the overall mixing time. Figure 5.12 more clearly displays the stratification of droplets due to inertial effects at injection. While the droplets are uniformly distributed at injection, the larger droplets continue along their initial trajectories while smaller droplets immediately begin following the streamlines suggested by the

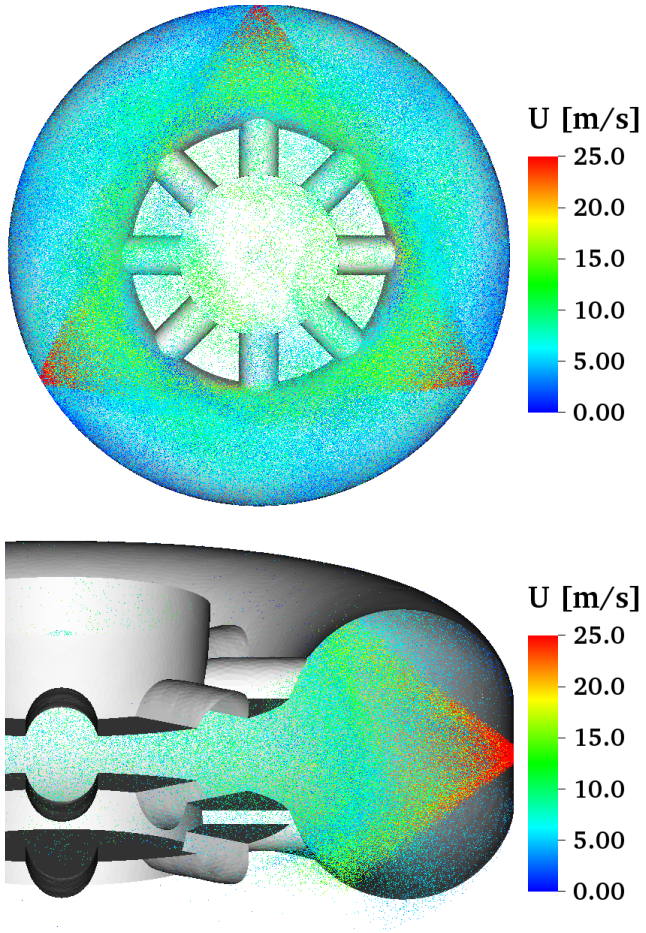

Figure 5.11: Droplet location colored by the particle velocity magnitude.

Eulerian velocity field.

5.3.3 Reacting flow and droplets

Consider a more detailed view of the reacting droplets. Figure 5.13 displays a single instance of the stochastic droplets colored by temperature and diameter. The data were collected during the transient stage prior to

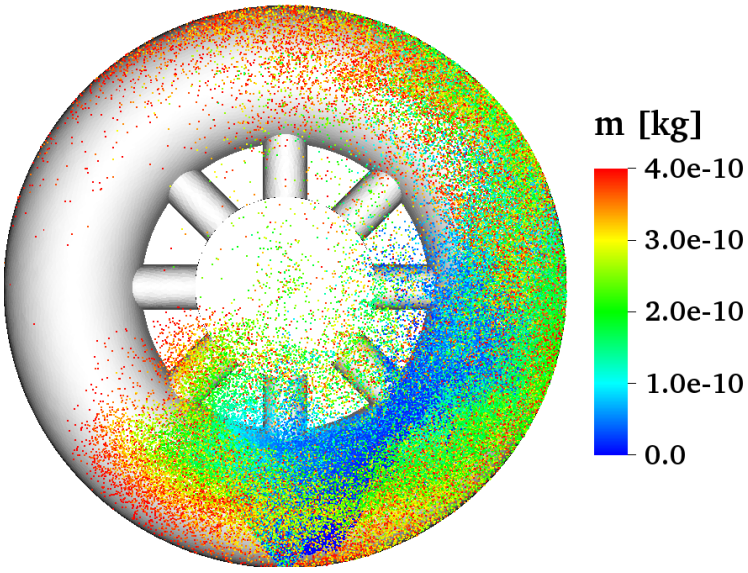

Figure 5.12: Instantaneous scatter of droplet location colored by particle mass for a single injector.

stable ignition and only includes droplets added by a single injector in order to provide a clearer description of droplet mixing and evaporation near injection. The continuous spread of the spray jet is evidence that large Stokes number droplets, or those with sufficient inertia to maintain their trajectory despite crossflow drag, are present in the flow. This strong inertial effect coupled to the relatively slow evaporation of large droplets results in a many droplets leaving the combustor before fully evaporating, even in the high temperature reaction. This is an important point of validation since one of the distinct characteristics of the experimental combustion was an accumulation of soot on the bottom side of the flow straightener. While the models implemented do not account for soot formation, it is encouraging to see that a fuel rich environment, favorable

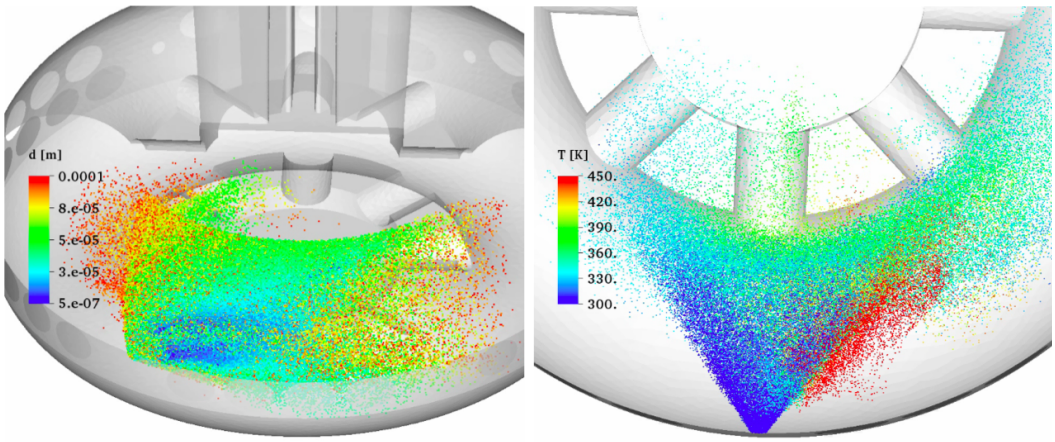

Figure 5.13: Instantaneous scatter of stochastic droplet diameter (left) and temperature (right) from an individual fuel injector.

for soot formation, can be replicated in the simulations.

Studying the droplet temperature evolution reveals that Stokes number greatly impacts the droplet heating and subsequent evaporation rates. Due to the d^2 dependence of the model, small droplets will inherently evaporate more quickly in the same environment. This in turn rapidly creates an even larger Stokes number discrepancy between large and small droplets. The result, as seen in Figure 5.13, is that small droplets are quickly carried downstream while and supply a large fraction of vaporized fuel despite their small masses individually. The evaporation source term reflects the description above, as displayed in Figure 5.14. The peak evaporation rates are directly downstream of the fuel injectors. This is a consequence of the freestream flow being slightly heated to 415 K, which is not only well above the injection temperature of the

droplets, but also nears the dodecane boiling temperature of 420 K. While measurable droplet evaporation is present throughout the domain, early flame formation is due to the fuel rich mixture resulting from peak evaporation rates as will be shown below.

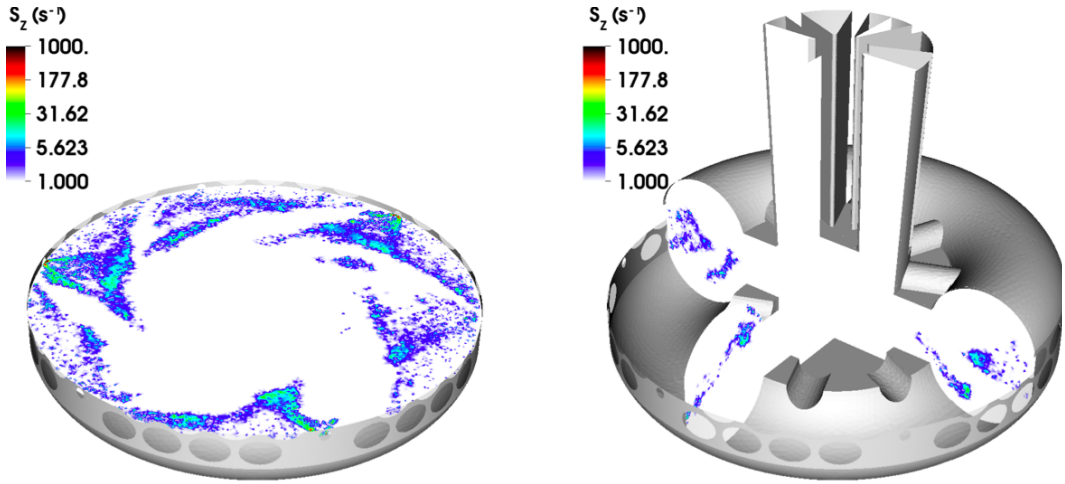

Figure 5.14: Contour of evaporation source term in axial (left) and radial (right) planes.

Figure 5.15 displays the vaporized fuel mass represented by the mixture fraction. The region of peak mixture fraction directly after injection is locally driven above the stoichiometric value by the droplets and subsequently diffuses to create a stoichiometric fuel mixture. Therefore, the structure resembles a diffusion-type flame, greatly simplifying the required modeling. When pockets of liquid fuel separate from the main injection zone, additional regions of very rich fuel content induce secondary flame kernels. In Figure 5.15, the instantaneous mixture fraction indicates entrainment into the upper and lower

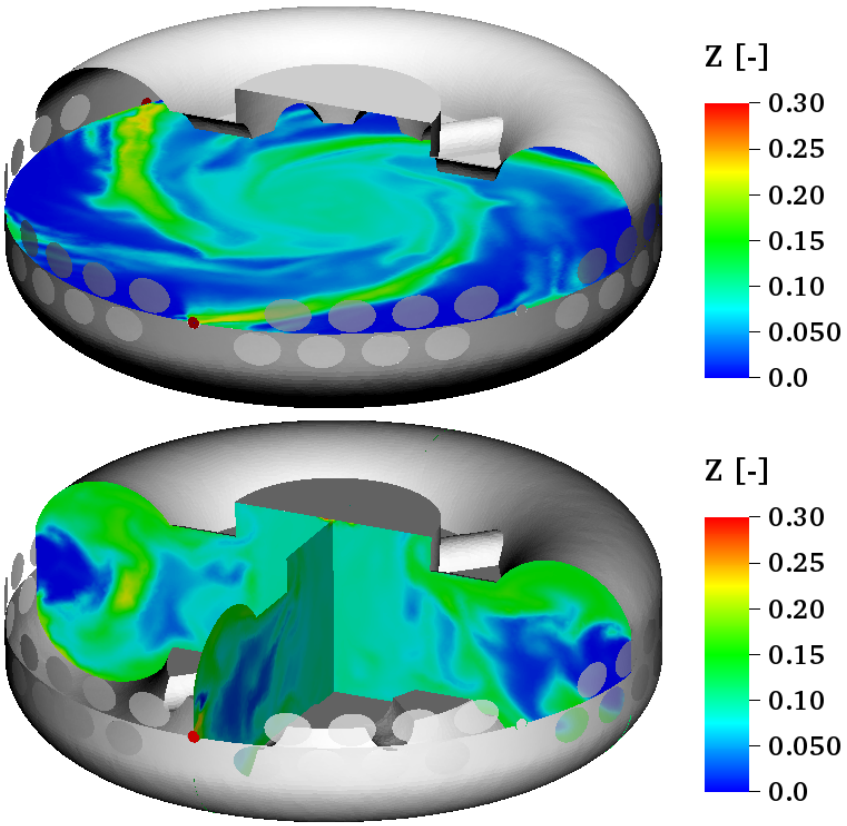

Figure 5.15: Instantaneous mixture fraction for burning solution, with fuel injector port colored in red.

regions of the outer toroid despite low levels of turbulence. This is crucial in achieving stable ignition of the reactive mixture. The lack of intense turbulence prevents the evaporated mass from each of the injectors from mixing on any small scale, as independent structures are seen even while nearing the exhaust.

From the model quantities, the gas phase temperature can be calculated. Figure 5.16 displays planar contours from the reacting simulation with temperatures ranging from 300 K where droplet evaporation demands signifi-

cant latent heat of vaporization to the peak flame temperature at atmospheric pressure of approximately 2100 K. The reactive system exhibits significant flame intermittency, but the source of this behavior differs from the more common turbulence-driven local extinction. The left hand contour in Figure 5.16 shows very little reaction occurring along the plane of droplet injection, whereas the right hand contour displays discontinuous but strong reactions located in the recirculation regions above and below the injection plane. This local phenomenon is evident throughout the toroidal combustor in Figure 5.17. Volume rendering of the temperature field clearly demonstrates the tendency of the highest temperatures to occur in the lower recirculation region for these simulations. While the upper region displays significantly higher temperatures than near the air and fuel injectors, the proximity to the exhaust allows the flow to immediately carry this mixture away from the vaporized fuel. In one sense the lower stagnation region serves as a pilot for the mixture and allows it to remain stably ignited.

With this intuition, Figure 5.18 shows validation of a one-dimensional temperature profile with experimental data taken both in the axial (top) and radial (bottom) directions. Note the axis is a dimensionless temperature, normalized against the peak value over the profile. With regards to the axial plot, both peaks are well predicted, though the experimental result fails to get close enough to the outside wall to capture the temperature drop. In the radial plot, while the core of the combustor is represented, an anomalous peak occurs in the LES. By examining the axis along which this data was taken, it becomes

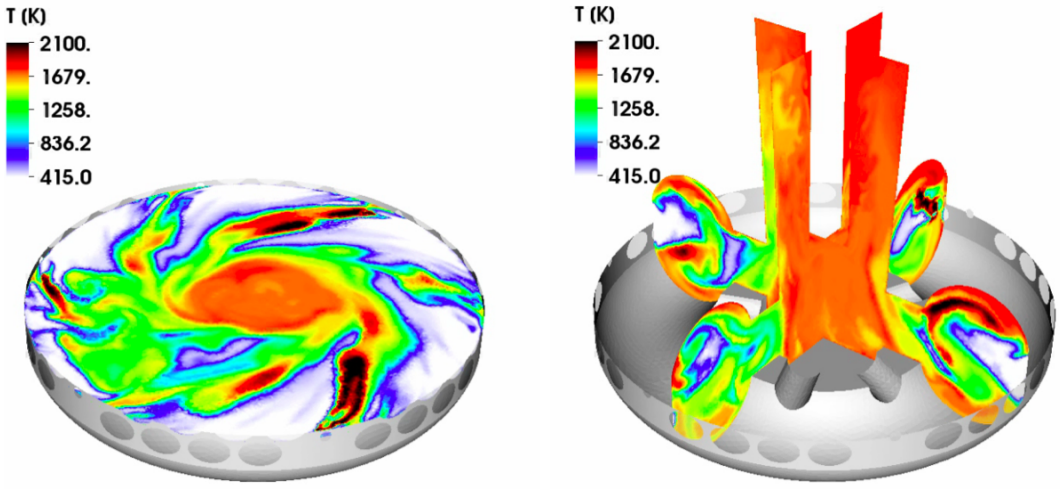

Figure 5.16: Contour of gas phase temperature in axial (left) and radial (right) planes.

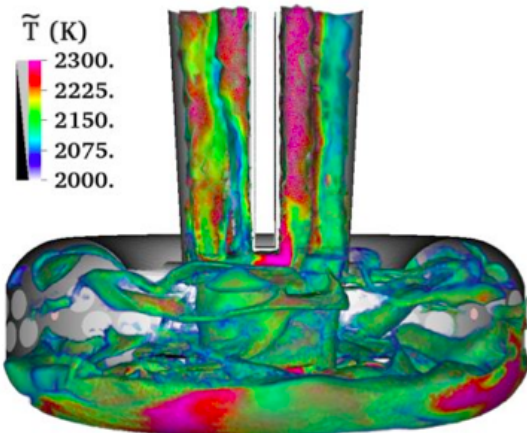

Figure 5.17: Volume rendering of gas phase temperature with half wall cutaway

clear that the flame has spread to the slower regions near the outside wall in between the air inlets and the fuel injectors. As the air flow increases, this region is likely to diminish as mixing between the two streams improves.

In this study, experimental temperature statistics were compared against the LES for purposes of validation. While the qualitative behavior of the axial temperature distribution was closely captured, the radial component showed significant discrepancies particularly toward the outer wall. Additionally, the LES over predicted peak temperatures. While this suggests room for improvement, the general agreement allows the extension of the solver to higher air inflow velocities to gain a qualitative understanding of the effects of higher g-force loadings on the droplets.

5.3.4 On the effects of varying high G loadings

The ultra compact combustor relies on centripetal motion of the droplets and gas phase in order to increase residence time and consequently mixing. Additionally, the previously cited experimental studies suggest that at high g-force loadings, the reaction rates increase. Considering these two factors together, it is expected that for a fixed pressure spray injector, a faster air flow velocity yields correspondingly higher temperatures. The results discussed here, however, tell a more complicated story.

The default air inflow velocity of 6.8 m/s yields peak centripetal acceleration of up to 200 times gravity, depending on the location of the droplets. In order to adequately test their effect, they must be on the order of 2000

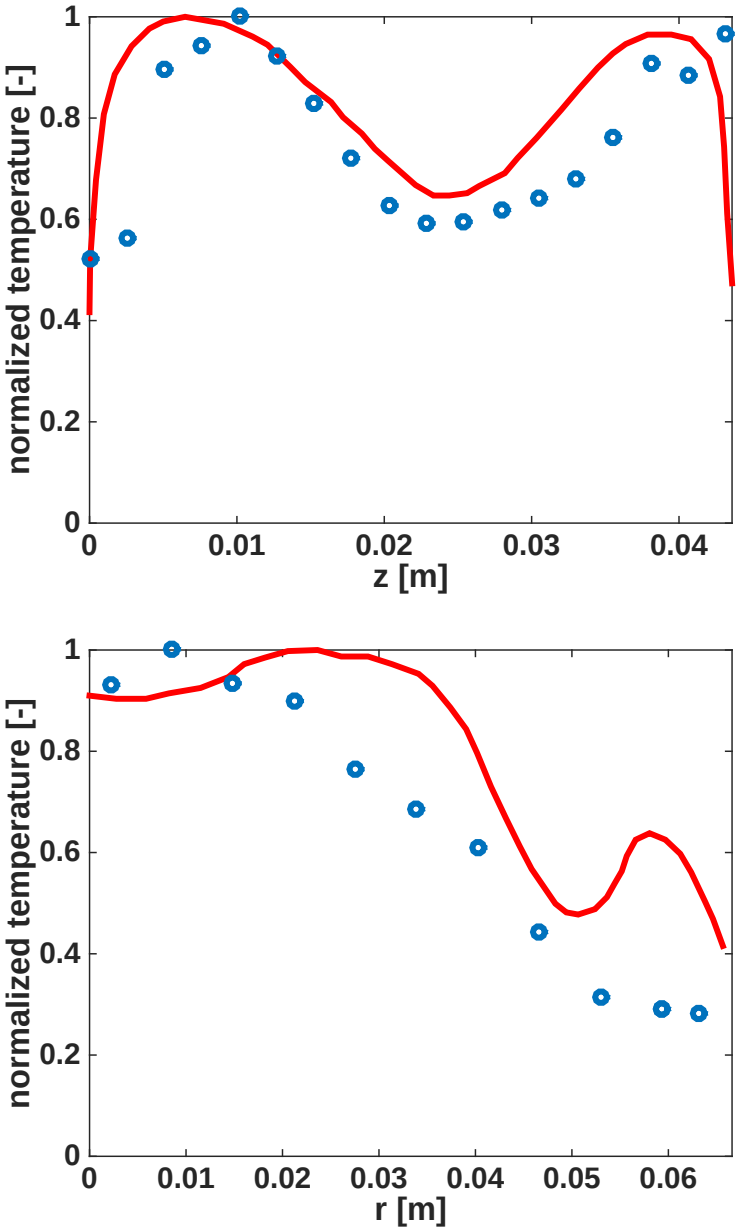

Figure 5.18: Time-averaged temperature profiles from the central axis to the outer wall (top) and from the bottom to top of the toroid at its widest cross-section location (bottom) for experimental results (circles) and LES (solid line).

to 10000 g-forces. Since the force scales with azimuthal velocity squared, the air inflow must only increase modestly. Inflows of 13.6 m/s, 27.2 m/s, and 40.8 m/s, or 2, 4, and 6 times respectively, were chosen, yielding forces of 800, 3200, and 7200 times gravity. For each inflow velocity, the mass flow rate of fuel injected was increased by the same factor, though still entering at the same speed. It should be noted that at the contraction near the exhaust, the flow accelerates significantly, with flow speeds for the fastest case approaching the limit of what could be considered low-Mach. For velocities beyond this, the solver would be inappropriate, with significant acoustic effects ignored.

Figure 5.19 displays the temperature distributions for all four inflow velocities over the same trajectories used above: radially and axially through a point 30° downstream from one of the activated fuel injectors. Considering first the radial distribution, the temperature in the core of the toroid remains relatively unchanged, since equivalence ratio is kept constant and mixing and evaporation have completed by that point. Temperatures near the outer wall vary greatly, however. Dividing the toroid into upper, central, and lower regions, it can be seen that the central region temperature decreases significantly. Since the air flow is directed along this plane, droplets and consequently fuel are convected away rapidly, leading to regions of almost pure air and consequently preventing large reaction zones there. As the air flow increases, that concentration continues to drop.

As the increasing velocity pushes both droplets and gas-phase fuel out of the central plane, it collects in the bottom and top regions of the toroid.

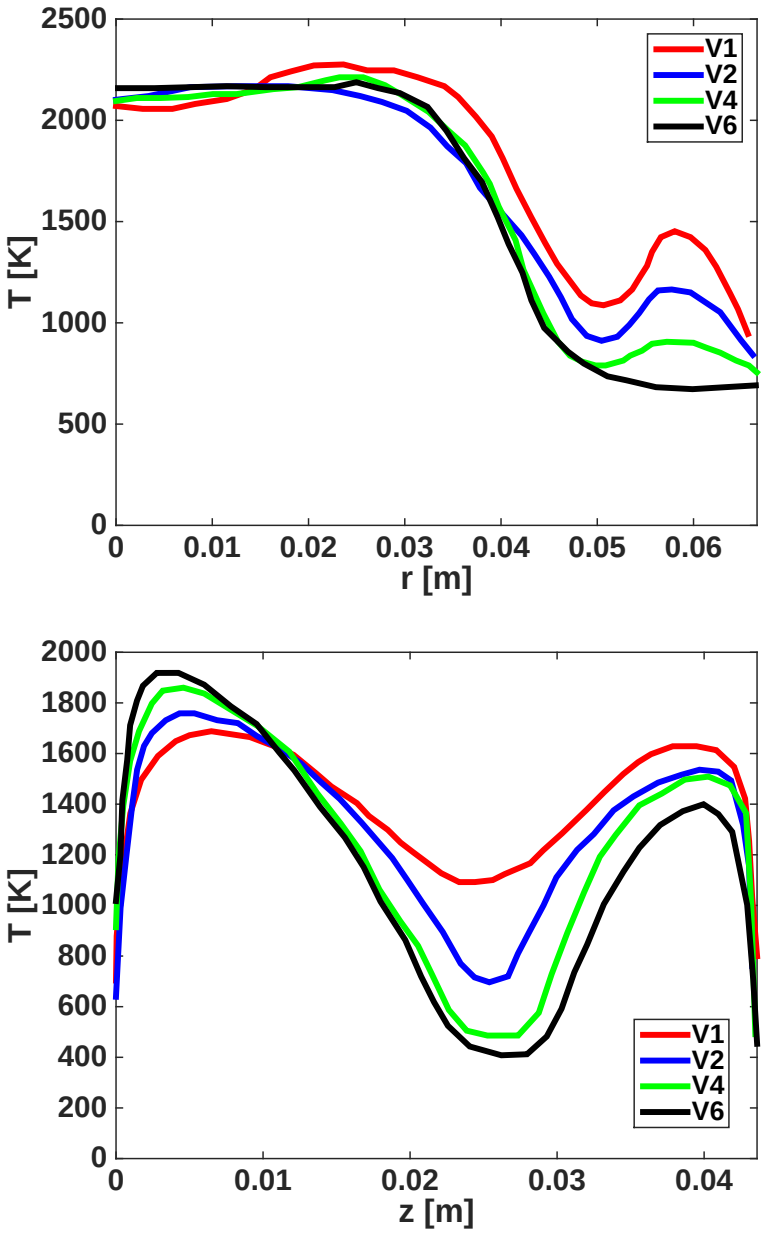

Figure 5.19: Time-averaged temperature profiles from the central axis to the outer wall (top) and from the bottom to top of the toroid at its widest cross-section location (bottom).

However, only the bottom region sees an increase in temperature; the top region actually decreases by several hundred K as the inflow velocity rises. This asymmetry is an extension of the behavior discussed previously. Recall the streamlines in the inert case (Figure 5.9): flow in the top of the toroid cannot move through the central plane to the bottom. Instead, it circulates near the top before being pushed toward the core, entering the contraction, and leaving the domain through the flow straighteners. As the air inflow velocity increases, average flow speeds everywhere increase. Consequently, droplet residence times in the top toroid region decrease. With a reduced fuel concentration, peak temperatures there drop.

5.4 Conclusion

Ultra compact combustors have been shown to provide a promising alternative to conventional configurations by decreasing the required length and weight while maintaining high combustion efficiencies. A model combustor was used to replicate the circumferential mixing utilized in UCC configurations with the goal of studying the effects of centrifugal forces on combustion stability and efficiency. LES results did show promising agreement with experimental observations. Rich droplet-laden mixtures were seen even in the flow straightener, which matched the experimental reports of soot accumulation in the low velocity regions on the upstream end of the straightener. Additionally, experimental results reported the combustor maintaining stable combustion even as liquid fuel flow was significantly reduced. This is direct

evidence that the flame was stabilized in the recirculation zone of the cavity as seen in the LES, where residence times of both droplets and reacting mixtures are greatly extended.

As an evaluation of the capabilities of the solver, this test case was successful. Given the limited studies of LES spray flames in complex geometries, it is particularly useful to evaluate the combustion model. While FPVA is a proven approach [17], commonly applied due to its computational efficiency, some additional complications are necessary to consider with no simple solution available. First is the instability associated with the evaporation source term. While not inherent to a coupled Lagrangian-Eulerian solver, this difficulty is far more likely to happen in an unstructured mesh due to conflicting grid resolution requirements. While both the channel and previous swirler indicated the importance of appropriately resolving the near-wall region, in the ultra compact combustor, these same constraints create several problems. As the size of the cell has no effect on the particles' algebraic models, they may yield extremely high local vaporization rates which typically destabilize a simulation. Second, the higher overall temperature indicates that a better representation of the combustion may be necessary, using more transported scalars.

Chapter 6

Conclusion

LES has emerged as a viable tool for modeling complex turbulent flows. While the current state of the art encompasses various flow solvers and many different turbulence and combustion models, the domain of applicability in the context of instabilities in gas turbine configurations and conditions is ambiguous. In this work, that domain was examined and extended to include several physical phenomena. The first goal toward this step was the creation of an appropriate tool. A solver was developed within the open source code known as OpenFOAM. This solver draws numerous models into a single coherent framework with a broadly applicable interface. While several corollary models were tested, including PDF-based Eulerian and Lagrangian techniques and adaptive chemistry solution, eventually a flamelet-manifold oriented approach was used. Substantial testing and validation was required for diverse conditions.

The first configuration studied was a small channel with a premixed hydrogen flame, with results compared against an accompanying DNS. The computations offered several insights into the behavior of a flame during flashback. The baseline filter width produced a flame front statistically comparable

to those expected. Using quantities such as the depth parameter and the PDF of front fluctuations, LES is accurate in predicting the structure of the turbulent flame front, but not necessarily its characteristic time scales. Regarding small length scales, the LES flame was significantly less wrinkled, with bulges and cusps much shallower than in the corresponding DNS. However, with regards to the whole time domain, this development is reasonably short, after which an accurate estimate of the flame speed is reached. These observations indicate that although the flame is well represented by the flamelet model, some physical behaviors are lost. Furthermore, grid requirements, while not extremely strict, can affect the result and must be taken into consideration when flashback is expected to be relevant in a given problem.

The second configuration was a swirling gas turbine combustor with either a premixed methane or hydrogen-methane flame. Results were compared against experimental data collected at the University of Texas at Austin. Similar to the channel problem, the behavior of interest was the upstream propagation of premixed methane/hydrogen flames through the low speed boundary layer. Regarding the inert field, the simulations proved highly accurate, particularly regarding streaks found within the mixing tube. The simulations also captured much of the flame behavior qualitatively, including the ligament like structures and contraction-like effects due to the flame which caused an acceleration of the unburnt flow as it moved past the front. The result is an accurate prediction of the flashback speed. The LES also exhibited the correct behavior for the transition from a stable flame to flashback, a requisite charac-

teristic of any model used in these types of applications. Additional work will examine the same configuration in the context of more real work conditions, specifically at higher pressures.

The third configuration was a swirling gas turbine combustor with non-premixed JP-8 droplets. Results were compared against experimental data collected at the Air Force Research Laboratory. Unlike the prior problems, this configuration, method of fuel injection, and fuel type are not prone to instabilities resulting from uncontrolled excessive burning; quite the opposite, in fact, as the jet fuel burns with some difficulty and achieving a stable flame took a consistent anchored pilot. Inert velocity statistics generally agreed with experiments, indicating a sufficiently resolved grid in consideration of the turbulence model. Rich droplet-laden mixtures were seen even in the flow straightener, which matched the experimental reports of soot accumulation in the low velocity regions on the upstream end of the straightener. The LES indicated an interesting phenomena, with regards to the flame stabilization and location: residence times for both droplets and flow increase substantially near the bottom cavity of the toroid creating a stable burning zone. Looking at the temperature profiles, the LES did have some issues correctly predicting the magnitudes, though their shape is captured. This discrepancy is likely an artifact of a previously documented flaw in the application of Lagrangian particle tracking in unstructured meshes and typically results in large instabilities. While some measures were taken to rectify it in this problem, more work is required to fix the core issue. Nevertheless, despite over predicting peak tem-

peratures, the solver is still useful in examining the trends and relative effects of extended applications. As g-force loadings increase, for instance, temperatures near the central injection plane decrease while those in the lower toroid increase, indicating a greater fuel concentration and diminished extinction.

In this work, the use of LES in gas turbine combustor has been studied comprehensively. Simulation of several critical behaviors within the combustion chamber indicate that not only are these computationally tractable, but also highly useful in understanding the fundamental flow and reaction physics. The use of this tool could effectively aid the development of new novel configurations and reduce the expense related to experimental testing. Furthermore, the versatility available through OpenFOAM allows a continual evolution of the solver as more applications are considered.

Bibliography

[1] General electric website.

[2] Openfoam documentation.

[3] *Airplane Flying Handbook*. U.S. Department of Transportation, Federal Aviation Administration, faa-h-8083-3a edition, 2004.

[4] K. Akselvoll and P. Moin. Large eddy simulation of turbulent confined coannular jets. *Journal of Fluid Mechanics*, 315:387–411, 1996.

[5] W. Anderson, M. Polanka, J. Zelina, D. Evans, S. Stouffer, and G. Justinger. Effects of a reacting cross-stream of turbine film cooling. *Journal of Engineering for Gas Turbines and Power-Transactions of the ASME*, 132, 2010.

[6] W. Anderson, J. Radtke, P. King, H. Thornburg, J. Zelina, and B. Sekar. Effects of main swirl direction on high-g combustors. In *44th AIAA Joint Propulsion Conference*, 2008.

[7] P Auzillon, R Vicquelin, O Gicquel, N Darabiha, D Veynante, and B. Fiorina. A filtered tabulated chemistry model of les of reactive flows. In *48th AIAA Aerospace Sciences Meeting*, 2010.

[8] J. Bardina, J. H. Ferziger, and W. C. Reynolds. Improved subgrid models for large eddy simulation. AIAA paper, 1980. 80-1357.

[9] G. Blanquart, P. Pepiot-Desjardins, and H. Pitsch. Chemical mechanism for high temperature combustion of engine relevant fuels with emphasis on soot precursors. *Combustion and Flame*, 156(3):588–607, 2009.

[10] M Boger, D Veynante, H Boughanem, and A Trouve. Direct numerical simulation analysis of flame surface density concept for large eddy simulation of turbulent premixed combustion. *Twenty-Seventh Symposium (International) on Combustion*, 27:917–925, 1998.

[11] B.T. Bohan. *Analysis of flow migration in an ultra-compact combustor*. PhD thesis, Airforce Institute of Technology, 2011.

[12] R. Borghi and M. Destriau. *Combustion and Flames*. Editions Technip, 1998.

[13] K. N. C. Bray and N. Peters. Laminar flamelets in turbulent flames. In P. A. Libby and F. A. Williams, editors, *Turbulent Reacting Flows*, pages 63–113. Academic Press, New York, 1994.

[14] A.M. Briones, B. Sekar, H. Thornburn, and J Zelina. Effect of vane notch and ramp design on the performace of a rectangular inter-turbine burner. In *48th ASM Aerospace Sciences Meeting*, 2010.

[15] A.M. Briones, J Zelina, and V.R. Katta. Flame stabilization in small cavities. *AIAA Journal*, pages 224–235, 2010.

[16] A. J. Chorin. Numerical solution of the navier-stokes equations. *Mathematics of Computation*, 22(104):745–762, 1968.

[17] M. Chrigui, A. Masri, A. Sadiki, and J. Janicka. Large eddy simulation of a polydispersed ethanol spray flame. *Flow, Turbulence and Combustion*, 90(4):813–832, June 2013.

[18] F. Colin, F Ducros, D. Veynante, and T. Poinsot. A thickened flame model for large-eddy simulation of premixed turbulent combustion. *Physics of Fluids*, 12(7):1843–1863, 2000.

[19] F Dabireau, B Cuenot, O Vermorel, and T Poinsot. Interaction of flames of h2 and o2 with inert walls. *Combustion and Flame*, 135:123–133, 2003.

[20] P. E. Desjardin and S. H. Frankel. Assessment of turbulent combustion submodels using the linear eddy model. *Combustion and Flame*, 104:343–357, 1996.

[21] J. K. Dukowicz. A particle-fluid numerical model for liquid sprays. *Journal of Computational Physics*, 35:229–253, 1980.

[22] D. Ebi and N. T. Clemens. Experimental investigation of flashback in premixed ch4/h2-air swirl flames. *AIAA Journal*, 2013.

[23] D. Ebi and N. T. Clemens. Time-resolved piv and flame front imaging of boundary layer flashback in a swirl combustor. *Symposium (International) on Combustion*, July 2014.

[24] C Eichler. *Flame flashback in wall boundary layers of premixed combustion systems*. PhD thesis, Technische Universitat Munchen, 2011.

[25] C Eichler, G. Baumgartner, and T Sattelmayer. Experimental investigation of turbulent boundary layer flashback limits for premixed hydrogen-air flames confined in ducts. *Journal of Engineering for Gas Turbines and Power*, 134(011502), 2012.

[26] C Eichler and T Sattelmayer. Experiments on flame flashback in a quasi-2d turbulent wall boundary layer for premixed methane-hydrogen-air mixtures. *Journal of Engineering for Gas Turbines and Power*, 133, 2011.

[27] J. H. Ferziger and M. Peric. *Computational Methods for Fluid Dynamics*. Springer, 3rd edition, 2002.

[28] B. Fiorina, O. Gicquel, L. Vervisch, S. Carpentier, and N. Darabiha. Approximating the chemical structure of partically premixed and diffusion counterflow flames using FPI flamelet tabulation. *Combustion and Flame*, 140:147–160, 2005.

[29] R. O. Fox. *Computational Models for Turbulent Reacting Flows*. Cambridge University Press, 2003.

[30] J Fritz, M Kroner, and T Sattelmayer. Flashback in a swirl burner with cylindrical premixing zone. *Journal of Engineering for Gas Turbines and Power-Transactions of the ASME*, 126(2):276–283, 2004.

[31] M. Germano, U. Piomelli, P. Moin, and W. H. Cabot. A dynamic subgrid-scale eddy viscosity model. *Physics of Fluids*, 7:1760–1765, 1991.

[32] A Gruber, J. H. Chen, D. Valiev, and C. K. Law. Direct numerical simulation of premixed flame boundary layer flashback in turbulent channel flow. *Journal of Fluid Mechanics*, 709:516–542, 2012.

[33] A Gruber, R Sankaran, E Hawkes, and J. H. Chen. Turbulent flame-wall interaction: a direct numerical simulation study. *Journal of Fluid Mechanics*, 658:5–32, SEP 2010.

[34] M. Ihme, L. Shunn, and J. Zhang. Regularization of reaction progress variable for application to flamelet-based combustion models. *Journal of Computational Physics*, 231:7715–7721, 2012.

[35] R. I. Issa, A. D. Gosman, and A. P. Watkins. The computation of compressible and incompressible recirculating flows by a non-iterative implicit scheme. *Journal of Computational Physics*, 62:66–82, 1986.

[36] J. Janicka, W. Kolbe, and W. Kollmann. Closure of the transport equation for the PDF of turbulent scalar fields. *Journal of Non-Equilibrium Thermodynamics*, 4:47–66, 1970.

[37] H Jasak. *Error analysis and estimation for the finite volume method with applications to fluid flows*. PhD thesis, Imperial college of London, 1996.

[38] D. Kirk, G. Guenette, S. Lukachko, and I. Waitz. Gas turbine engine durability impacts of high fuel-air ratio combustors-part ii: Near-wall

reaction effects on film-cooled heat transfer. *Journal of Engineering for Gas Turbines and Power-Transactions of the ASME*, 125:751–759, 2003.

[39] Bernard Koff. Gas turbine technology evolution. *AIAA Journal*, 2003.

[40] V Kurdyumov, E Fernandez-Tarrazo, and A Linan. Flame flashback and propagation of premixed flames near a wall. In *Proceedings of the Combustion Institute*, volume 28, pages 1883–1889, 2000.

[41] V Kurdyumov, E Fernandez-Tarrazo, JM Truffaut, J Quinard, A Wangher, and G Searby. Experimental and numerical study of premixed flame flashback. In *Proceedings of the Combustion Institute*, volume 31, pages 1275–1282, 2007.

[42] C. K. Law and C. Sung. Structure, aerodynamics, and geometry of premixed flamelets. *Progress In Energy and Combustion Science*, 26:459–505, 2000.

[43] A. Lefebvre and D. Ballal. Combustion in a centrifugal-force field. *Proceedings of the Combustion Institute*, 13:625–629, 1971.

[44] BP LEONARD. Stable and Accurate Convective Modeling Procedure Based on Quadratic Upstream Interpolation. *Computer Methods in Applied Mechanics and Engineering*, 19(1):59–98, 1979.

[45] G. Lewis. Combustion in a centrifugal-force field. *Proceedings of the Combustion Institute*, 13, 1971.

[46] G. Lewis. Centrifugal-force effects on combustion. *Proceedings of the Combustion Institute*, 14, 1973.

[47] Juan Li, Zhenwei Zhao, Andrei Kazakov, and Frederick Dryer. An updated comprehensive kinetic model of hydrogen combustion. *International Journal of Chemical Kinetics*, 36:566–575, 2004.

[48] Timothy Lieuwen and Vigor Yang. *Combustion Instabilities in Gas Turbine Engines: Operational Experience, Fundamental Mechanisms, and Modeling*. AIAA, 6.

[49] D. K. Lilly. A proposed modification of the Germano subgrid-scale closure method. *Physics of Fluids A*, 4:633–635, 1992.

[50] C.-X Lin, R. Holder, H. Thornburg, B. Sekar, J. Zelina, W. Anderson, M. Polanka, S. Stouffer, and A. Briones. Numerical simulation of film cooling in reactive flow over a surface with shaped coolant hole. In *47th AIAA Aerospace Sciences Meeting*, 2009.

[51] A. N. Lipatnikov and J. Chomiak. Effects of premixed flames on turbulence and turbulent scalar transport. *Progress in Energy and Combustion Science*, 36(1):1–102, 2010.

[52] S. Lukachko, D. Kirk, and I. Waitz. Gas turbine engine durability impacts of high fuel-air ratio combustors-part i: potential for secondary combustion of partially reacted fuel. *Journal of Engineering for Gas Turbines and Power-Transactions of the ASME*, 125:742–750, 2003.

[53] A Majda and K Lamb. Simplified equations for low mach number combustion with strong heat release. *Dynamical issues in combustion theory*, IMA(664), 1990.

[54] A Majda and J Sethian. Derivation and numerical solution of the equations of low mach number combustion. *Combustion Science and Technology*, 42:185–205, 1984.

[55] A. R. Masri and S. B. Pope. PDF calculations of piloted turbulent nonpremixed flames of methane. *Combustion and Flame*, 81:13–29, 1990.

[56] C Meneveau and J. Katz. Scale-invariance and turbulence models for large-eddy simulation. *Annual Review of Fluid Mechanics*, 32:1–32, 2000.

[57] P Michalke and T Schmuck. Powerful products for the enhanced flexibility of gas turbines. In *POWER-GEN Europe*, 2012.

[58] R. Miller and J. Bellan. Direct numerical simulation of a confied three-dimensional gas mixing layer with one evaporating hydrocarbon-droplet-laden stream. *Journal of Fluid Mechanics*, 384:293–338, 1999.

[59] R. Miller and J. Bellan. Direct numerical simulation and subgrid analysis of a transitional droplet laden mixing layer. *Physics of Fluids*, 12:650–671, 2000.

[60] P. Moin. Advances in large eddy simulation methodology for complex flows. *International Journal of Heat and Mass Transfer*, 23:710–720, 2002.

[61] P. Moin, K. Squires, W. Cabot, and S. Lee. A dynamic subgrid-scale model for compressible turbulence and scalar transport. *Physics of Fluids A*, 3:2746–2757, 1991.

[62] S. Muppidi and K. Mahesh. Direct numerical simulation of round turbulent jets in crossflow. *Journal of Fluid Mechanics*, 574:59–84, 2007.

[63] K. Narayanaswamy, G. Blanquart, and H. Pitsch. A consistent chemical mechanism for oxidation of substituted aromatic species. Submitted to Combustion and Flame, 2009.

[64] N. Okongo and J. Bellan. Consistent large-eddy simulation of a temporal mixing layer laden with evaporating drops. part1. direct numerical simulation, formulation and a priori analysis. *Journal of Fluid Mechanics*, 499:1–47, 2004.

[65] S. V. Patankar. A calculation procedure for two dimensional elliptic situations. *Numerical Heat Transfer*, 14:409–425, 1984.

[66] S. V. Patankar and D. B. Spalding. A calculation for heat, mass, and momentum transfer in three-dimensional parabolic flows. *International Journal of Heat and Mass Transfer*, 15(10):1787–1806, OCT 1972.

[67] Norbert Peters. *Turbulent Combustion.* Cambridge University Press, 2000.

[68] C. D. Pierce and P. Moin. A dynamic model for subgrid-scale variance and dissipation rate of a conserved scalar. *Physics of Fluids*, 10:3041–3044, 1998.

[69] Charles D. Pierce. *Progress-variable approach for large-eddy simulation of turbulent combustion*. PhD thesis, Stanford University, 2001.

[70] H. Pitsch. A C++ computer program for 0-d and 1-d laminar flame calculations. RWTH Aachen, 1998.

[71] H Pitsch. A consistent level set formulation for large-eddy simulation of premixed turbulent combustion. *Combustion and Flame*, 143(4):587–598, December 2005.

[72] H. Pitsch. Large-eddy simulation of turbulent combustion. *Annual Review of Fluid Mechanics*, 38:453–482, 2006.

[73] S. B. Pope. A Monte Carlo method for the PDF equations of turbulent reactive flow. *Combustion Science and Technology*, 25:159–174, 1981.

[74] S. B. Pope. *Turbulent Flows*. Cambridge University Press, 2000.

[75] S. B. Pope. Ten questions concerning the large-eddy simulation of turbulent flows. *New Journal of Physics*, 6(35), 2004.

[76] S. Puranam, J. Arici, N. Sarzi-Amade, D. Dunn-Rankin, and W. Sirignano. Turbulent combustion in a curving, contracting channel with a

cavity stabilized flame. *Proceedings of the Combustion Institute*, 32:2973–2981, 2009.

[77] V. Raman, H. Pitsch, and R. O. Fox. Hybrid LES-PDF methods for the simulation of turbulent reactive flows. In *Topical conference at the AIChE annual meeting, San Francisco, CA*, 2003.

[78] J. Reveillon and L. Vervisch. Analysis of weakly turbulent dilute-spray flames and spray combustion regimes. *Journal of Fluid Mechanics*, 537:317–347, 2005.

[79] J. Smagorinsky. General circulation experiments with the primitive equations: I. the basic equations. *Monthly Weather Review*, 91:99–164, 1963.

[80] Y Sommerer, D Galley, T Poinsot, S Ducruix, F Lacas, and D Veynante. Large eddy simulation and experimental study of flashback and blow-off in a lean partially premixed swirled burner. *Journal of Turbulence*, 5(37), 2004.

[81] Richard Sonntag and Claus Borgnakke. *Introduction to Engineering Thermodynamics*. Wiley, 2000.

[82] G. Sturgess, J. Zelina, D. Shouse, and W. Roquemore. Emissions reduction technology for military gas turbine engines. *Journal of Propulsion and Power*, 21(2):193–217, 2005.

[83] C. J. Sung, C. K. Law, and J. Y. Chen. An augmented reduced mechanism for methane oxidation with comprehensive global parametric val-

idation. *Twenty-Seventh Symposium (International) on Combustion*, 27:295–304, 1998.

[84] P.K. Sweby. High resolution schemes using flux limiters for hyperbolic conservation laws. *SIAM J. Numer. Anal.*, 21(5):995–1011, OCT 1984.

[85] E Tangermann and M. Pfitzner. Evaluation of combustion models for combustion-induced vortex breakdown. *Journal of Turbulence*, 10(7):1–21, 2009.

[86] D Thibaut and S Candel. Numerical study of unsteady turbulent premixed combustion: application to flashback simulation. *Combustion and Flame*, 113:53–65, 1998.

[87] H. Thornburg, B. Sekar, J. Zelina, W. Anderson, M. Polanka, C. Lin, R. Holder, A. Briones, and S. Stouffer. Design studies of turbine blade film cooling with unburned fuel in cross stream flow. In *47th AIAA Aerospace Sciences Meeting*, 2009.

[88] J. P. Van Doormall and G. D. Raithby. Enhancements of the simple method for predicting incompressible fluid flows. *Numerical Heat Transfer*, 7:147–163, 1984.

[89] J. A. Van Oijen and L. P. H de Goey. Modeling of premixed laminar flames using flamelet-generated manifolds. *Combustion Science and Technology*, 161(1):113–137, 2000.

[90] J. Zelina, D. Shouse, and C. Neuroth. High-pressure test of a high-g, ultra-compact combustor. In *41st AIAA Joint Propulsion Conference*, 2005.

[91] J. Zelina, D. Shouse, J. Stutrud, G. Sturgess, and W. Roquemore. Exploration of compact combustors for reheat cycle aero engine applications. *Proceedings of the ASME Turbo Expo*, 2006.

[92] J. Zelina, G. Sturgess, and D. Shouse. Aiaa joint propulsion conference. In *The behavior of an ultra-compact combustor (UCC) based on centrifugally-enhanced turbulent burning rates*, 2004.